Remagnetization during Rotation: The Variscan Orocline(s?) in Iberia

Master thesis by: D.R.H. Brouwer, Utrecht University

Supervised by:
Mark Dekkers, Utrecht University
Daniel Pastor Galán, Utrecht University

Final Version

Abstract

The Variscan orogeny in Iberia consists of at least one orocline in a c-shape but recent work suggests that a second orocline is formed simultaneously, creating an s-shape. In order to investigate the geometry and kinematics of the southern orocline we perform a paleomagnetic study on remagnetized Cambrian limestones located in the middle of the s-shape with the Cantabrian Orocline in the north and the Central Iberian Orocline to the south.
The paleomagnetic study shows 65 degree spreading with east and southeast magnetic directions. The rocks show magnetic isotropy and fold tests are negative. Thermomagnetic analysis shows pyrrhotite as main carrier with inclusions of magnetite, which is more closely investigated by using hysteresis loops, IRM acquisition, and subsequent unmixing in three end-members.
The total interpretation is a 65 degree counterclockwise rotation with rapid local remagnetizations during the Later Carboniferous to Early Permian. This interpretation does only fit with the Cantabrian Orocline in the north, which disproves simultaneous formation of both oroclines. The Central Iberian Orocline, if present, must be formed before the initiation of the Cantabrian Orocline.

Table of Contents

1. Introduction

The textbook geometry of mountain belts in map view is a (near) straight orogen which does not deform over time. However, this is not the standard case as orogen curvatures are common around the Earth. Three kinematic classifications can be distinguished if an orogen shows curvature (Weil & Sussman 2004; Weil et al. 2013): a primary arc (which has initial curvature and no rotation after formation), a progressive arc (a belt which acquires rotation during primary formation), and an orocline (an initially straight orogen which is rotated around a vertical axis during secondary deformation). One of the key ways of proving secondary oroclinal bending is using paleomagnetism which records the vertical axis rotation of the orogen (Schwarz & Van der Voo 1983; Weil et al. 2000; Pastor-Galán et al. 2012; Weil et al. 2013). This needs to be combined with strain and kinematic analyses measurements using rotated structural trends that were initially straight (Weil & Sussman 2004; Pastor-Galán et al. 2011).

The theory on the formation of an orocline as described above is generally accepted by the literature. However, unravelling the mechanisms of orocline formation is a complex issue which is not understood sufficiently. To try and unravel the mechanisms of orocline formation, the Variscan orocline(s) of Iberia are used as study case.

The Cantabrian Orocline, also known as the Ibero-Amorican arc in the literature (eg. Aerden 2004), is located in northern and western Iberia and is one of the best studied oroclines in the world (Gutiérrez-Alonso et al. 2012; Weil et al. 2013). Carey (1955) was the first to name this vertical rotations oroclines and already had an eye for Iberia and matching rotated structures across Iberia and Western Europe. The Cantabrian orocline is part of the Variscan belts that have been produced over major parts of Europe (Martínez Catalán et al. 2007; Martínez Catalán et al. 2009; Weil et al. 2013). The Variscan orogeny in Iberia is formed by the closure of the Rheic Ocean; positioned in between Iberia, Avalonia and Gondwana; and the amalgamation of Pangea in between 420 and 310 Ma (eg. Matte 2001; Winchester et al. 2002; Martínez Catalán et al. 2009; Weil et al. 2013 and others). The Variscan structures in Iberia are described in three stages of deformation (Diez-Balda et al. 1995; Weil et al. 2000), in which phase three is responsible for the oroclinal bending (Weil et al. 2000; Pastor-Galán et al. 2011; Gutiérrez-Alonso et al. 2012). All the deformation events will be discussed extensively in the geological setting.

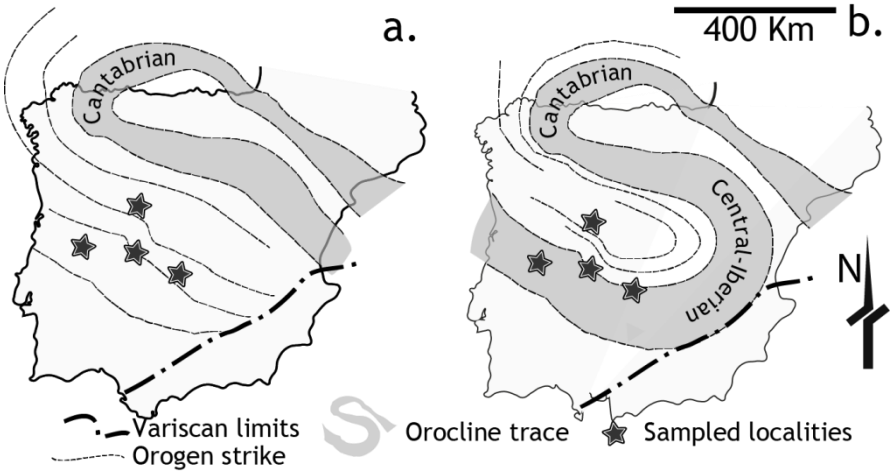

Figure 1: Two contrasting hypotheses on orocline formation in Iberia. Figure a shows the single orocline theory, b shows the extra Central Iberian Orocline as depicted by Shaw et al., 2012. The darker traces elements show the outlines of the oroclines, while the stars represent the localities that have been sampled.

One orocline can already be observed in the major maps of the Iberian Peninsula as a curved set of lithologies in a c-shape, also highlighted in figure 1a. This oroclinal bending, which is a complete 180 degree curvature of the orogen around a pivot point, is dated Moscovian to Asselian and is supported by paleomagnetic (Van der Voo et al. 1997; Weil et al. 2010; Yonkee & Weil 2010; Pastor-Galán et al. 2012), magmatic (Gutiérrez-Alonso et al. 2011a, 2011b), and structural data (Aerden 2004; Pastor-Galán et al. 2011).

There is however a second hypothesis which contradicts the one explained above. As shown in figure 1b, a second orocline with a hinge in the east of Iberia is posed as hypothesis next to the earlier mentioned single orocline, creating an s-shape over Iberia. It is named Central Iberian Orocline (CIO) and is based on porphyroblast orientations (Aerden 2004), aeromagnetic analysis (Aerden 2004; Martínez Catalán 2011), and paleocurrent directions (Shaw et al. 2012). This Central Iberian Orocline, if it exists, is assumed to be formed in the same timeframe as the Cantabrian Orocline and is also part of the Variscan structures in Iberia (Aerden 2004; Martínez Catalán 2011; Shaw et al. 2012). Formation of this orocline can be linked to late strike-slip tectonics along a broad, dextral, and intracontinental zone (Martínez Catalán 2011). The southern orocline in scenario is hard to see in map view as the affected rocks are almost completely covered by younger sediments.

These two hypotheses vary distinctively and imply major changes in formation and deformation of the Iberian Orocline(s). This could drastically change the general consensus on the amalgamation of Pangea and role that the Iberian Peninsula plays in it. Therefore it is well worth the effort to sample, measure, and process this data and try to validate one of these hypotheses. The main dissimilarity between the two hypotheses can be found in the Central Iberian Zone, which is located in west and central Iberia (see figure 2 for details).

This main goal of this master thesis is to constrain the geometry and kinematics of the Central-Iberian bend(s) via a complete paleomagnetic and rock magnetic analysis. In order to successfully manage this goal, a combined study of paleomagnetism and rock magnetism is performed on remagnetized Cambrian limestones which are positioned the center of the putative s-shape, as can be observed in figure 1. The two studies will be treated separately throughout the results and interpretation. These Cambrian limestones have never been used before in the orocline studies and therefore add new information to the data pool. The localities of the sampling campaign are shown in figure 1 in combination with the earlier mentioned orocline hypotheses.

2. Geological setting

2.1 Deformation overview of Iberia from latest Phanerozoic to Permian

The history of the Iberian Peninsula from the Phanerozoic to the Permian (the core interest) is complex with several major tectonic events. The first major deformation event relevant for this study is the Cadomian orogeny which is a 650 to 500 Ma Gondwana-located orogeny (Diez-Balda et al. 1995; Linnemann et al. 2008). This is followed by a northward extension in the Cambrian/Ordovician related to the opening of the Rheic Ocean. In this extensional phase, Iberia is located on the southern margin as can be seen in paleomagnetic data (Cocks & Torsvik 2002; Weil et al. 2013 and references therein) and related magmatism (Gutiérrez-alonso & Fernández-suárez 2004; Montero et al. 2007; Gutiérrez-Alonso, Fernández-Suárez, et al. 2011). The uppermost Ordovician marks the start of a second rifting phase which separates Amorica and Iberia via the Paleotethys ocean (Stampfli & Borel 2002; Torsvik et al. 2012). This is followed by the closing of the Rheic Ocean, which causes the Variscan Orogeny (Matte 2001; Díez Fernández et al. 2012), explained in detail in section 2.2.

2.2 Formation and deformation of the Variscan in Iberia

The Variscan orogeny in Iberia starts with the compression due to the movement of Laurentia towards Gondwana and Iberia dated Silurian to Early Devonian (Martínez Catalán et al. 2007). During the late Devonian, dated around 359 Ma, the supposed basins in between Gondwana and Iberia closed (Dallmeyer et al. 1997; Martínez Catalán et al. 2007). A Carboniferous syn-orogenic pulse of magmatism is emplaced in the hinterland of the CIZ at 350-340 Ma (Carbonell et al. 2004; Gutiérrez-Alonso et al. 2011b) .

The structural history of the Variscan can be classified in three different deformation phases (Diez-Balda et al. 1995; Weil et al. 2000). All of them are found in figure 2 (modified from Martinez-Catalan et al., 2012), in which the observed D1 folding is denoted with purple and D2/D3 folding in blue colors throughout Iberia. The sampled sites are denoted with stars.

D1 is a spatially different set of deformations with recumbent folds on the east and north side and upright folds in the south (Diez-Balda et al. 1995 and references therein). The Tamames Syncline, important in this research as a sampling location, is part of this D1 phase, but strikes northwest – southeast (Diez-Balda et al. 1995 and references therein).

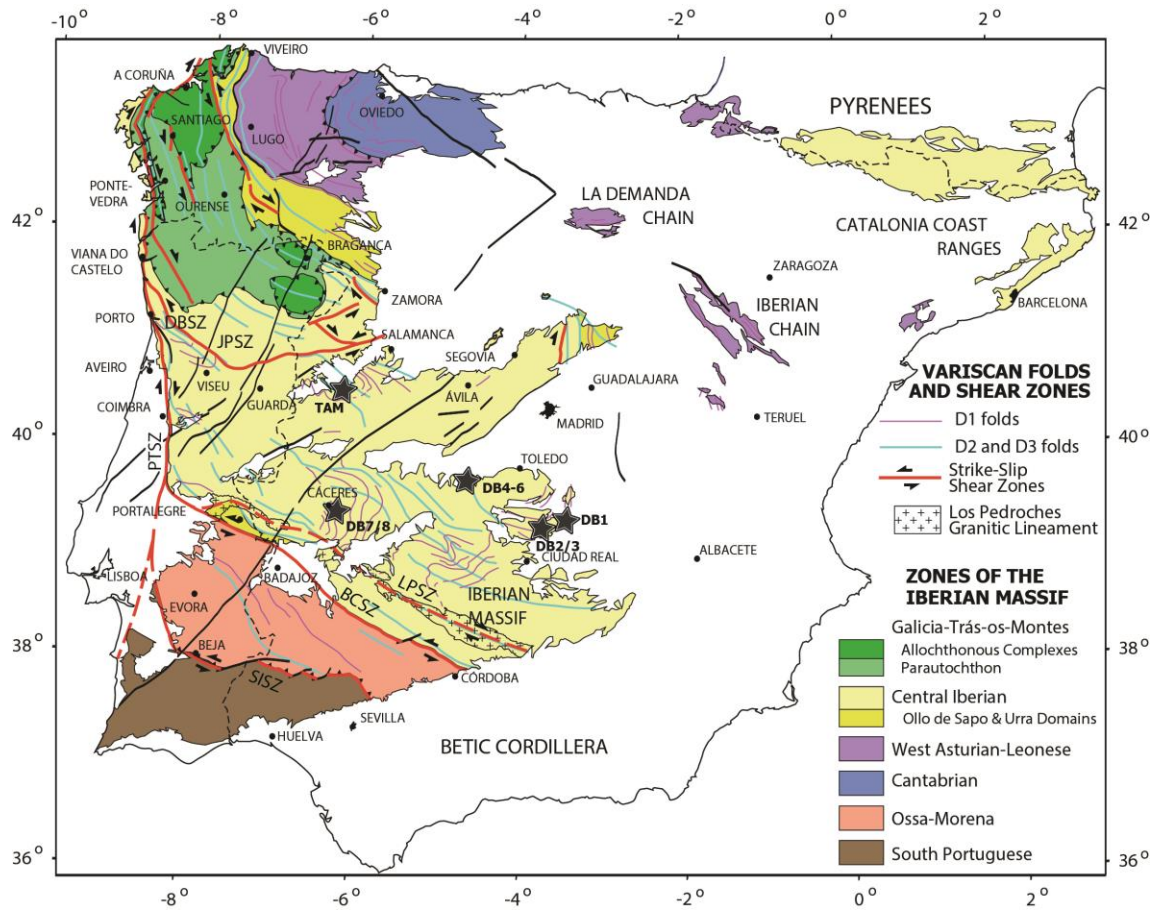

Figure 2: Map showing all Variscan-deformed rocks that have not been covered with sediments. The axial traces of D1 and D2/D3 are highlighted as well as the major shear zones. BCSZ Badajoz-Cordoba shear zone; DBSZ Douro-Beira shear zone; JPSZ Juzbado Penalva shear zone; LPSZ Los Pedroches shear zone; PTSZ Porto-Tomar shear zone; SISZ Southern Iberian shear zone. Modified from Martínez-Catalán (2012)

D2 is a refold of D1 and has an S2 foliation which overprints the S1 and the pre-Variscan granitoids. Variscan Granites which were emplaced in D1 were heterogeneously deformed by D2 (Diez-Balda et al. 1995). This deformation phase can be linked to extensional tectonics as the thickened crust in the orogen shows syn-collisional gravitational collapse as seen by the normal faulting (Diez-Balda et al. 1995; Martínez Catalán et al. 2009). D2 is accompanied by syn-kinematic granitoids, which occur in regional metamorphic domes. The age of the syn-kinematic granites has been constrained at 325-318 Ma in the CIZ (Dias et al. 1998; Gutiérrez-Alonso, et al. 2011b). At the western part of Asturo-Leonese Zone (ALZ), see figure 2, granites of a similar age (325-315Ma) have been observed by Fernández Suarez et al. (2000); Dias et al. (1998) and others. Gutiérrez-Alonso et al. (2011b) suggests that these granites can be combined to one event with the 325-318 Ma ones.

The third phase is an open, subvertical folding of large wavelength (up to 12 km) and small amplitude (Diez-Balda et al. 1995; Aerden 2004) striking roughly 100-120 in the Central Iberian Zone (Diez-Balda et al. 1995; Aerden 2004; Díez Fernández et al. 2013 and others). This is the major oroclinal phase which is mentioned in the introduction. The orientation of D3 folds changes towards the north to a north – south oriented strike (Dallmeyer et al. 1997; Díez Fernández et al. 2011). Accompanied by D3 is the last Variscan post-orogenic pulse, found in both the internal and external part of the orocline, peaking around 310-295 Ma (Dias et al. 1998; Fernández Suarez et al. 2000; Gutiérrez-Alonso et al. 2011b and references therein). These show a deep lithosphere signature and are therefore interpreted to be part of a thick skinned orogenic event. After this oroclinal phase of deformation, Iberia has seen no internal rotations (Weil et al. 2010).

Paleomagnetic data points are mainly found in the northern and northwestern part of Iberia. Van der Voo et al. 1997 was first to distinguish two remagnetizations in the Cantabrian Orocline: one synfolding during Westphalian to Stephanian and one post-folding. This is further constrained and accepted by data from various literature sources which all add paleomagnetic data positioned in the Cantabrian Orocline (Weil et al. 2000; Weil et al. 2001; Weil & Sussman 2004; Weil 2006; Gutiérrez-Alonso et al. 2012; Weil et al. 2013). Weil et al. 2010 combined all the available paleomagnetic data to a stable pole for Iberia of 203.3/43.9 with an error of 5.4 at 290 Ma.

Pastor-Galán et al. (2011) show active rotation of the Variscan during the Stephanian by dating erosional surfaces in sediments and linking these to different joint sets. The rotation has ended in the Permian, as the joint sets are showing consistently the same direction over the bended area (Pastor-Galán et al. 2011). Kollmeier et al. (2000) also showed a rotation of the Cantabrian Orocline using calcite twinning to obtain the $\sigma 1$ by subsequently unbending the secondary deformation. This shows a north-south compressional regime, which fits with the oroclinal bending interpretation (Kollmeier et al. 2000).

The formation of the Cantabrian Orocline has been interpreted as a thick-skinned orogenic event with widespread mantle replacement (Gutiérrez-Alonso et al. 2012). The composition and position of the granitoids show a deeper origins of mantle material as the intrusions (Gutiérrez-Alonso, Fernández-Suárez, et al. 2011). Younger intrusions are positioned more in the core of the Cantabrian Orocline, while older are located more on the outside (Gutiérrez-Alonso, Fernández-Suárez, et al. 2011). Both observations are interpreted as a complete crust and lithosphere and even delamination of the lithosphere (Fernández Suarez et al. 2000; Gutiérez-Alonso et al. 2011a).

Inclusions in porphyroblast show a curved geometry which can be linked to the Cantabrian Orocline, as well as a second rotation around a different axis in the Central Iberian Zone, which can be linked to a Central Iberian Orocline (Aerden 2004). The relative timings that have been found in the minerals (FS1 to FS4) have been coupled to four deformation phases of which the youngest is determined to continue to at least after 310 Ma (Aerden 2004). Shaw et al. (2012) has used

paleocurrent directions in Ordovician quartzite's (which are discussed below) which show a consistent pattern to the west to northwest when the bending is removed. The data is collected over large parts of Iberia and assumes that this has to happen simultaneously with the formation of the Cantabrian Orocline. This implies the simultaneous formation of the second orocline. Paleomagnetic data from the Almadén area in Southern Spain shows NRM pointing to southeast and east (Perroud et al. 1991; Parés & Van der Voo 1992). This data is did not lead to an interpretation at that time, but could be of influence when looking at the Central Iberian Orocline.

The formation of the Central Iberian Orocline is mechanically explained by Martínez Catalán (2011) which assumes dextral strike slip shear zones hundreds of kilometers long. Evidence for this is to be found in the similarities in rock successions in the Central Iberian Zone and the Central Amorican Zone located in northwestern France (Martínez Catalán 2011 and references theirin). The main shear zones can be caused by a weakening in the crust which can be caused by a suture, continental rift of a Paleotethyan transform fault (Martínez Catalán 2011).

2.3 The Cambrian sediments in the Central Iberian Zone

The CIZ; or Central Iberian Zone; is the largest zone of the Iberian Massif, and it forms an internal zone of the orogeny (Julivert et al. 1972; Diez-Balda et al. 1995) and is denoted with the yellow to grey colors on figure 2. The CIZ is defined by its stratigraphy, consisting of Upper Proterozoic and Lower Cambrian terrigenous sequences and transgressive sequences of the Lower Ordovician quartzite (Julivert et al. 1972; Diez-Balda et al. 1995). Another characteristic of the CIZ is the occurrence of large amounts of pre-Variscan volcanic and plutonic rocks, mainly in its northern and eastern parts. These can be related to the Cadomian Orogeny and Lower Paleozoic extensional events (Diez-Balda et al. 1995).

Important for the Cambrian rocks of interest is a phase of inversion leading to unconformities of Late Proterozoic and Early Paleozoic age (Diez-Balda et al. 1995). The Amorican Quartzite is located unconformably on top of the Proterozoic or Cambrian rocks and is dated 465 Ma (Bonjour et al. 1988). This formation mainly consists out of quartzites, but also contains some sandstones or slates, which represent a sub-tidal shelf environment (Diez-Balda et al. 1995). It is a well visible formation around the CIZ, since it is resistant to weathering and therefore is responsible for the hills in the terrain.

2.4 Study area

Three limestone formations were sampled to solve the problem. The first formation is the Tamames limestone Formation which is well exposed at the Tamames Syncline, found about 50 km south southwest of Salamanca and about 5 km southeast of the village of Tamames. The second formation is spread across Central Iberia where the Los Navalucillos Limestone Formation is exposed scarcely in between the more recent covers. Both formations are part of the Central Iberian Zone and the sampling localities are denoted with stars in figure 2. The last formation is a Carboniferous limestone found east of Cáceres in which a lot of quarrying is performed. Other than (Julivert et al. 1972) who produced a geological map and a description of the area, little information can be found. Only two sites have been drilled in this formation: DB7 & DB8.

The Tamames limestone Formation; as described by Corrales et al. (1974) and Díez Balda (1986); and the Los Navalucillos limestone Formation; as described by Menéndez Carrasco (2013) and references therein; show lots of similarities and are categorized as platform carbonates (Rodriguez-Alonso et al. 2004). Both consist of alternating limestones and dolomitic carbonates and are characterized by

significant differences in thickness (120-600m). In both formations are shallow tidal deposits with mud cracks, stromatolites and oncoliths observed. Also, reef facies are observed which are interpreted as a barrier for the tidal flats (Corrales et al. 1974; Corrales & Valladares 1980; Menéndez Carrasco 2013). According to Archaeocyatha (Menéndez Carrasco 2013) and Trilobite fossils found by Díez Balda (1986), the age of the both limestone formations is 515 – 509 Ma, consistent with Age 4 of the Cambrian period (Gradstein et al. 2012). Since these two formations are this similar, a suggestion can be made that these two formations belong to the same unit.

Corrales et al. (1974) and Diez Balda (1986) have produced a stratigraphical column of the Tamames limestone Formation which is digitalized in appendix A1.4. The Tamames limestone Formation has a gradual transition to the Tamames sandstone formation (Valladares et al. 2000; Ugidos et al. 2003). Both are unconformably overlain by the lower Ordovician Amorican Quartzite (Diez-Balda et al. 1995).

2.5 Earlier sampling campaign

An earlier expedition has been performed in the Tamames limestone Formation and some localities around western Iberia which are described in the master thesis of Groenewegen (2014). This earlier expedition is mostly used for the sites taken in the Tamames limestone Formation, indicated as PM3 to 10 throughout the report. These consist of multiple types of measurements as PM3 to 7 being single spot layer readings and PM8 to 10 are conventional paleomagnetic sites which can be added to the data pool. Magnetic susceptibility, rock magnetic and magnetic directions data are obtained which are used in this report. These can be found in the designated appendixes and will be discussed and used in the results and interpretations.

3. Methods

3.1 Sampling

We collected 382 cores in the field in the various localities as described in the geological setting of which 275 are drilled in the Tamames syncline; named TAM and PM respectively; and 107 in the Los Navalucillos formation named DB, of which 11 cores in DB1, 37 cores in DB2&3, 49 in DB4-6, and 21 in DB7&8. These cores are cut to standard sized samples of 10.5cm^3 with a diameter of about 2.5 cm. When possible, multiple specimens are retrieved from each core. Also, spare core parts are labeled and used for various tests where a complete sample is not required. Each drill hole per has been oriented and bedding measurements are taken and averaged per site.

The average GPS per locality is found in table 3 in the results section, while the GPS coordinates of each site can be viewed in the data repository. This also shows an overview of the bedding measurements as well as the borehole measurements. Localities can also be viewed in figure 2. The positioning of the different sites of the TAM-locality need some extra work, as they are used as stratigraphic column. The biggest TAM locality can be viewed in figure 3. TAM9 & 10 are sampled about 5 km to the east and are correlated to the shown locality using Google Earth.

A previous study of Groenewegen (2014) is partly focused on the same Cambrian limestones around the Tamames area. The data that is produced there is combined with own data throughout this study.

Figure 3: Google Earth image of the Tamames locality in which TAM1 to 7 and PM3 to 9 are collected. PM10, TAM9 & TAM10 are located about 4 km to the southwest of this.

3.2 Paleomagnetic methods

3.2.1 Thermal Demagnetization

This study mainly uses thermal demagnetization to unravel the magnetic directions required for paleomagnetism. The goal of the thermal demagnetization is to obtain as much magnetic directions as possible with the smallest errors possible. One direction per sample is taken.

Thermal demagnetization is performed using varying temperature increments in between 5 and 55 degrees Celsius, where the choice in temperature step is made by the expected decrease in intensity of the sample as described in detail in appendix A2.1. After heating and cooling of the sample in a field-free furnace, a double-sided NRM is measured with a 2G Enterprises SQUID magnetometer. The samples are measured in field-in and field-out positions and averaged afterwards to minimize errors. A pilot batch with varying temperature steps containing several samples of each site is used to find the optimal temperature steps. Measurements are terminated until full demagnetization or behaving directionally inconsistent for several magnetic steps. The samples are alternated between field-in and field-out position in the furnace to prevent stacking residual fields that might occur in the furnace.

All available samples have been thermally demagnetized. NRM values typically start at $3x10^{-3}$ Am^2 at 200 degrees Celsius which is usually the starting temperature, but there are exceptions with intensities up to two orders of magnitude higher. An overview of the temperature steps is given in Appendix A2.1. When rejected for further thermal analysis, the samples usually show intensities around $3x10^{-5}$ Am^2. The detection limit of the machine, which is $1x10^{-8}$ Am^2 for each axis, is far from reached, so accurate measurements can be ensured. The sample holder is measured before each batch and its base value must be below $30x10^{-6}$ Am^2. The stored holder intensity vector is deducted from each measurement. Small errors can occur due to small deviations in the position of the sample, but careful handling of the samples should minimize this error.

Characteristic Remanent Magnetization (ChRM) is determined in a Zijderveld (1967) plot using principal component analysis (Kirschvink 1980). This analysis is done using VPD, made by Rámon and Puyeo in 2010. Two criteria must be met order to accept the ChRM: the ChRM must contain out of at

least 5 points and the Maximum Angle of Deviation (MAD) must be smaller than 15 degrees. Fortunately, most of the ChRM consists out of 6 to 10 points and a MAD of 2 to 6 degrees.

3.2.2 Alternating field (AF) demagnetization

A second option for obtaining magnetic directions is AF demagnetization which could show different or higher quality results. There is no real method to say whether AF or thermal demagnetization shows better results beforehand, therefore both are tested and the results are compared.

16 samples have been measured for Alternating Field experiments on the in-house robot at University of Utrecht which is connected to a 2G enterprises DC SQUID magnetometer (Mullender et al. 2005). The samples are placed and glued in silicon cubes in which the sample is precisely oriented and measured per string of 8. The magnetometer uses an oscillating known field in a in a field free room to demagnetize the sample. The field strengths are shown in table 1.

Measurement	1	2	3	4	5	6	7	8	9	10	11	12	13	14	15
Field (mT)	0	5	10	15	20	25	30	35	40	50	60	70	80	90	100

Table 1: Field steps applied for AF demagnetization in mT.

The 16 samples have been checked for Gyroremanent magnetization (GRM), which is an artificial remanence magnetization that is acquired by stationary specimen in a moving field (Dankers & Zijderveld 1981; Stephenson 1993; Tauxe et al. 2010). Mostly, this is observed in AF demagnetization. The most recent hypothesis of the creation of gyroremanence is that small changes in the uniaxial constraint for small needle-shaped magnetic particles play a key role in GRM (Potter & Stephenson 2005).

3.2.3 Anisotropy of Magnetic Susceptibility (AMS)

AMS is measured to find preferred magnetic directions in a rock which can be caused by combined orientation distributions of magnetic minerals in the specimen. Anisotropy of magnetic susceptibility can be caused by large scale tectonic process or geological event or by sedimentary flattening of the rock (Borradaile & Jackson 2004). AMS can also be caused by earlier high field strength magnetic tests (Borradaile & Jackson 2004), which is prevented by performing AMS measurements before conducting any other experiment.

The anisotropy of the low-field (200 A/m peak-to-peak) magnetic susceptibility was measured for a selection of samples of every site an AGICO MFK1 Kappabridge at 200 Hz. By rotating around 3 axis, a At least 5 cores were measured per site to support a meaningful statistical result (Jelinek 1978). The most complete cores have been used to perform AMS analysis; others are excluded to prevent alteration of the vector due to an incomplete sample where air will be measured instead of rock. The principle of AMS and some interpretation methods can be found in appendix A1.1.

The AMS data is plotted using Anisoft 4.2, which is the standard package that belongs to the machine. This plots the available directions in a stereonet, while the mean bulk susceptibility, $\sigma 1/\sigma 2$, and $\sigma 1/\sigma 3$ can be plotted separately.

3.3 Rock magnetic methods

3.3.1 Thermomagnetic Analysis

Thermomagnetic analysis provides insight in the magnetic carrier of the sample, which can help to obtain insights in the magnetization of the rock. It can provide information on the dominant magnetic mineral and thus showing a ferromagnetic behavior, but it is not always successful as a significant amount of samples only show paramagnetic behavior.

A weighed sample of 45 to 125 mg of powdered material is loaded into a glass vial in between two layers of thermally conductive quartz wool. This vial is measured in a horizontally modified Curie balance of Mullender et al., (1993). The measurement consists of the increment of the temperature by 10°C per minute with intermediary cooling phases cooling 10°C per minute. The time steps are shown in table 2. After reaching 720°C, the temperature is cooled to room temperature. During these temperature steps the sample is subjected to a sinusoidally cycled magnetic field varying between 150 to 300 mT. The result is a horizontal displacement which can be measured using a seismometer and compensated using an automatic force compensator. This current required to keep the sample in place is calibrated to a magnetic moment by means of a calibration sample. In the thermomagnetic curve figures, these magnetic moments are plotted on the y-axis of the diagram, whereas the temperature is plotted on the x-axis.

The noise level of the Curie balance is $2 \cdot 10^{-9}$ Am^2, which is three orders of magnitude lower than traditional Curie balances (Mullender et al. 1993). The horizontal position of the sample counters the mass decrease or increase due to oxidation and therefore the error the machine has. The chemical alterations that are caused by the temperature changes can be shown by the reversibility of the thermomagnetic curve: if the curve is irreversible, thermal alteration of the sample has occurred. If there is no chemical alteration in the sample, the magnetic moment should decrease with increasing temperature. The magnetic carriers can be distinguished using shape analysis compared to known curves for this machine.

Step	0	1	2	3	4	5	6	7	8	9	10	11	12
Temp (°C)	20	200	150	300	250	400	350	500	450	600	550	720	20

Table 2: Overview of the consecutive steps used in the thermomagnetic analysis. A lower temperature step in between two higher steps indicates a cooling phase in which the signature of a mineral could arise depending on the mineral type.

3.3.2 Hysteresis loops

Hysteresis loops are an effective tool to find the state of magnetic minerals by small rock samples to an alternating magnetic field. Some primary observations on the diversity of magnetic minerals can be made by analyzing the shape of these loops, as well as an indication on grain sizes.

Hysteresis loops are performed on a Micromag 2900 alternating gradient magnetometer at Utrecht University, which uses a 2 to 5 mg sample with a pinhead size samples attached to a probe. Silicon grease is applied to maintain a vacuum state in connections of the various instruments and glassware. The probe is suspended between magnets which are cooled with water to prevent short-circuiting of the current. The magnets are fitted with coils, which control the gradients of the applied field. The hysteresis loop measurements are performed up to 2 Tesla. The response of the measuring equipment of the probe is not linear after 1.6 T. This is corrected using the pole-shoe correction, which assumes a magnetically saturated sample beyond a maximum of 1.2 Tesla, as stated in the

manual of the Micromag. After the hysteresis loop experiment, the measurement is corrected for paramagnetic behavior by converting the saturated lines to a horizontal position. This assumes saturation at 70% of the measurement maximum. The saturation magnetization (M_s), saturation remanence (M_r), and coercive force (B_c) are extracted from the slope-corrected plot as well the habit of the loop. The exact working of the machine is explained in Appendix A1.2.

Several parts of the plot have been used to be represented and interpreted in the squareness versus coercivity plot. This explains the remanence magnetization (Mr) as the crossing of the line through the y-axis and the coercive force (Bc) as the traversing of the x-axis. The saturation magnetization (Ms) is defined as the magnetization moment of all the grains is parallel to the applied field. If this is not the case after the maximum range of the machine (2T), a pole shoe correction is applied as explained above.

The shape analysis performed is mainly based on the symmetry of the two lines and the distance between them (equal to 2 times Bc). If the two curves are not parallel to each other, the sample is probably wasp-waisted.

3.3.3 Isothermal remanence magnetization (IRM)

Isothermal Remanence Magnetization (IRM) is used to further discriminate between magnetic carriers that are present. IRM can also be used to distinguish between grain sizes and magnetic intensities by use of the flipping field parameter, which is explained in section A1.2, which can further explain the magnetic state of the rocks.

The isothermal remanence magnetization measurements are performed on the in-house robot at University of Utrecht (Mullender et al. 2005). In total, 192 samples are measured in two batches of 96. The samples are weighed and do not need to be complete (10.5 cm^3). Before the experiment initiates, the samples are demagnetized using an alternating field of 300 mT to guarantee a similar initial state per batch and trying to make the acquisition curve cumulative log-Gaussian (Heslop et al. 2004; Egli 2004) which is a requirement for the processing of the data. During the experiment, the samples are glued with silicone kit in magnetically saturated epoxy resin cubes and per string of 8 transported through a 2G Enterprise DC-SQUID magnetometer. Every sample will be exposed 60 times to a known and increasing magnetic field in the longitudinal direction and measured afterwards to observe remanent magnetization. Isothermal Remanence Magnetization is based on the principle of applying a field on the sample followed by a relaxation of the magnetic field. The magnetically flipped domains (for explanation see the rock physics appendix A1.2) will remain in the most recent flipped state, and can therefore be measured.

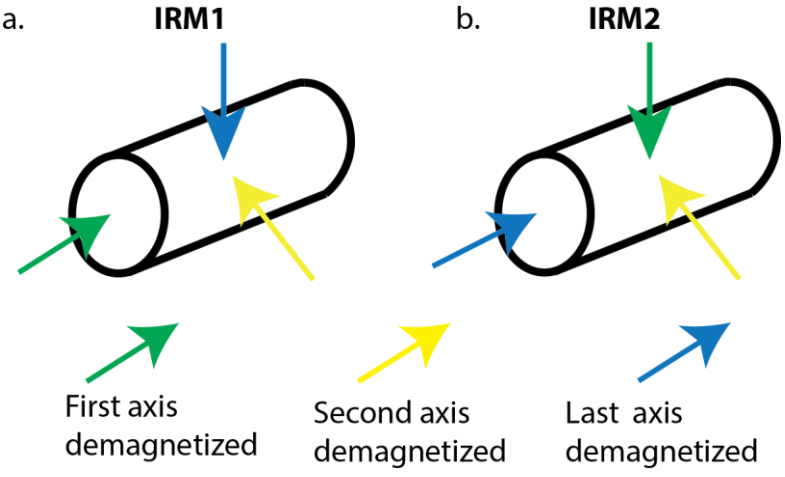

Figure 4: Visual representation of the order of the demagnetized axes in the two measured IRM sets. The final axis of demagnetization could be of influence on the magnetic result.

Important to notice is that there are two distinct sets of IRM measurements which cannot be mixed with each other. The difference between the two sets is the order of the axes that have been demagnetized, as is displayed in figure 4. IRM set 1, initially

consisting of 96 samples, has the cylindrical axis demagnetized the latest (figure 4a). IRM set 2 has the longitudinal axis demagnetized the latest and also consists of 96 samples as can be seen in figure 4b. IRM set 2 is treated in the text and IRM 1 in the appendices.

3.3.4 IRM unmixing

By unmixing the different habits of the IRM into family curves, a general habit could be found which might be indicative for the magnetization habit of the curves. This is done by several mathematic processes that are explained below.

Robertson & France stated in 1994 that the populations of magnetic minerals generally are conform to log-normally distributions. They argue and experimentally show that the IRM is the linear sum of all the contributing grains and therefore can be unmixed into the contributing components under the condition that each contributing magnetic mineral can be represented by cumulative log-Gaussian curves (Robertson & France 1994; Heslop et al. 2004; Egli 2004; Tauxe et al. 2010). This method is based on single domain minerals, so interaction between different minerals or states might interact and alter the curve. The log-Gaussian curves might give an indication on type, grain size, and concentration of the minerals or phases that can be found in the sample (Robertson & France 1994), in which the peaks are assumed to be correlated with coercivity components (Robertson & France 1994; Heslop & Dillon 2007). More mathematical information on the unmixing can be found in the paper of Weltje 1997, which is the designer of this solution.

Every curve is pre-processed: the base value that the tray has is subtracted from the total before the end member calculations are performed. Also, the remanence values have to be continuously rising, so interpolations are used on parts of curves where this is not the case. This could lead to rejection of several curves in which interpolation could excessively alter the shape of the individual curve. The interpolated curves are then combined to find end-members. For complex curves where interpolation is difficult, the remanent magnetization is processed using the procedure of Kruiver et al. (2001), based on Robertson & France, (1994). Some complex curves can be rejected for end-member modelling. The plots obtained by Kruiver 2001 show a linear acquisition plot (LAP), which can be differentiated to obtain the gradient acquisition plot (GAP). By applying normally distributed peaks in the GAP using position, mean value and standard deviation, a best fit will be produced.

A necessary assumption is that the data set is fully representative for the variability in the rocks. This assumption is attempted to be met by sampling in various layers, sites, and borehole orientations per site and using a large amount of samples.

3.3.5 End-member modelling

End-member modelling is performed on the IRM data in order to distinguish different mechanisms which can alter the minerals. This can show underlying processes that provide insight on the magnetization and a geological solution on the area.

The IRM curves are combined per IRM batch and statistically divided into end-members using a program of Heslop & Dillon, made in 2007, supported by a Matlab compiler. In the used application, 2 to 9 end-members can be selected. The final code will produce the end-member shapes, calculating end-member curves and contributions to these curves per sample.

The choice of amount of end members is based on the coefficient of determination (r^2), which ranges between 0 and 1 (Heslop & Dillon 2007). The model is not sufficient if the r^2 is below 0.5. The

optimal model shows a high r^2 value, but adding one end-member does not significantly increase r^2. If r^2 is plotted against the corresponding end-member number, the break-in-slope provides a useful guideline for the optimum number of end members: the steeper slope at the low number of end members is considered 'information' and the almost-horizontal slope at the higher number of end members is 'interpretational noise' (Dekkers 2012). A second criterion is based on the similarity of end-members. If two end-members have a (near) identical shape, the complete dataset has been overinterpreted and fewer end-members can be used.

3.3.6 X-Ray Fluorescence (XRF) measurements

XRF measurements are used to get a first insight on the chemical heterogeneity of the TAM locality which might be coupled to other properties that have been found in other methods. The chemical components can also be tested to check the magnetic carrier.

A selection of the TAM samples and DB6 are subjected to XRF tests using a Thermo instruments Niton XL3t handheld XRF stabilized in a radiation blocking container. The measured surfaces are first cleaned using alcohol. The XRF-machine is set to measure bulk analysis, measuring magnesium, calcium, silicium, copper, iron, aluminum, iron, chlorine, potassium, sulphur, and several other (minor) elements. The measurements are performed under a helium flow in order to provide a higher accuracy, although the net accuracy is not as big as a static XRF machine.

TAM1-1 has been measured throughout the whole cycle to check for inconsistencies of the machine. TAM5 was subjected to multiple measurements to provide insight on whether a different position in the sample would provide a different result. The rest of the samples are measured once. The results will give an insight in the chemical heterogeneity of the rocks over the sampled sections of the Tamames limestone Formation.

The measurement error of the machine is used to tell something on the accuracy of the machine. The errors of this machine are located in appendix A1.3.

4. Results

4.1 Lithological results

4.1.1 Preliminary lithological observations

The DB & TAM localities show brown to grey and slightly pinkish limestones with a patchy color distribution over the layers. The layers are dolomitized and metamorphosed slightly with tiny variations in intensity of these processes. The original layering is still visible and no metamorphic foliation is observed.

DB1 shows a grey to white limestone with clear grains. The limestones are relatively brittle in comparison to other sites. A big granite intrusion is present approximately 500m away.

DB2 to DB6 all show grey to brown limestones with clear bedding. DB2 is located in an abandoned mine. DB3 shows multiple folds next to each other, while DB4 is located on an anticlinal structure with measurements on both limbs. DB5 shows a somewhat higher metamorphic grade in comparison to others. DB6 is only party visible, the rocks with lower hardness are not visible.

DB7&8 are brown, gray to pink limestones with patchy coloring and a lot of visible pores. They are sampled next to a mine.

The TAM localities show an alternation of visible harder layers and are interbedded of softer layers which are not visible. The layers are mostly grey and brownish. The top of the ridge shows an angular unconformity to the Amorican Quartzite as stated in section 3.4. Some cores taken show small visible pores. The sites of TAM and PM are found in figure 5.

Several layers at the Tamames locality show patchy, roundish features in the limestones which makes the rock too brittle to drill regardless of the drilling direction. The patchy features appear to be concentrated in several layers as they can be followed laterally throughout several layers. The patchy structures can be linked to reefs or stromatolitic parts in the stratigraphic columns that are treated in the next section.

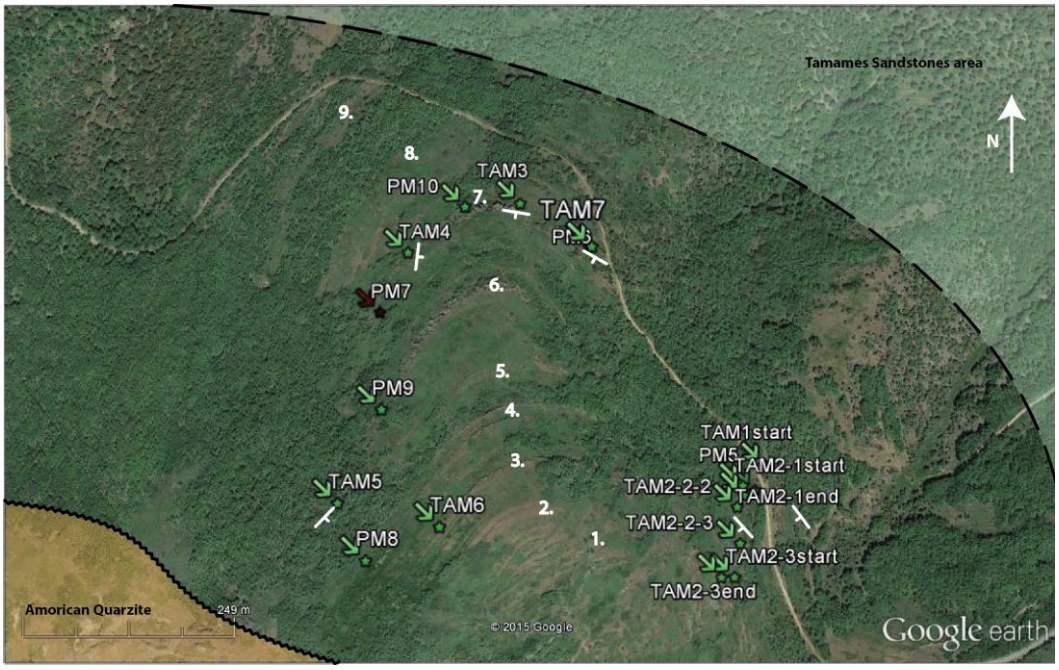

Figure 5: processed orthophotograph htat shows the Tamames Limestone Formation in the center. The strike and dip of the layers is highlighted with the appropriate symbols. The numbers correspond to figure 6. Note that there is an angular unconformity in the southwest to the Amorican Quarzite.

4.1.2 Stratigraphic column

The main input for the sedimentological results for the Tamames section is based on the TAM1-7 site by visual inspection of orthophotographs combined with observations taken on the sites. The overview of this section can be seen in figure 5 in which a Google Earth picture is overlain with various features. The locality of this site is shown in figure 2. This locality is a syncline through a hill, which can be concluded from the bedding measurements indicated with strike/dip signs. Important to notice is that the dip increases at the top of the hill and therefore the top of the formation. The topographic height difference between layer 9 and layer 1 is about 100 meters. The Tamames Sandstone Formation, which is below the Tamames Limestone Formation, is found in the right side of the map. The boundary is not mapped as the sandstone poorly cropped out. The unconformity of the Tamames Limestone Formation with the Amorican Quartzite is found in southwestern part of figure 5.

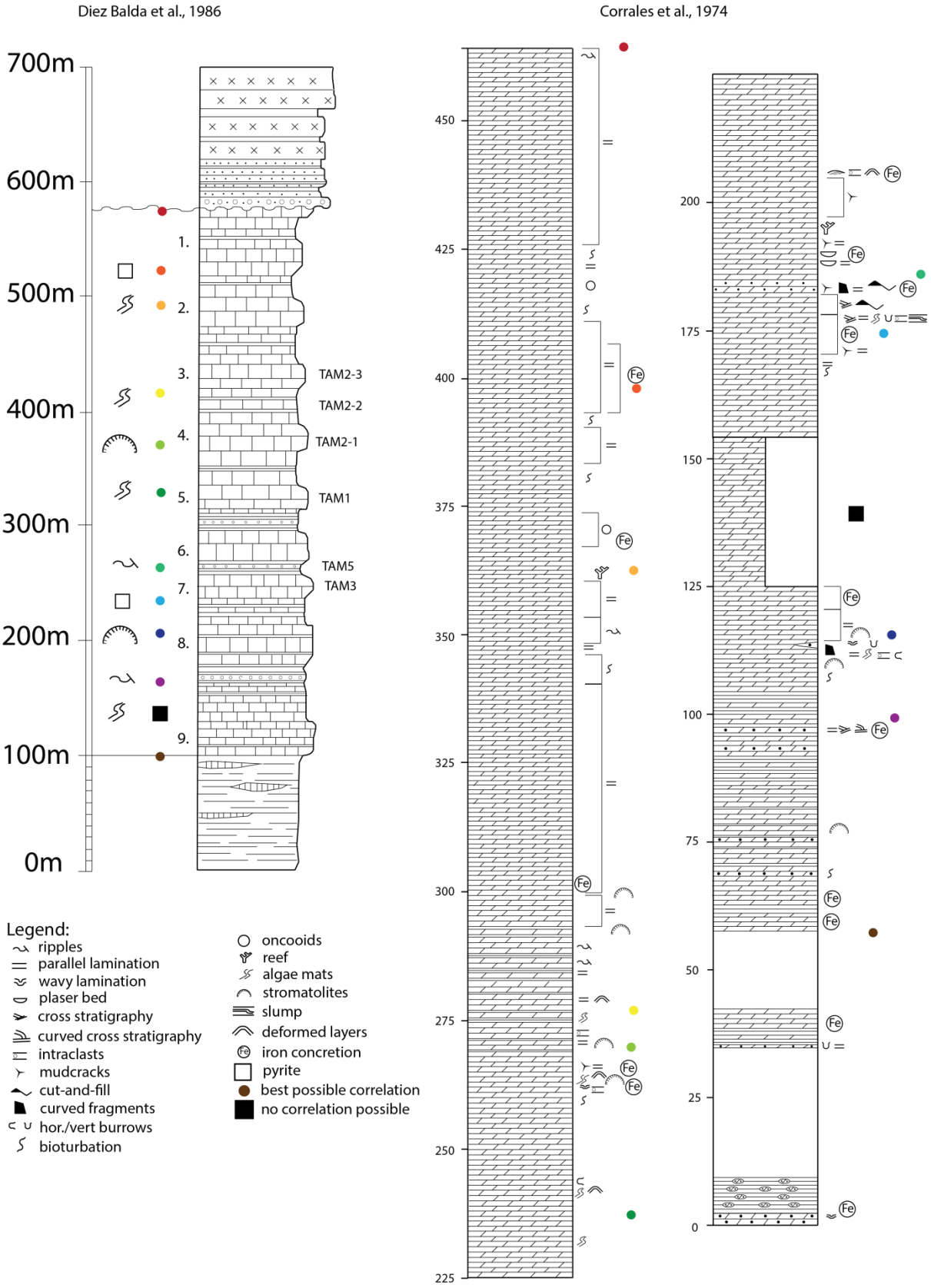

Figure 6: Digitalized stratigraphic columns of Corrales et al., (1974) and Díez Balda, (1986), with a scale in meters. The colored dots are a possible link between the two columns. The biggest sites have been denoted next to the column of Díez Balda, which is then used to produce the synthesis column in figure 7.

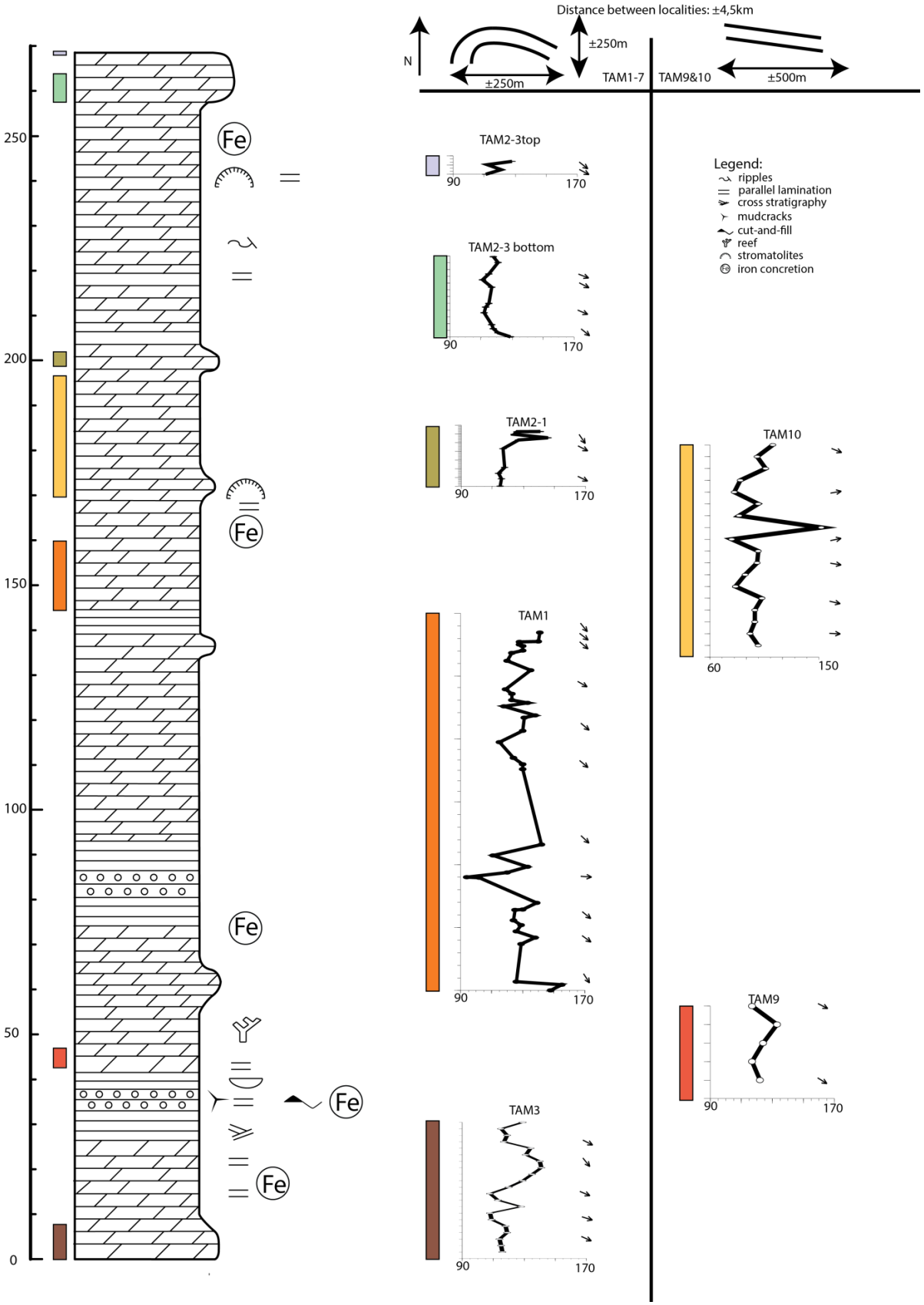

Figure 7: On the left side, a synthesis column in meters for the Tamames area is found which is formed out of the combined columns of figure 6 and own observations in the field. The bars correspond with the stratigraphic sites on the right, which have been split in two sites. The left columns show the sections from the TAM1-7 locality, which is shown in figure 3 and 5. The right columns have been taken approximately 4.5 km from there, but fit in the same formation and setup.

The first task is to rework and combine the two literature stratigraphic columns that are discussed in section 2.4. These are not logged at the same locality and are therefore not exactly similar, but show a good basis for correlation. The result can be observed in fig COL in which both columns are displayed. The correlation of the two columns is performed on distinct layers and regional fossil content which are marked with the colored circles. The black squares are parts that are not possible to correlate as they are not observed by the other column.

The columns now need to be related to the study area. The column of Díez Balda (1986) is used for this as this contains the relative hardness of the layers. The column of Corrales et al., (1974) is unsuitable for this, as the sampling campaign did not incorporate a large scale study on fossils and sedimentological content. The layers have been marked 1 to 9 in figure 5 and figure 6, which show the most likely fit based on the best exposed in the TAM1-7 area and the distance in between these layers. The TAM9 & TAM10 sites can be added to the TAM1-7 overview using the same procedure.

Using the sedimentological correlations, a synthesis column of the TAM1-7 and TAM9&10 localities can be produced by overlaying the hardness of the Díez Balda (1986) column with the regional fossil content of Corrales et al. (1974). The part of the column that has concentrated measurements is found by photographic analysis and is found around 230 to 460m in the left column in figure 6. The result is found on the left side of figure 7; the right side will be treated later on in the text. In the synthesis column local phenomena are disregarded, but more continuous features are preserved. The color bars stand for different stratigraphic cored sites.

4.2 Paleomagnetic results

4.2.1 Zijderveld diagrams & NRM-analysis

For the Tamames syncline, 237 samples were successfully evaluated for magnetic directions consisting of both TAM and PM cores. Los Navalucillos limestone is split in two localities: DB2 & DB3 has 30 samples, DB4 to DB6 consist of 43 valid directions, and DB7 & DB8 show 19 directions in the dataset. Adding these gives a total of 329 cores with a valid direction out of the 398 cores that have been investigated, which results in a 82.7% success rate. The statistics per locality can also be viewed in table NRM, which is located below in table 3. The criteria for selection are stated in the methods section. The temperature steps vary between 5 and 55 degrees Celsius and the maximum temperature is set at 350 °C for the majority of the samples. Several samples were heated to over 400°C, but all the samples started to show random magnetic directions and an increase in magnetic intensity. More information on the temperature steps can be viewed in Appendix A2.1.

Figure 8 shows selected orthogonal projections (Zijderveld 1967) of the TAM-samples and the DB-samples. Per site one or two samples are used that are representative for the site.

Some primary observations and remarks can be made when observing the Zijderveld projections. Most of the samples show consistent behavior and can be interpreted confidently. However, all cores of DB1 were not interpretable and therefore the complete site is rejected. The NRM shows some correlation up to 180 °C, but the signal is random when increasing the temperature. Samples like DB3-1-2 show a successful measurement, but are rejected because there is no clear line through the measurement points that follows the criteria. One of the main reasons for rejection to find a magnetic direction is little to no demagnetization. This has happened quite a lot in TAM9 and throughout several individual TAM & DB measurements. TAM2-2-3, TAM6, and TAM8 were undrillable and therefore do not contain measurements.

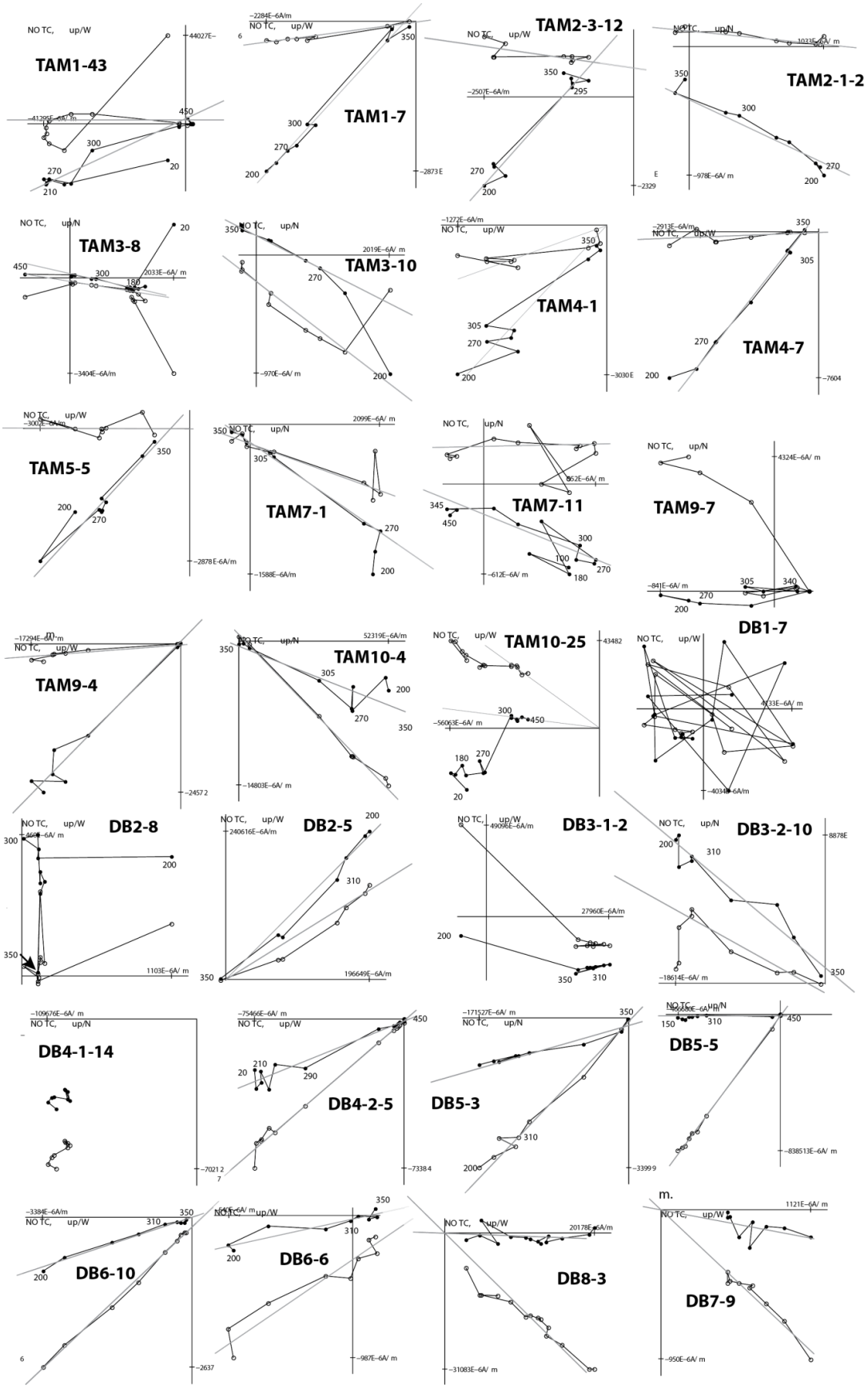

Figure 8: Overview of the different representative Zijderveld plots per site. All samples have been thermally demagnetized, with temperature steps shown in °C. Interpretations have been shown where possible. Closed (open) circles indicate projection on the horizontal (vertical) plane. All diagrams are in a non-tilt corrected reference frame.

Name	GPS N	GPS W	#site	#cores	#dir	#45	D	I	ΔDx	ΔIx
TAM & PM	40.61554	6.05982	17	272	237	231	123.9	9.6	2.1	4.1
DB1	39.45386	3.61084	1	11	0	0	-	-	-	-
DB2-3	39.40109	3.71514	2	44	30	22	132.9	15.3	9.4	17.7
DB4-6	39.6602	4.63596	3	49	43	34	151.4	22.1	6.3	11
DB7-8	39.44242	6.33717	2	21	19	14	347.3	48.6	7.6	7.7

Name	k	a95	K	A95	A95min	A95max	El	E	Eu
TAM & PM	16.2	2.4	20	2.1	1.4	2.7	1.56	2.01	2.79
DB1	-	-	-	-	-	-	-	-	-
DB2-3	7.4	12	12	9.3	3.5	11.7	1.42	2.52	7.13
DB4-6	9.3	8.5	17	6.1	2.9	8.9	1.68	3.51	9.47
DB7-8	47.9	5.8	37	6.6	4.2	15.6	1.48	3.16	27.45

Table 3: Overview of the paleomagnetic statistics per locality. For DB1, no usable results are found, hence a dash is used. GPS N/W = GPS coordinates. #site = amount of sites (no discrepancy between stratigraphic and regular sites), #cores = amount of cores per locality, #dir = amount of cores with a valid magnetic direction, #45 = amount of magnetic directions which pass the 45-cutoff, D/I = average declination/inclination, ΔDx/ΔIx = error in declination/inclination calculated from the A95, k = precision parameter associated with site means, a95 = confidence cone associated with site means K = precision parameter based on the Virtual Geomagnetic Pole (VGP) scatter, A95/A95max/A95min = cone of confidence/maximum value/minimum value determined from VGP distribution based on Deenen et al., (2011), El/E/Eu = lower/mean/upper elongation parameter based on paleosecular variation (PSV).

The ChRM directions are shown in figure 9a to 9d and are split per locality. The outliers, 27 in total out of 329, are excluded by using a fixed 45 degree cutoff per site and are shown in the red colors. Figure 9a shows only 6 outliers in 237 samples with an elongated cluster around 90 to 150 declination with low inclination. For DB2 & 3, 22 out of 30 directions are determined to be valid and clustered directions. The cluster appears around a declination of 135. DB4 to 6 contain 9 outliers out of 43 and again has a cluster around a declination of 150 with low inclination. Note that the inclination seems to shallow with increasing declination in the Tamames and first two Los Navalucillos localities. DB7&8 have a cluster around a declination of 350 and an inclination around 40 consisting of 14 out of 19 measurements. The different position of the cluster of DB7 & DB8 means that it is highly likely that they have not had the same magnetization age as the other localities. Therefore it is excluded from the data from now on.

7 samples are flipped in polarity to fit them in the major second quadrant. The marking could be inversed by accident or a reversal of the Earth's magnetic polarity has occurred, this can be checked in the discussion to check for verification when the dating of the magnetization is complete.

The ChRM is uninfluenced by stratigraphical successions. The single layer readings (PM3 to PM7) show consistent magnetic directions with small errors, while the stratigraphic sections show little to no trending, which could be an important indication of remagnetization.

Several samples were AF demagnetized, but the results were not interpretable. The TAM-samples that were not magnetically depleted at 350 °C were checked for gyroremanence, which was not found.

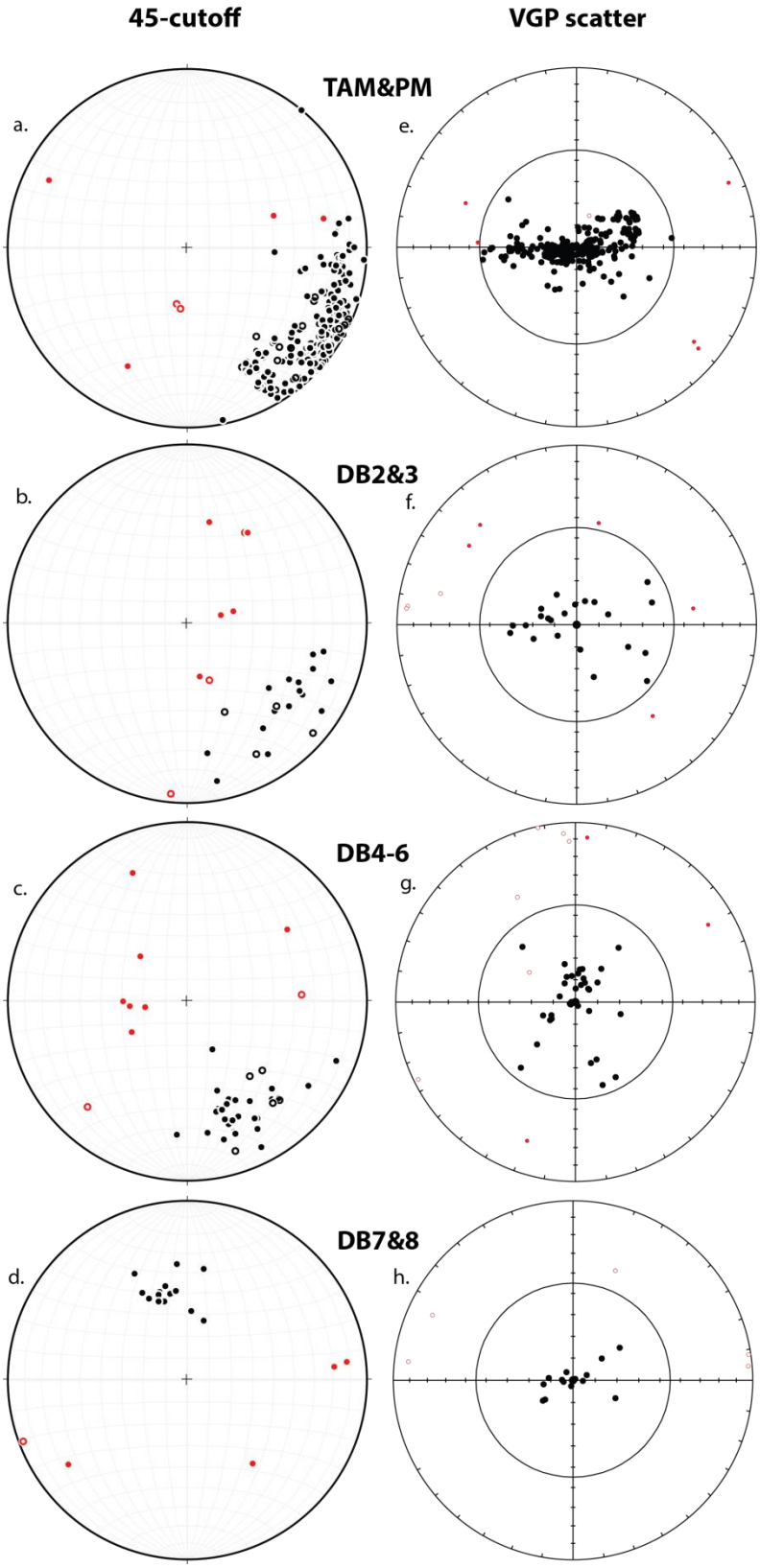

Figure 9a-d: Equal area projections of the ChRM of each locality in which the 45 cutoff has been applied per site. Open circles show upper hemisphere projection, closed circles are used for the lower hemisphere. The rejected directions are shown in red. E-h: VGP scatter per locality, again showing the cut off samples in red. Note that the VGP scatters are elongated.

The scatter of Virtual Geomagnetic Pole (VGP) of each locality is shown in figure 9e to 9h. As can be observed, all the scatters of the VGP show elongation either east to west or northwest to southwest. The statistics on paleosecular variation (PSV) of Deenen et al. (2011) are considered to check for the reliability of the data. The A95 values of the localities are consistently in between the $A95_{min}$ and $A95_{max}$. More importantly, the VGP shows an elongated scatter, which is indicative for either flattened sedimentation or deformation (Tauxe et al. 2010). This will be covered in the discussion.

The declinations of the stratigraphic order cored sites of TAM can be plotted in the synthesis column as shown in figure 7. In this figure, the different magnetic stratigraphic columns of TAM1-7 and TAM9&10 are linked to the column. Note that the open circles show a non-measured stratigraphic distance, while the closed dots of TAM1 and TAM2 are measured distances. All the declination plots are shown from 90 to 170 except for TAM10, which is shown from 60 to 150. The arrows next to the columns represent the declination as well. Although there seem to be subtle changes across the stratigraphy, no absolute arguments can be found for some kind of magnetic cyclicity in the area.

The localities, except for DB7&8, have been subjected to a fold test as used by Tauxe & Watson (1994), in which the complete

locality is used in one test. The fold axis position is determined before the fold test is executed. A preliminary correction towards a vertical fold axis position is needed if the fold axis is more tilted than 10 degrees as the fold test only takes vertical folding into account. The results can be seen in figure 10 which shows the unbending percentage on the x-axis and the eigenvalues of the major axis on the y-axis. For the TAM & PM data, the 95% chance envelope can be observed between -15 and 5 percent unbending, resulting in a negative fold test. The DB2-3 and DB4-6 fold tests show both a 95% chance envelope of -60 to 23 percent unbending. -60% unbending is the limit that this test is supposed to have, making this both inconclusive tests. This is probably caused by the lower amount of samples per test, while the samples are still experiencing a similar spread in comparison to the TAM samples.

All fold tests show results that are found display low to negative percentages of unbending. This leads to the conclusion that the magnetic fabrics must have been formed during or after the latest major tectonic event, which is the oroclinal bending of the Variscan. This would time the remagnetization in between 310 and 290 Ma. This also explains the lack of coherent cyclicity in the stratigraphic sites. More on the physics behind the remagnetization can be found in section 4.3 and on.

4.2.2 Anisotropy of Magnetic Susceptibility (AMS)

The results of the AMS measurements can be seen in figure 11. The majority of the mean bulk susceptibility values are higher than 10^{-6} in all the samples indicating a ferromagnetic carrier (Hrouda & Jelinek 1990).

The Tamames cores (no PM cores are included in these measurements), the DB2&3, and the DB4-6 localities show no general trend in geographic or tectonic projections (figure 11a to 11c). This can be explained by the relative anisotropy plot as most of the samples are located between 0.5% and 1.5% with some outlies that reach a maximum susceptibility differential of 2.5%. The majority of the samples are located near the detection limit of the machine, which leads to the conclusion that there is very little to no anisotropy in the rocks. The mean bulk susceptibility is mostly around $3x10^{-4}$ SI, although some exceptions can be found mainly in DB2 which have a lower mean bulk susceptibility (around $5x10^{-6}$ SI), but show a higher anisotropy of up to 11%. Most of the cores that had this higher anisotropy were not able to show a valid magnetic direction and thus were of little influence on the magnetic directions. The vast majority of the samples show little to no anisotropy in magnetic susceptibility, which

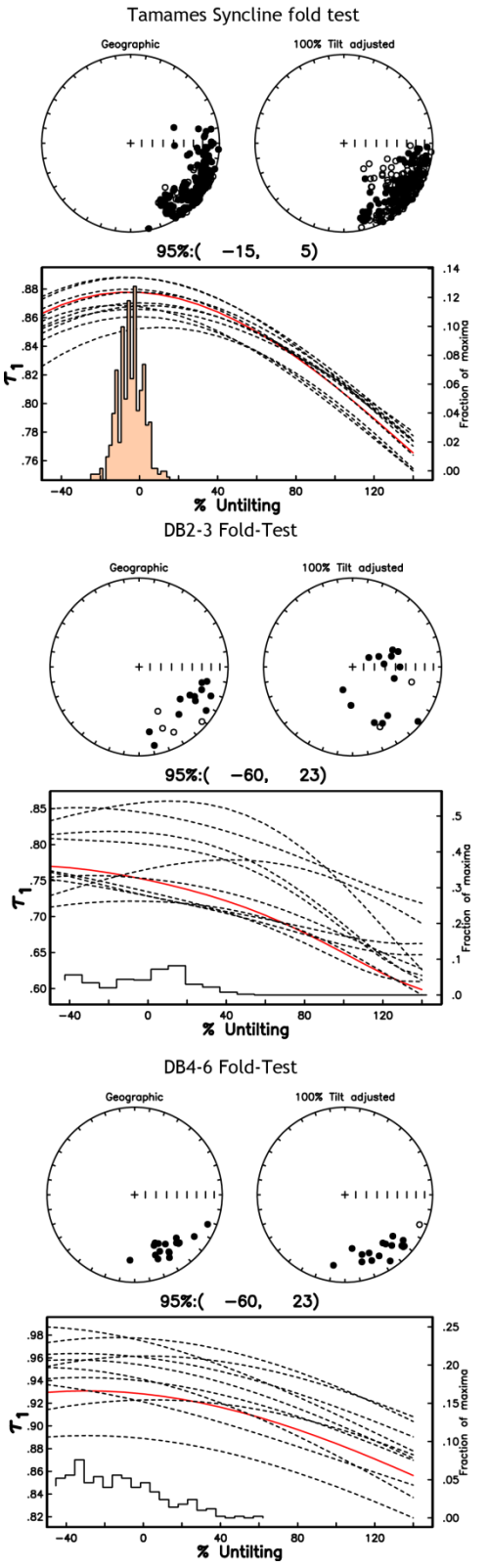

Figure 10: Fold tests of the three major localities. The τ1 parameter represents the largest eigenvalue of the orientation matrices from representative para-datasets taken from the original data population. The circles show the geographic and tilt corrected ChRM, while the bottom graph shows the best fit for vertical unbending percentages.

actively prevents biased magnetic directions in the section above.

DB7&8measurements, displayed in figure 11d, show different habits with a ribbon of κ1 directed southwest to northeast which is shifted towards a north to south orientation in tectonic coordinates. The samples show an anisotropy ellipsoid with up to 7% anisotropy measurements. The mean bulk isotropy is lower in comparison to the other localities: about 5.7 x 10^{-5} SI.

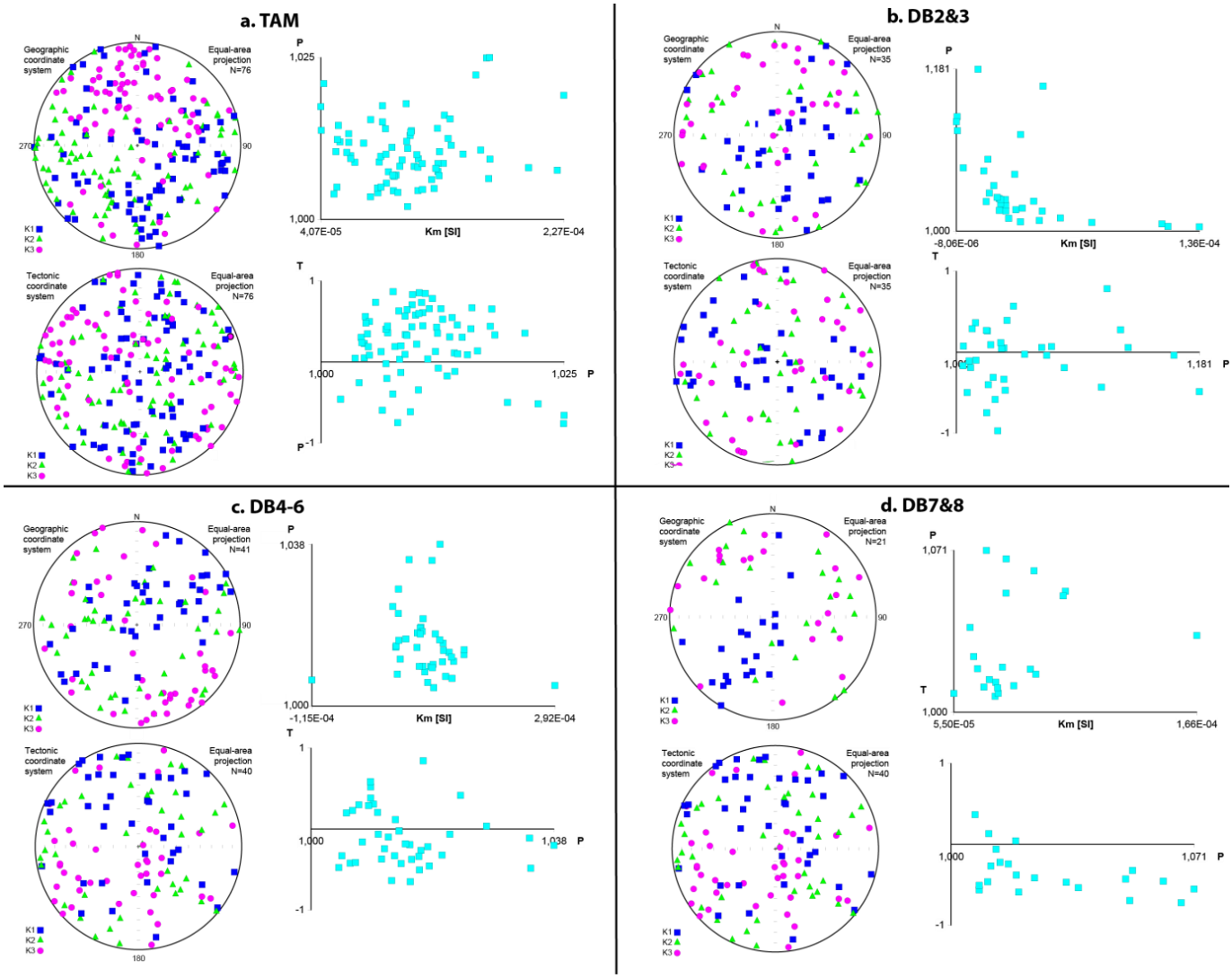

Figure 11: AMS plots of the different major localities in which κ1 (maximum magnetic susceptibility direction) is represented by blue squares, κ2 by green triangles, and κ3 (minimum magnetic susceptibility direction) by purple circles. Every top right graph shows anisotropy on the y-axis and mean bulk susceptibility on the x-axis. The bottom graph shows the rounding of the anisotropy ellipse versus anisotropy on the x-axis.

4.2.3 Apparent Polar Wander Path (APWP) for Tamames

A paleolatitude can be extracted from the TAM directions without prior knowledge of the ages of the sampled rock. Starting point are the accepted directions of the 45 cutoff as shown in figure 9a. Sorting the accepted directions on declination, a moving average of the accepted Tamames directions can be obtained. Figure 12a shows an untouched moving average with error bars of every point using 30 points per averaged measurement point. It shows that there is a relative overrepresentation of the data in between declinations 110 and 120 as this boundary is narrow. This

moving averaged is then smoothed and restacked to five points which are then converted to an apparent polar wander path (APWP). Figure 12b displays the APWP of Iberia (Torsvik et al. 2012) combined with the APWP from the Tamames using paleomagnetism.org software (Hinsbergen et al. 2015; Koymans et al., submitted). No direct fit can be observed in the APWP, and further discussion shall be held in section 5.2.

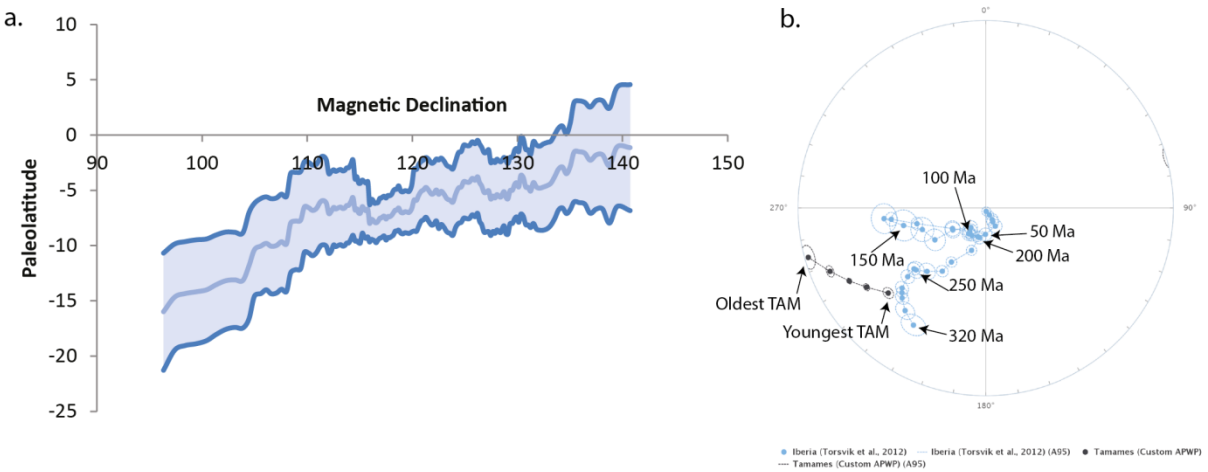

Figure 12a: Moving average of 30 points per point of the Tamames locality in which the declinations have been sorted and shown against the paleolatitudes. b: Apparent Polar Wander Path of Iberia in blue, Tamames area in black.

4.3 Rock magnetic results

4.3.1 Thermomagnetic analysis

The results of the thermomagnetic analysis are shown in figure 13, in which temperature is shown on the x-axis and magnetization on the y-axis. One sample from PM3 (figure 13a) shows a sharp drop in magnetization between 200 and 300 degrees Celsius followed by a drop in magnetic intensity in between 300 and 350°C. This is typical for a pyrrhotite (Fe_7S_8) bearing sample, which has an unblocking temperature around 325°C and a narrow temperature interval of 10 to 50 °C for complete unblocking near this Curie Temperature (Appel et al. 2012). As these intensity drops are observed at the same temperature ranges in the vast majority of the samples that have been thermally demagnetized, it is concluded that pyrrhotite is the main magnetic carrier in the TAM, PM, and DB samples.

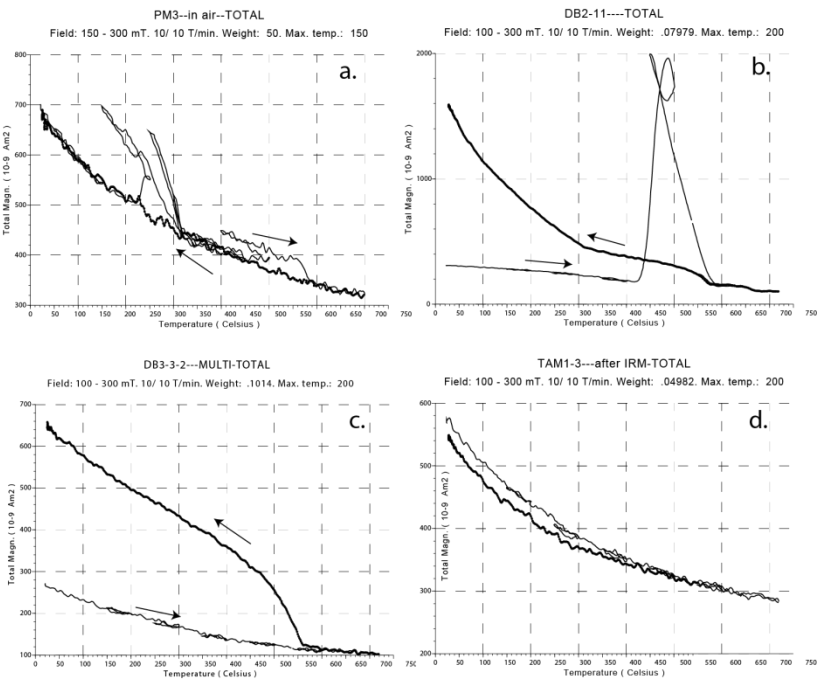

Figure 13: Overview of the different thermomagnetic plots trends showing temperature on the x-axis and total magnetization on the y-axis. The thin line represents the heating curve and the thick line represents the cooling curve.

Pyrrhotite is an iron sulfate which is generally found in remagnetized rocks, which can confirm the remagnetization observed in section 4.2. It has a ferromagnetic susceptibility component value bigger than 3.2 [SI] (Hrouda 1986; Borradaile & Jackson 2004) and is hard to detect in a Curie Balance as the susceptibility is low. Pyrrhotite is formed by the remineralization of magnetite and pyrite (Ferry 1981; Tracy & Robinson 1988) above 200°C in a reductive environment (Lambert 1973; Hall 1986), or via desuphidification (Carpenter 1974; Hall 1986). The occurrence of pyrrhotite in low-grade metamorphic sediments is a general phenomenon, especially in marly limestones (Appel et al. 2012). The conditions under which pyrrhotite grows best consist of marly carbonate rocks (because of reductive conditions and presence of Sulphur) with peak metamorphic temperatures just above the Curie temperature of pyrrhotite (Appel et al. 2012). Pyrrhotite is a very long mineral which could influence the magnetic directions when the crystal structure is aligned to the magnetic directions. However, the AMS research conducted in this study proves that this is not the case in this study. Low weight percentages of Pyrrhotite (~0.2 wt%) may outweigh other minerals in the AMS analysis due to high κ(Borradaile 1988; Borradaile & Jackson 2004).

The second trend type shows a nearly equal trend for the cooling curve (the thicker curve) and the heating curve. This is interpreted as a minor amount of magnetite in this sample and shown in figure 13b. Figure 13c shows DB2-11 which has a big peak around 400 and 500 degrees Celsius in the heating curve (the thinner curve). This is interpreted as a pyrite-bearing rock. The final curve shown in figure 13d, which shows a big hyperbola in the cooling curve which ends with a higher total magnetization at 20 degrees than the initial heating curve. This is typical of a paramagnetic curve and these are common throughout the dataset that is obtained.

The rest of the measured curves can be found in Appendix A2.2, although the major trends have been covered in this section.

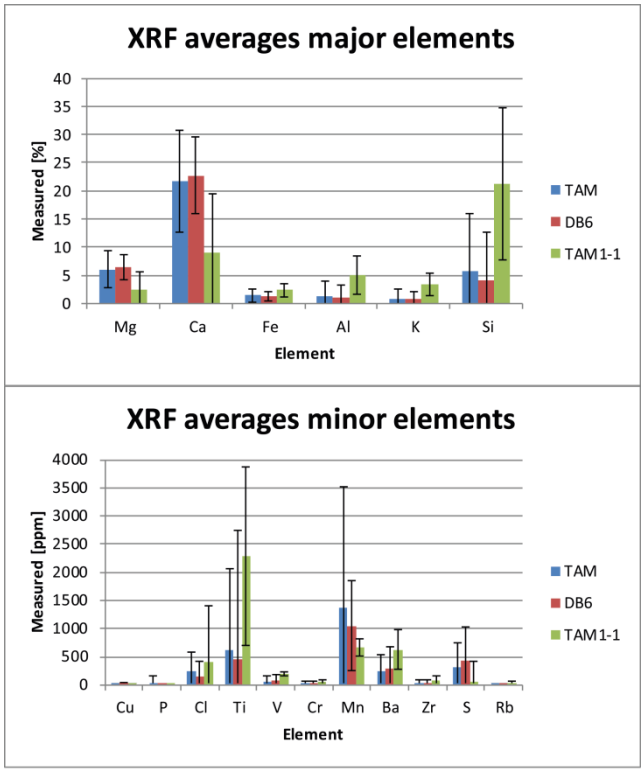

Figure 14: Overview of the major (in %) and minor (in ppm) measured elements of the bulk XRF measurements. The lines indicate the possible error using two standard deviations. The TAM1-1 sample has been measured multiple times for consistency.

4.3.2 XRF

The vast majority of the samples of the Tamames locality have been measured (in total 172 samples) as well as DB6 (14 samples). TAM1-1 has been measured 12 times in between the different measurements for consistency checks throughout the samples and to check errors in measurements. The bulk findings can be found in figure 14, in which is a distinction is made between larger quantities of elements and smaller ones to improve readability. The error bars represent two times standard deviation for the averages of each element per locality. The percentage that is not covered in the graphs is made out of "Balance", which is a combination of light elements that are not readable by the machine to fill to a 100% in the data. Also, several other larger elements that are measured by the machine only show the minimum value of 1 ppm with a larger error and are therefore they are most probably not present in these rocks. All the raw

results can be observed in the data repository.

The first conclusion that can be drawn is that the errors are quite large, most of the time for than 50% of the value that this element has. This is caused by the measuring device. Measuring one sample multiple times will not significantly improve the data, as TAM1-1 is measured 12 times and still shows significant errors as is displayed in the right column of figure 15. The low amount of chlorite is an indication that measurements are sensible, as little to no chlorite should appear in rocks. Appendix XRF can be consulted for all the raw data for the XRF measurements.

In figure 15a and 15d, an overview of the XRF measurements for TAM-samples and DB6-samples is shown in a tri-axial plot in which one axis fits for calcium, and magnesium, one axis for silica and one for potassium, iron, and aluminum in which the different symbols represent the different sites as seen in the legend. The axes roughly represent the main measurable elements for limestones, sandstones and clays. The plot shows a line running from Mg/Ca towards 65 to 70% Si and 30 to 35% K/Fe/Al. Most of the lower Mg/Ca values can be observed in TAM1. This can be used to say something on the depositional environment whether a layer contains more calcareous or marly content.

Figure 15b shows the same set of TAM samples with site-symbols with iron on the y-axis and silica on the x-axis and figure 15e shows the same for the DB6 samples. There tends to be a baseline where iron increases slightly with increasing silica content, but there is a significant amount of samples which appear to be enriched in iron.

Figure 15c and 15f show the results for iron versus Sulphur on TAM samples and DB6 respectively. There is a big cluster observed in both of the graphs, as no real line can be spotted. The 0 measurements of the sulphur are probably errors, as all these samples have pyrrhotite as main carrier and should therefore contain sulphur. Yet, a striking conclusion for this plot is the low amount of sulphur that is present in the rocks, which is an indication of a low percentage of the rock being pyrrhotite.

The XRF measurements have been tested against magnetic directions, end-member contribution, directions, and colors of the samples. Unfortunately, none of them gave a correlation. The spread of each site varies though: samples collected on site locations are

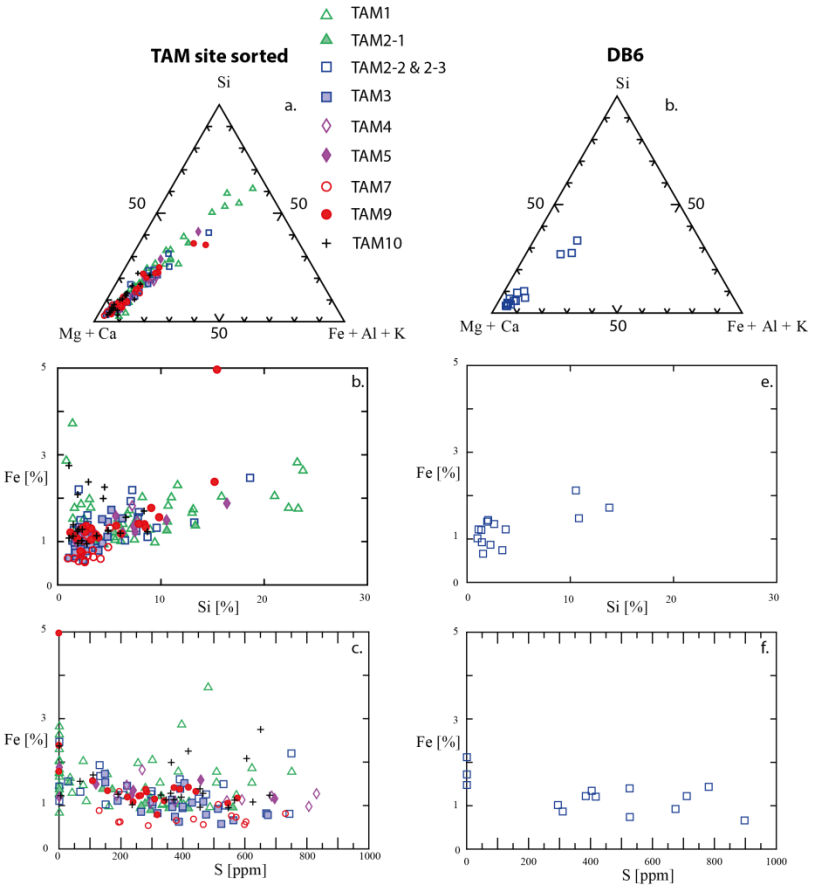

Figure 15: overview of relevant chemical ratios in the Tamames area (left) and DB6 (right). The plots are mostly in percentages, only the bottom plot uses sulphur in PPM on the x-axis.

located in a close cluster, while the stratigraphic column samples of TAM1, 2, and 3 are have a higher dispersion. This effect can be explained by the fact that the stratigraphic samples cover more layers and therefore show a further spread. TAM7 has several cores that were drilled in the same layer, but still varying in composition. This can be combined with multiple measurements of the same sample TAM1-1, as seen figure 15, with a measuring scatter. These factors combined can be interpreted as strong geochemical heterogeneity across the Tamames syncline in which not only a difference in geochemistry across layers, but also across positioning in this syncline.

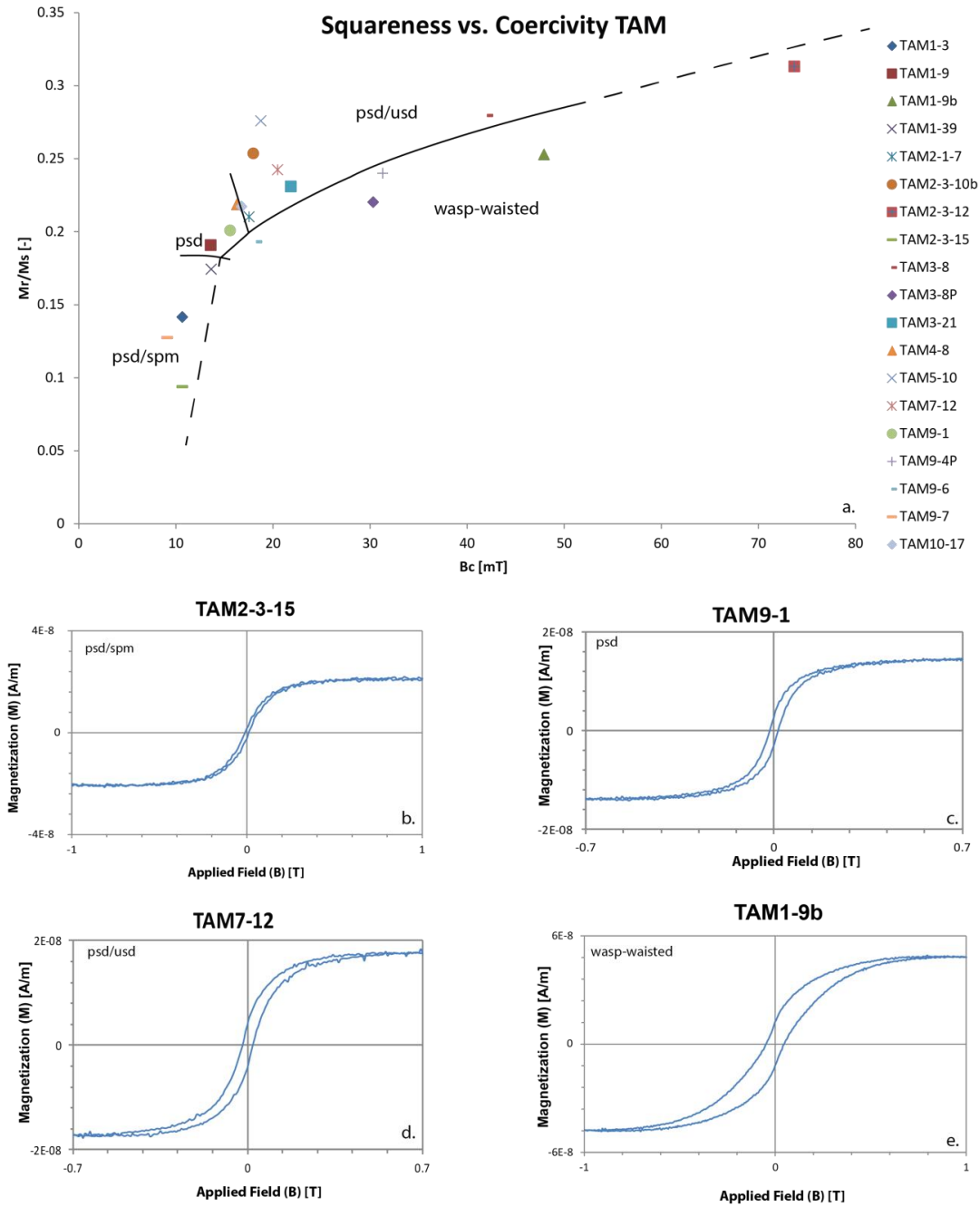

Figure 16: Squareness (Mr/Ms) vs Coercivity plot of all Tamames area hysteresis loop measurements. The striped lines in between the magnetic domains are uncertain, while the full lines represent more certain boundaries. The shape analysis shows different habits, which are also shown below with applied field in T on the x-axis and magnetization in A/m on the y-axis.

4.3.3 Hysteresis loops

The results of the rock magnetic analysis are shown in figure 16. First, the individual curve trends will be addressed, followed by a combined plot.

Different styles of hysteresis loops can be distinguished in the set of samples, as shown in figure 16b to 16e in which the magnetization is shown on the y-axis and the applied field on the x-axis. The applied field switches between 0.5, 0.7, 1.0, and 2.0 Tesla while making sure the samples are all saturated. Figure 16b is the measurement of TAM2-3-15, which shows a very tight to closed loop, which is inferred to reflect a superparamagnetic (SPM) to pseudo single domain (PSD) state. 16C shows a more open hysteresis loop in which the two lines open in a symmetrical fashion, showing a PSD style sample. A PSD to USD (uniaxial single domain) state example is shown for TAM7-12 (figure 16d) in which the loop has a wider opening which continues further into the more horizontal section. Some of the samples like TAM1-9 show wasp-waisted hysteresis loops, of which an example is shown in figure 16e. The complete set of measurements can be found in appendix A2.2, which shows similar styles as shown here.

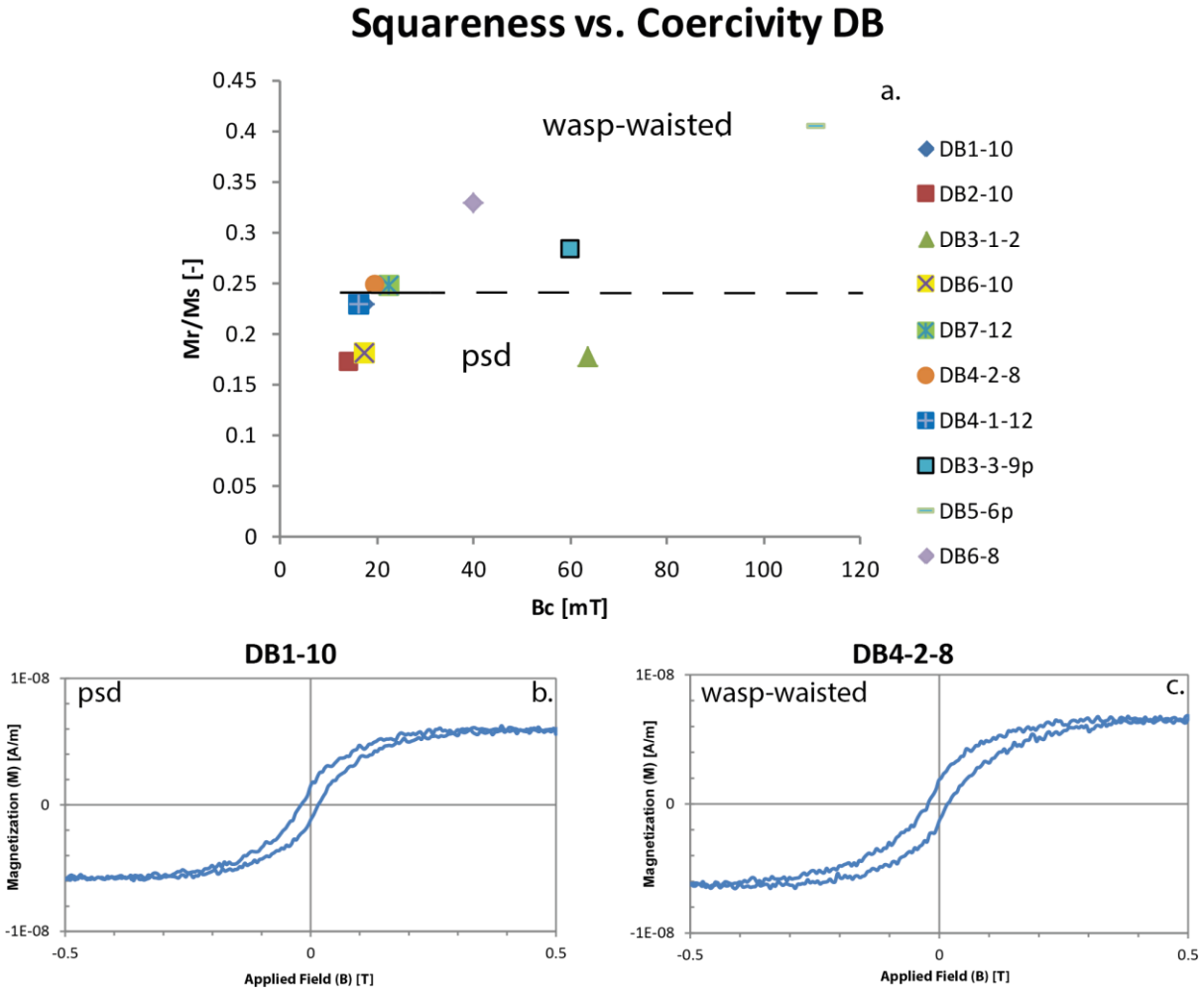

Figure 17: Overview of the squareness vs. coercivity plot of the DB samples with appropriate examples for the shape analysis. The axes are the same as in figure 16.

Combining the habit of the different samples, a separation is made of different fields in the squareness vs coercivity plot, shown in figure 16a. This shows an overview of the different types of hysteresis loops in which the squareness is plotted on the y-axis and the coercivity in millitesla on the x-axis. It is the first time that such a plot has been produced for pyrrhotite. The solid lines are

denoted as certain boundaries, whereas the dashed lines are less certain as fewer measurements are located in those areas. Clustered measurements are observed in between 15 and 25 mT of coercivity and a squareness of 0.18 to 0.25. The rest of the samples are spread out over the plot.

The same procedure can be followed for the DB samples. Two samples have been highlighted; the rest of the hysteresis loops can be found in the appendix as stated above. DB1-10 has a closed hysteresis loop at 0.5 T while both the curves are parallel around B=0 (figure 17b). This can be classified as PSD style behavior. DB4-2-8 shows a broader distance between the curves at B=0.1 T than at B=0 T. This is interpreted as a wasp-waisted sample.

The DB samples show a different pattern in the squareness versus coercivity plot in comparison to the Tamames samples in figure 17a, though fewer samples were measured. Figure 17a shows a cluster of samples at Mr/Ms around 0.2 and a coercivity of 15 to 20 mT. Some outliers can be observed around this cluster. Interpreting all the samples, a line can be drawn between the PSD and the wasp-waisted samples. The trend of this line is uncertain and therefore kept horizontal. Nevertheless, the position in between the different samples is correct, but more samples need to be measured in order to place the curves in the correct position.

Due to the low amount of measurements, a problem arises when considering the differences between the Tamames plot and the Los Navalucillos plot. The Tamames plot shows the wasp-waisted Multi Domain (MD) samples below the PSD/UD samples, while the DB samples situates these MD samples at a little higher squareness. The difference between the two different plots could be explained with a possible mineral composition change in which different minor compositions of secondary minerals play a role. This could lead to alteration of the different boundaries, but it will need more measurements.

Important to observe is the coupling of the rock magnetic results in combination with the NRM. DB3-3-9 shows incomplete demagnetization at 350°C while having a wasp-waisted hysteresis loop. This shows an influx of a secondary mineral. The prone candidate for this is magnetite, as it has been showing itself in low amounts in the thermomagnetic analysis.

The measurements that are shown in figures 16 & 17 show a consistent behavior of PSD to USD in most of the cases. The Mr/Ms values can be translated to grain sizes as stated by Dekkers (1988) which uses various parameters to couple these to grain sizes. The Mr/Ms is chosen since this is the only variable which is known. The two curves that have been used were the TTE and EGI curves of Dekkers (1988), in which the TTE represents a pure pyrrhotite and EGI represents a combination of pyrrhotite and magnetite. The composition of the EGI is changing over the grain size fractions in which the ratio of pyrrhotite to magnetite shifts more towards pyrrhotite with reducing grain sizes. The wasp-waisted measurements have been excluded from the TTE measurements as they do not contain pure magnetite by default. The results can be shown in table 4 which is sorted with increasing Mr/Ms. A first hand conclusion is the increase in Mr/Ms shows a sizable change from SPM/PSD tot PSD to USD type hysteresis loops.

The TTE grain size curve concludes that the individual grains should be larger than 200 micrometer (the final measurement of the curves), indicating that the minerals can be seen without magnification. This is not the case, as the grains are not visible by visual inspection of the samples. The grain size parameters can be influenced by minor additions of a second mineral, which could be linked to magnetite. This sets the stage for the EGI results, which seem more reasonable with parameters from 180 µm to 9 µm. The grainsizes will not be precise, but more an indication as the concentrations of pyrrhotite in both the EGI grainsize curves and the samples researched in this study varies throughout. Another option is the influence of superparamagnetic particles of a few

nanometers thick which could be largely present in the rocks. The presence of magnetite is most likely due to the results of the curie balance of several samples, which point to very minor additions of magnetite.

NAME	Mr/Ms	Hys. Loop state	TTE Mr/Ms grainsize [µm] (Dekkers 1988)	EGI Mr/Ms grainsize [µm] (Dekkers 1988)
TAM2-3-15	0.0938189	SPM/PSD	200+	180
TAM9-7	0.1274371	SPM/PSD	200+	60
TAM1-3	0.1415183	PSD	200+	45
TAM1-39	0.1743407	SPM/PSD	200+	40
TAM1-9	0.1908021	PSD	200+	32
TAM9-6	0.1930435	wasp-waist		32
TAM9-1	0.2008505	PSD	200+	30
TAM2-1-7	0.2101178	USD	200+	28
TAM10-17	0.2171642	USD	200+	26
TAM4-8	0.2186528	PSD	200+	24
TAM3-8P	0.220288	wasp-waist		20
TAM3-21	0.2308806	USD	200	15
TAM9-4P	0.24	wasp-waist		14
TAM7-12	0.2424382	USD	130	13
TAM1-9	0.2528688	wasp-waist		13
TAM2-3-10	0.253577	USD	100	13
TAM5-10	0.2759016	USD	65	11
TAM3-8	0.2795082	USD	60	10
TAM2-3-12	0.3131713	USD	45	9
DB2-10	0.1717	USD	200+	40
DB3-1-2	0.177	USD	200+	40
DB6-10	0.1816	USD	200+	35
DB1-10	0.2286	USD	190	18
DB4-1-12	0.2289433	PSD	190	18
DB4-2-8	0.2471	wasp-waist		15
DB7-12	0.2479	USD	110	15
DB3-3-9p	0.2827	wasp-waist		11
DB6-8	0.3292248	wasp-waist		-
DB5-6p	0.4042	wasp-waist		-

Table 4: Overview of the different grain sizes obtained from the Mr/Ms values measured in the hysteresis loops. The tables are sorted on locality and grain size. The TTE grain sizes are for pure pyrrhotite, while the EGI grain sizes are mixed with magnetite. By observation on the mineralogical content, a mix with magnetite is more probable.

Other ways of determining the grain size are hard. Small grain sizes show a slightly lower unblocking temperature spectrum; larger grain sizes show no changes in unblocking temperature (Dekkers 1989). Smaller grain sizes also show a larger decrease in intensity between 210-245°C in comparison to greater grain sizes, followed by an increase in intensity between 260-300°C, which is absent in greater grain sizes (Dekkers 1989). This is not observed in the NRM of these samples, so a small grain size is absent.

Comparing squareness versus coercivity plots with Tauxe (2002), which constructed squareness versus coercivity plots for pure magnetite, the pattern of the different modes of behavior show similarities in behavior with the Tamames section. This also seems to be the case for the Los Navalucillos rocks, but this is more complicated as the wasp-waisted part of the graph is in a different position. There is a clear boundary between multi domain and single domain samples and the super paramagnetic samples are positioned in the left part of the graph. The coercivity values differ though, probably because this is a different mineral.

4.3.4 IRM acquisition & End-member modelling

Two sets of IRM acquisition curves were measured on a robotic cryogenic magnetometer (Mullender et al. 2005) at Fort Hoofddijk, Utrecht University which were further processed to create sets of end-member curves. As explained in section 3.3.2, two distinct sets have been made. Only the second set will be treated in the main text as it is demagnetized in the regular way. The first set will be discussed in appendix A2.4.

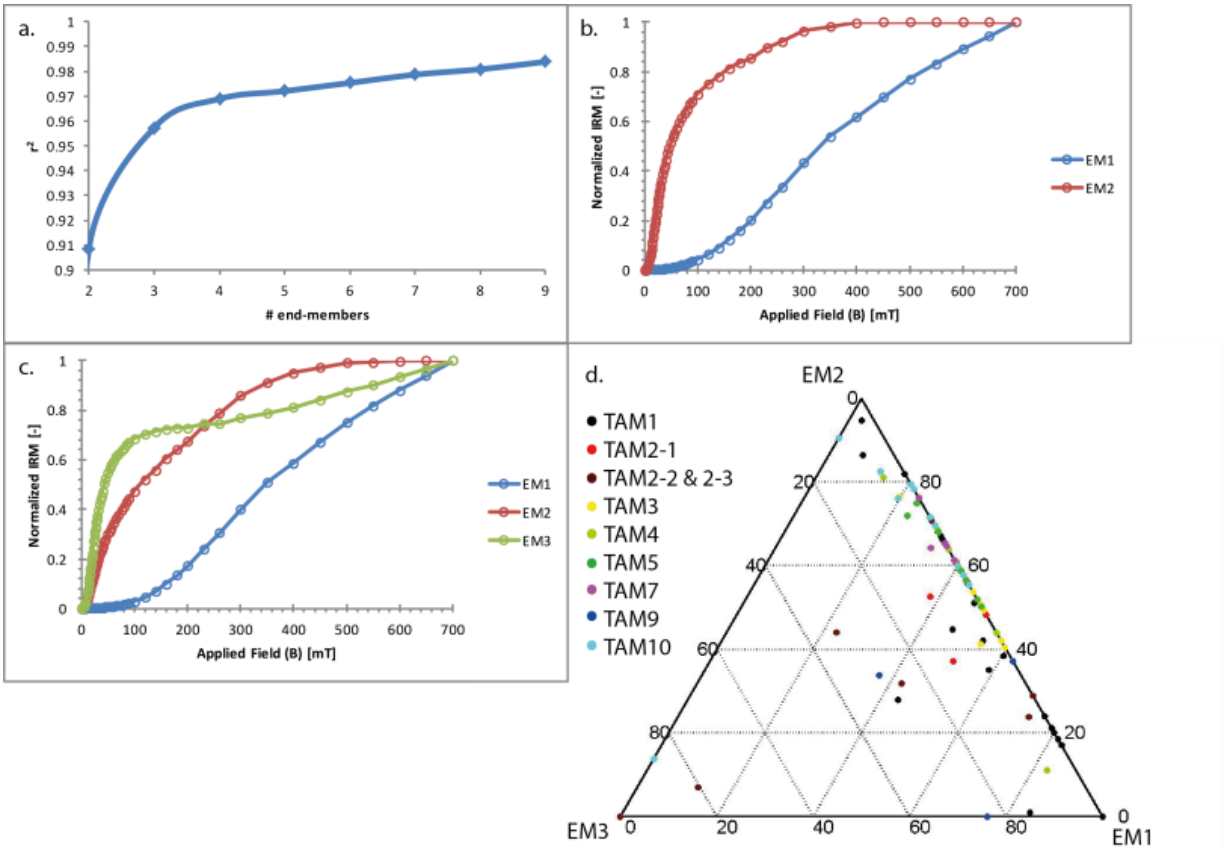

Figure 18a: Overview of the r^2 plot on the y-axis and the amount of end-members on the x-axis. The proper choice of amount of end members is at the bending point of the graph. b-c: the two and three end-member solution curve for IRM unmixing with applied field in T on the x-axis and normalized IRM acquisition on the y-axis. d: a triplot showing the distribution of the samples across the 3 end-member solution, sorted per site. All graphs only use data of the second IRM set.

The second set, IRM2, consists of 81 usable results out of the 96 samples and has been demagnetized with the longitudinal axis as final axis. Figure 19a shows the r^2 curve of this dataset per amount of end-members. Based on the criteria stated in the methods section 3.3.4, the two and three end-member model solutions are examined more closely and are shown in figure 18b and 18c.

The two end-member version shows one member which saturates around 400 mT and one continuously rising end-member which initially rises slowly and is not saturated at the limit of the test. The three end member shows an extra end-member at the top side of the graph which crosses the top end-member and changes both the paths. The EM2 is quite continuously rising and saturating around 500 mT, while EM3 stars with a giant start, but this slows down at 100 mT and starts to rise again around 300 mT. The ternary plot per site in figure 19d shows a low amount of samples which add greatly to the second end-member. These samples are originating from TAM2-2, TAM2-3, and TAM10.

Figure 19 shows the unmixed and idealized end-member IRM's. These are the results of the mathematical process and are therefore not real samples. EM1 shows a shallow start, but a big increment is located at the final part of the measurement. EM2 shows a continuous increase in acquisition which can be explained by two components and a third component to simulate the slow start. EM 3 shows two major increments at 20 mT and 200+ mT and is not saturated at the end of the simulated measurements.

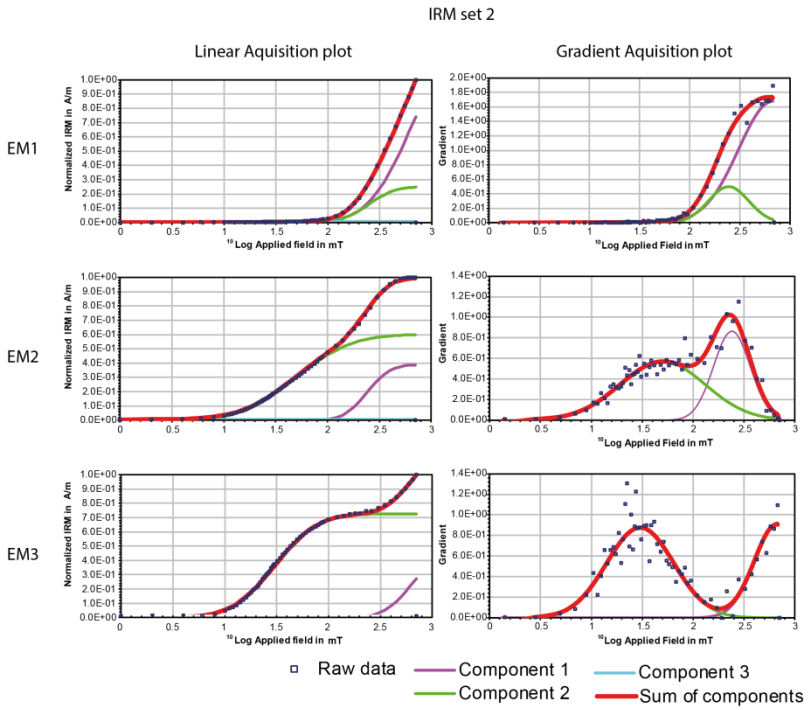

Figure 19: Unmixed end-members of IRM set 2 using multiple components. Applied field is on the x-axis (logarithmic scale) and IRM acquisition on the y-axis. The graphs represent the hypothetical 100% end-member which is not a sample per definition.

The three end-member set shows similarities to the IRM1 set, found in the Appendix. The style of the curves is similar, but the intersection of EM1 and 2 is at a lower applied field and a lower saturation value. There is an intersection in between EM2 and EM3, which is not always a proof of a viable solution. To find this out, the end-members must be coupled to properties. IRM set 1 shows a higher end-member related to magnetite.

Figure 20 shows an overview of habits of end members by using samples that are highly representative for one end-member curve. The samples have been compared on IRM acquisition, thermomagnetic and rock magnetic analysis, and NRM behavior.

EM2 is represented by a high amount of samples. It shows a high end IRM acquisition mainly from 100mT and up, combined with PSD and wasp-waisted hysteresis loops. The hysteresis loop shows PSD behavior and the NRM is not demagnetized completely at 350 °C.

The behavior of this end-member is mainly dominated by the samples that have a not fully demagnetized NRM at 350°C. This can be due to an influx of secondary minerals with a higher demagnetization temperature which explains the wasp-waistedness of the hysteresis loops. Combining this with the thermomagnetic results, the most logical influx would be one of magnetite as this has been found several times in low amounts.

EM1 is represented for 95% by a relatively high amount of samples and shows two steep increases in IRM around 25 mT and 250 mT as shown in the gradient acquisition plot. The thermomagnetic gradient shows a near equal value during heating and cooling. The hysteresis loop shows a very slight wasp waist profile and main demagnetization step between 270 and 295 °C.

EM3 shows a big increase in IRM acquisition in the middle part of the graph, around 40 to 70 mT, which is followed by a very tiny increase over the rest of the plot. The hysteresis loop is super paramagnetic to PSD and the NRM demagnetization shows a very straight line which almost touches the origin. This end-member is supported by a relatively low amount of samples, but is distinct in comparison to the others and therefore it deserves to be investigated more closely.

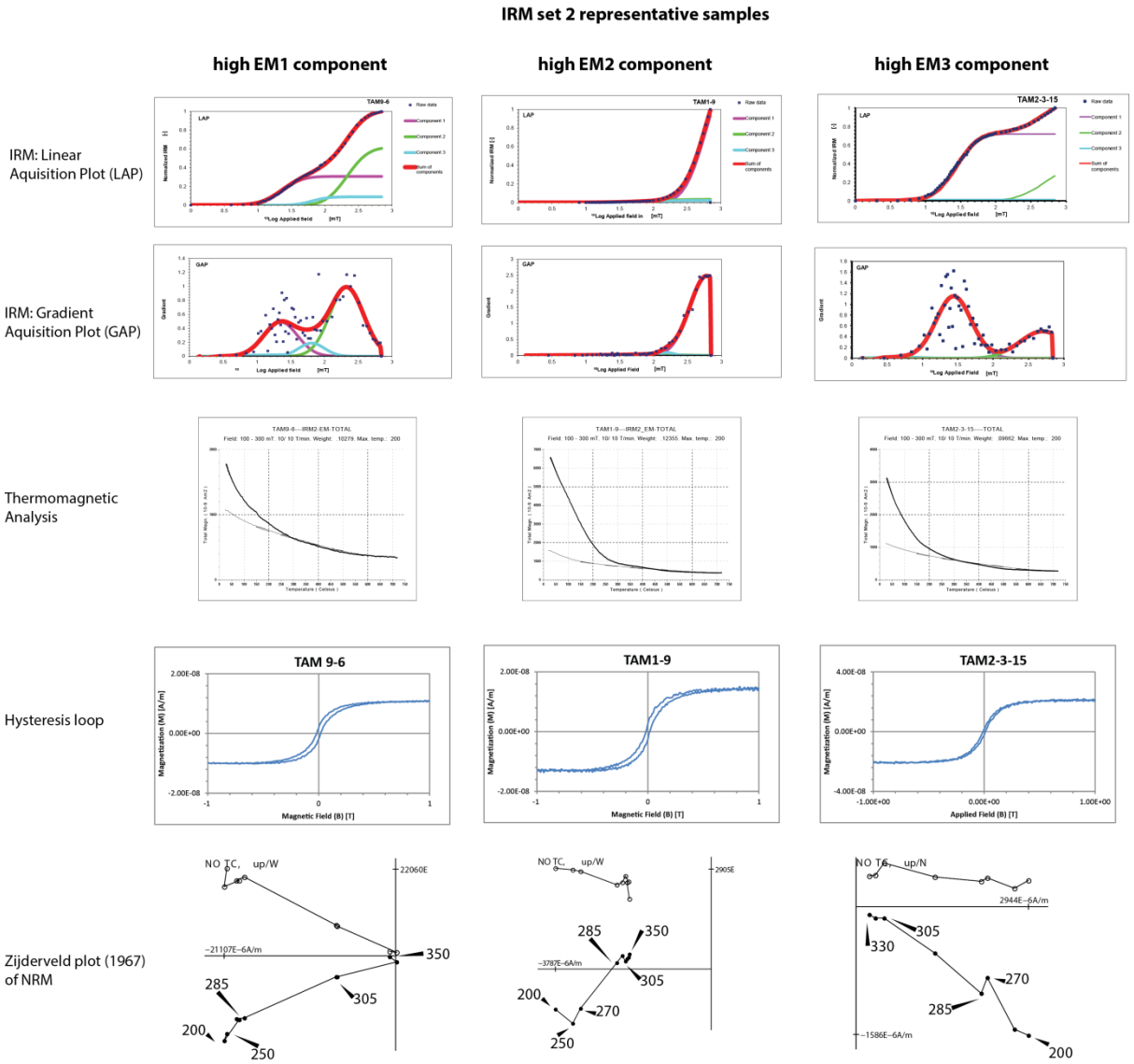

Figure 20: Overview of major representative samples per end-member of IRM set 2. The top two graphs show the unmixed IRM, followed by a thermomagnetic analysis, a hysteresis loop and the ChRM obtained by thermal demagnetization (temperature steps shown in °C). All the plots use the same axes as discussed before.

Different explanations for the habit of the EM1 and EM3 curves have been proposed. First proposed is grouping IRM curves per site, which did not show any trend. Also, IRM curves within one site do not show a general buildup. The non-stratigraphic sites (TAM4, 5, 7) show more consistently

grouped curves on comparison with the stratigraphic sites (TAM1, 2, 3, 9, 10), which can be explained by the fact that the stratigraphic sites are more spread. The IRM curves have been proposed to link to stratigraphical successions as some sites are on roughly the same stratigraphical height, but this did not give a direct relationship as well. Magnetic directions have been proposed as a correlation factor, but there is no correlation to be found here. The data is too spread out. IRM curves have been linked to chemical data to find a correlation, but linking end-member 1 to IRM curves also does not show an apparent correlation. The data is too spread out to show a correlation.

The first and third end members mainly show a consistent difference in hysteresis parameters. EM1 can be correlated with most of the USD-style samples in the hysteresis loops, showing a low relative high squareness. The samples that are more found towards EM3 are the three SPM/PSD style samples that have been measured. This is probably due to differences in pyrrhotite grain size and therefore the switching field distribution as there is no additional mineralogy found in these end-members. As EM3 has a different mineralogical content in comparison to EM2, the cross cutting of the two end-members in the graph is accepted, therefore accepting the three end-member solution.

5. Discussion

5.1 Paleomagnetic discussion

The main paleomagnetic components that are described in the results do not fit with each other without having some kind of deformation or alteration. The main indication is the elongated VGP scatter of the three similar localities (figure 9e to 9g). This indicates either deformation or inclination shallowing by sedimentary compaction (Tauxe et al. 2010).

As stated in section 4.3.1, pyrrhotite is found in the rocks which could be an indication of remagnetization. This is combined with the negative and inconclusive fold tests in all relevant localities which indicate mineral formation during or after deformation. This does not fit a large extensional phase, the Variscan orogenic phase, and oroclinal bending have been reported in between the Cambrian and Carboniferous to Early Permian as stated in the geological setting. After this Carboniferous to Early Permian deformation, Iberia has seen no internal rotations (Weil et al. 2010). The AMS measurements, as presented in section 4.2.2, indicate isotropic magnetic susceptibility, which suggest that they are not influenced by a big deformation event after formation of the magnetic mineralogy. Finally, no reversals have been observed in the NRM with an exception of 7 samples out of 360, which could have been caused by the human error of inverse marking.

The combination of all the observations and conclusions above shows that a remagnetization is a most probable which excludes inclination shallowing as sediments are not compacted anymore after lithification and remagnetization. To obtain this remagnetization effect, a major tectonic event must be present. We shift our view to the latest major deformation event in the history of the observed rocks, which is the oroclinal bending.

As stated in the geological setting, a remagnetization somewhere between 310 and 290 Ma has occurred during the latest major deformation seen in these Iberian rocks. This should be the tectonic event which fits the observations stated above and is therefore accepted for the study area. The widespread magmatic pulse as described by Gutiérrez-Alonso et al. (2011a) is prone candidate for remagnetization and occurs between 310 -297 Ma, narrowing the deformation and remagnetization time. As some major granites near the Tamames area have been dated at 308.7 Ma (Gutiérrez-Alonso et al. 2011b), one can assume that the remagnetization has been present as well in our study area. This would indicate that the remagnetized rocks are also (partially) incorporated in the

rotation, which explains the elongated VGP scatters. To fit this all in a coherent set of events, a vertical axis rotation must be present that is happening during rotation, which is linked to the oroclinal bending that is been highlighted by many authors in the area (eg Pastor-Galán et al. 2011; Weil et al. 2013; Pastor-Galan et al. 2015).

The orocline test, as described by Yonkee & Weil (2010), can be used to test whether this is an orocline or not. Normally, the orocline test consists of a plot in which the range of structural strikes is plotted on the x-axis versus magnetic declinations on the y-axis. A second plot is also used, plotting again structural strikes on the x-axis, but now shortening directions on the y-axis. If both plots show a slope of 1, the deformation is considered fully oroclinal. Using the data of Weil et al. (2013), which holds a huge collection of data on the Cantabrian Orocline, one can reverse the process to obtain the pre-folding declinations using the strike, the post-folding declinations, and the outcome of the orocline test under the assumption that the observed localities are a part of this oroclinal bend. Note that there is an opposite declination used when the strike is representative for the southern limb of the orocline.

The reversed orocline test shows a final magnetic declination of 90 for Tamames and 111 for the Los Navalucillos Limestone Formation as can be seen in figure 21 a&b. As the stable pole for Iberia is 209.1/43.9 ± 5.4; which is 154/-1 ± 5.4 in declination and inclination (Weil et al. 2010), which leads to the conclusion that there is a maximum rotation around 65 degrees for the Tamames limestone Formation. The Los Navalucillos limestone shows less rotation in the data set, but this data set consists of fewer measurements. Therefore, the rotation could be as large as the Tamames Limestone rotation, but it is not certain.

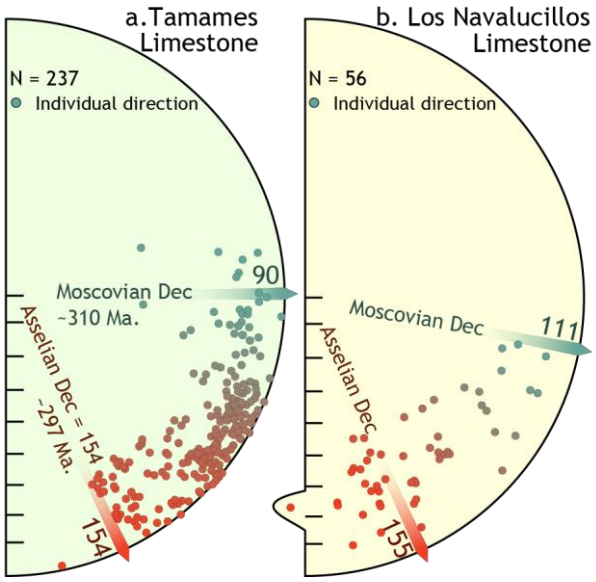

Figure 21: Equal area projections using the accepted magnetic directions. Reversing the outcome of the orocline test by using the known strikes and using a lot of paleomagnetic data across the Cantabrian Orocline shows us the reference declinations for the remagnetized Cambrian rocks of interest. The initial declination is rotated and therefore is located at 90 or 111 degrees of declination respectively.

The final problem is the elongated ellipse of magnetic directions which can be observed in every locality. This can be solved by interpreting this as multiple remagnetizations that have happened shortly after each other, which causes incomplete rotation of these points. This completes the interpretation of a remagnetization during rotation, which is going to be used in the paleolatitude calculation and further discussion.

Now that there is a timing on the magnetic structures, the geological timescale can be of importance (Gradstein et al. 2012). When checking in between 310 Ma and 297 Ma, there are minor normal periods in the Asselian and the Gzhelian, but mostly a reversed polarity is present around these times. This could however be a reason to accept the inversed cores, as stated in section 4.2.1 as valid.

5.2 Paleolatitude calculation

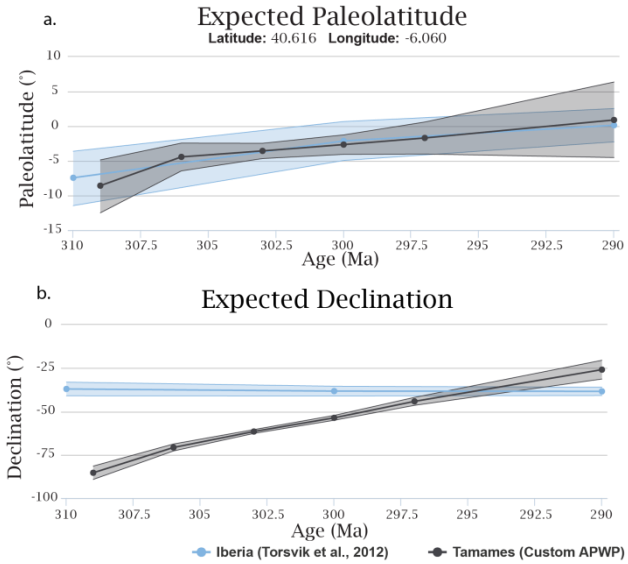

Figure 22: Expected paleolatitude and declination of the interpreted Tamames data in black, and the Torsvik et al. (2012) reference models in blue. The shades show the uncertainty boundary. The ages range from 310 Ma to 290 Ma. The final point is a literature point from Weil et al. (2010).

The results obtained from the apparent polar wander path can be used to test the above interpretation by comparing the paleolatitude and declination. The moving averages of section 4.2.3 are still used, in which an average of 25 points per 10 points is used, which has provided 5 data points.

There is no consensus on changes in rotational velocity, so constant rotation is assumed of 5 degrees per million years. Starting at 310 Ma and using the obtained total rotation of 65 degrees to come up with the total of 13 Ma, which is consistent with the interpretation of section 5.1.1. The 13 time s Figure 23: AMS plots of the different major localities in which κ1 (maximum magnetic susceptibility direction) is represented by blue squares, κ2 by green triangles, and κ3 (minimum magnetic susceptibility direction) by purple circles. Every top right graph shows anisotropy on the y-axis and mean bulk susceptibility on the x-axis. The bottom graph shows the rounding of the anisotropy ellipse versus anisotropy on the x-axis.

teps of 1 Ma each will again be averaged in 3 Ma timeframe steps. A sixth data point is obtained by adding the magnetic direction obtained by Weil et al. (2010). This literature point is accepted for 290 Ma which is latest Sakmarian as this is the latest possible window of orocline rotation. The result of this time-constrained moving average is shown in figure 22a, in which the reference model of Torsvik et al. (2012) is included in the calculator of Hinsbergen et al. 2015 and Koymans et al. (www.paleomagnetism.org, in press). The movement through the 0 fits with the observation of Weil et al. (2010), which states that Iberia crosses the equator between 315 and 290 Ma. The fit of the paleolatitude is very good, which shows that the time assumption is correct. The error in the data improves the Torsvik model in between 305 and 297 Ma. In total, a pure latitudinal movement of 766 km is obtained, which is comparable with the vertical distance between Amsterdam and Lyon. This results in an average plate velocity of 5.8 cm/year over the complete 13 Ma.

When comparing the measured declination to Torsvik et al. (2012) , declination is deviating from the reference model (figure 22b). This accepts the hypothesis for rotation during magnetization, as the paleolatitude is correct, but the declination is changing at a constant rate.

5.3 Remagnetization mechanisms

One of the main challenges of this thesis is to come up with an explanatory geological model that supports the mechanism behind the multiple remagnetization timings in a relatively short time as is used in the results section. This is complicated by the fact that the rock is metamorphosed slightly as well as dolomitized, which does complicate to observe original remagnetization characteristics of the rock.

As stated in section 4.3.4, no absolute correlations can be found between EM1, EM3 and other properties that have been measured in the Tamames limestone Formation, complicating the remagnetization origin. The remagnetization must be active for at least 65 degrees of rotation from 310 Ma to 297 Ma, whilst not demagnetizing the whole formation at once. The magnetic directions, and therefore the remagnetization pattern, show no distinct patterns over stratigraphy or position, which is interpreted as a local, patchy, and random remagnetization pattern.

This rules out various mechanisms for remagnetization, such as thermoviscous remanent magnetization (TVRM), which needs a long elevated temperature for periods of time (Kent 1985; Tauxe et al. 2010), indicating a prolonged and regional temperature regime for the reaction from magnetite to pyrrhotite (320°C). This is not possible because it leads to a regional simultaneous remagnetization which is clearly not the case. The rocks are slightly metamorphosed, but not as high grade as a 13+ Myr, 320°C burial, which makes pure TVRM very unlikely.

Pressure solution is another remagnetization method, as stated by for instance Evans & Elmore (2006), which investigate pressure solution in carbonates. It requires hot fluids and high pressures to form local dissolution patterns. This could be true locally, but cannot be observed properly as no SEM pictures are taken. Pressure solution could also be present due to compaction in the sediments, but this can be a false argument due to the presence of the metamorphism and the dolomitization, which can negate the pressure solutions.

This leads to the interpretation that alteration by multiple phases of hot fluids is the most probable source of remagnetization. As stated in the geological setting, widespread magmatism can be observed over the complete Cantabrian Orocline. This explanation can be supported by the fact that Gutiérrez-Alonso et al. 2011 found a granite near the Tamames locality with an age of 308.7 +/-1.4 Ma, which indicates that there is magmatism during the early deformation providing an opportunity for hot fluids to appear already during early deformation stages. Most of the sampled cores show multiple pores that can be seen with the naked eye, which could indicate fluid flow, but could also be coupled to the dolomitization of the limestones somewhere in time. Also, several rocks show cracks which can be used for this fluid flow, although these also can be coupled to the dolomitization.

This solution is categorized as a Chemical Remanent Magnetization (CRM) process and is widely accepted in other Paleozoic limestones that have been associated with a remagnetization during the formation of Pangea (eg. Jackson 1990; Garza & Zijderveld 1996; Van der Voo et al. 1997; Weil & Van der Voo 2002).

As stated before, Pyrrhotite has a curie temperature of 320 °C, which could be reached when purely investigating the metamorphic degree. Aubourg et al. (2012) propose a burial model designed for claystones in which temperature is the main variable for a CRM. This is combined with field experiments on marly carbonates of Rochette (1987) who found two isograds in the Alps: the breakdown of magnetite at 250°C and the breakdown of pyrite to pyrrhotite at 320°C. Pyrrhotite completely replaces magnetite at 300°C, also removing the magnetization of the magnetite (Rochette 1987; Aubourg et al. 2012). Pyrite is also used in this reaction in order to provide the necessary sulfur (Crouzet et al. 2001; Schill et al. 2002; Aubourg et al. 2012).

This principle can be applied to the samples that are covered in this report, which mainly can give an answer to several end-members. EM2 is not fully demagnetized at 350°C due to magnetite. This could give a temperature indication for these samples between 250°C and 300°C. EM1 and EM3 are close to being fully demagnetized, so would most probably be above the 300°C mark, in which EM1 shows a bigger grain size in comparison to EM3. This difference can be interpreted as the duration of

the heating period as longer periods of heating tend to create larger grains. DB2-11, which is not completely demagnetized, shows a clear presence of pyrite in the sample, which shows that pyrite could be present in the rock to accommodate this process. As pyrite is denoted as a weak paramagnet, no large disturbances will be found throughout the measurements.

The local CRM interpretation is illustrated in figure 23a to 23c, in which the Tamames area is highlighted in the proposed deformation timespan of 310 to 297 Ma. The well visible outcrops are shown in brown, running throughout the area. The figures are rotated to highlight the fact that the surroundings rotate instead of a very quick change in magnetic direction. Hot fluids locally alter the minerals from magnetite to pyrrhotite and remagnetizes to the local field which is then rotated to position somewhere between a declination of 90 and 155. The later the remagnetization, the less rotation incorporated in the declination. There is constraint on the amount of remagnetizations have occurred during this time and one site can have had multiple remagnetizations during that time. No measurements are performed on the Quartzite, therefore no information is shown. The parts that did not complete the full transition to pyrrhotite still show pyrrhotite dominance, but are not fully recrystallized.

Note that there is a big an assumption of complete remagnetization at the start of the oroclinal deformation in figure 23a. It is hard to truly check for the complete remagnetization in this area due to the remagnetizations that have been occurring over the timespan of the rotation. This can be validated by using the remagnetization timeframe as discussed in the geological setting as there is a remagnetization that has occurred during the Westphalian (Weil et al. 2010 and many others). No primary remagnetization has been observed, making at least one full remagnetization likely.

5.4 Orocline discussion

One of the key questions in this report was to define whether there are one or two orocline systems. This could be solved by looking at the similarities between the localities. Magnetic directional wise, TAM and the two DB localities are alike, which is a good indication that all are part of the same oroclinal system as discussed in section 5.1. All the measured localities have been showing counterclockwise rotation, while the Central Iberian Orocline explicitly needs a clockwise rotation in order to fit the second orocline.

So, is there a second orocline or not? Although this is one of the main objectives, there is no true consensus found in this report as all the localities show magnetic directions belonging to the Cantabrian Orocline. This does not disprove the Central Iberian Orocline, but it is less likely to show that the CIO is a complete orocline.

If the Central Iberian Orocline has existed, the rotation must have ended before the Moscovian which is, according to the literature, the initiation of the rotation of the Cantabrian Orocline. This could be a viable solution, but conflicts with the data that Aerden (2004), Martínez Catalán (2011), and Shaw et al. (2012) presented, whom have stated that simultaneous oroclinal bending is possible. The solution to this can be situated in the way that the data of the above papers has been collected. Porphyroblasts only show the relative age of deformations, which therefore allows pre-Moscovian bending. The final deformation phase of Aerden (2004), FS4, is reported to be post 310 Ma, which could be oroclinal bending of the Cantabrian Orocline, as the most southern sample is taken around the same locality as the Tamames area. The paleocurrent directions of Shaw et al. (2012) originate from the Lower Ordovician which implies that bending could have happened earlier in time than the Late Carboniferous/Early Permian oroclinal phase and the coeval forming of these two oroclines is explicitly stated as an assumption. One conclusion could be that the Central Iberian Orocline is a pre-

formed structure which does imply that there is no secondary bending. This primary bend could be formed by several large tectonic events, but no evidence has been found up to date.

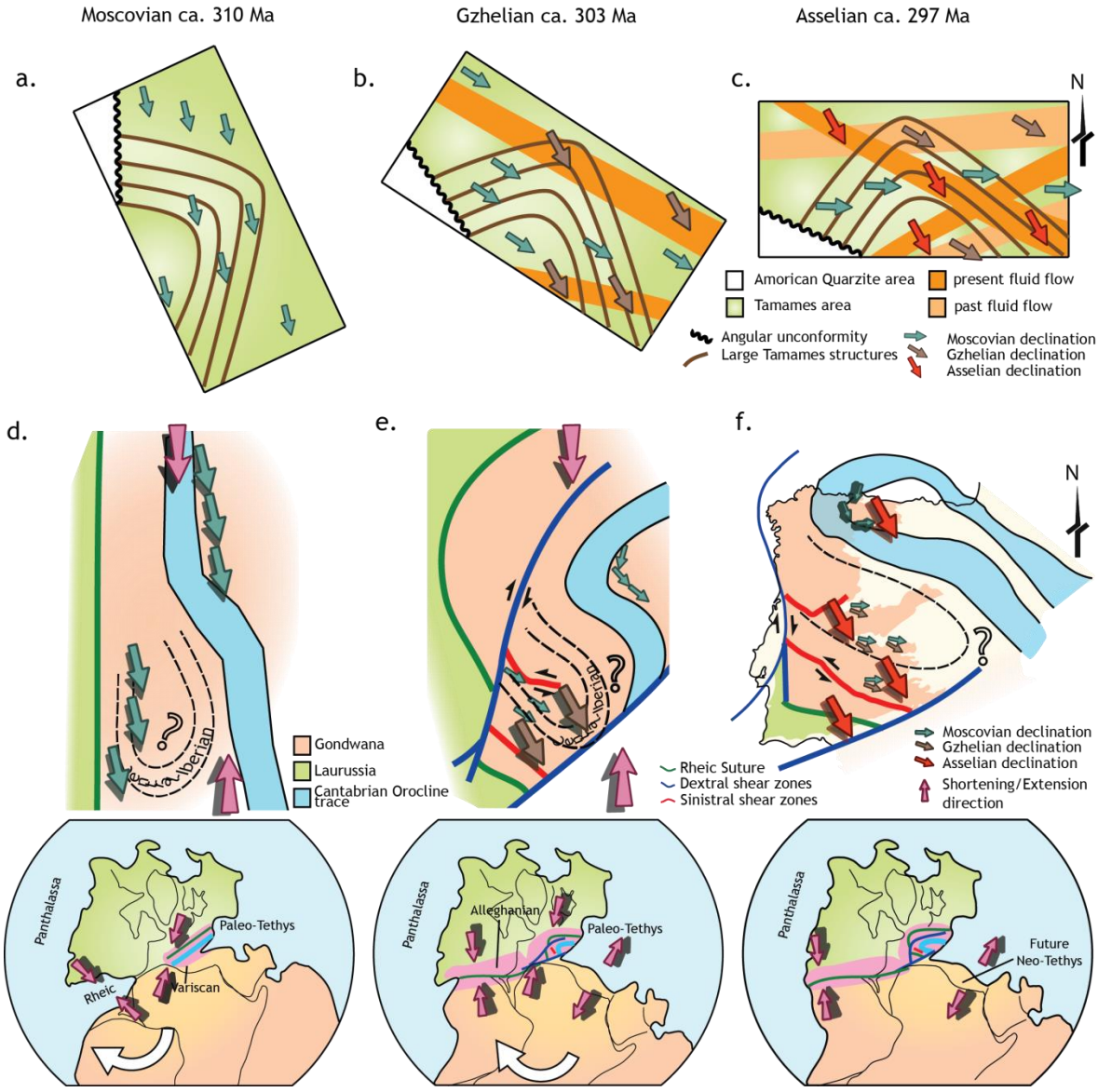

Figure 24a-c: Conceptual model of the rotation and remagnetization of the Tamames area through time using hot fluid flows as reason for remagnetization. The Tamames area is rotated during this time which is represented with the rotated figures. d-f: Conceptual model that uses the impact of this study combined with all the literature data that shows the amalgamation of Pangea following the same time steps as above. The formation of the orocline is caused by a stress change which can be related to the movement of Laurentia and Gondwana.

A proposed solution according to the data of this thesis can be seen in figure 23d to 23f, which uses the same timeframe as figure 23 a to c. At 310 Ma, the orogeny starts out roughly linear with some room for little alterations. Gondwana and Laurussia are already connected, but do not exert the pressure to bend Iberia at that time. In figure 23e, a counterclockwise rotation appears which is also visible in the Tamames area, forced by the compression of the two surrounding continents Laurussia and Gondwana. The colored arrows in figure 23e show the rotated directions. The north/south compression continues to push, therefore pushing the Cantabrian Orocline all the way to a 180 degree position (Figure 23f). The red arrows are representative for the Asselian declination, which is pointing southwest. The older declinations are now spread out from a declination of 90 to the Asselian declination which is similar to the observations done in this thesis. The Central Iberian

Orocline is shown in the figures, but optional and as already existing structure as no supportive evidence is found for simultaneous bending.

5.5 Suggestions for further research

Although this research proposes a valid solution, more work can be done to expand this research to capture this in data. Personal suggestions to this would be to do more rock magnetic analysis in order to properly capture the boundaries of the pyrrhotite/magnetite bearing samples, enabling more robust interpretations on the nature and habit of the magnetic directions and end-members. Also, the usage of a SEM (Scanning Electron Microscope) could be of importance to visualize the interplay between magnetite & pyrrhotite and make observations on grain sizes. A parallel can be drawn to the chemical side of this remagnetization, as multiple aspects are important, such as the burial depth, pH levels and redox conditions. These have not been studied well enough to show definitive conclusions. It could be interesting to see whether these settings can confirm the statements that have been made.

6. Conclusions

Paleomagnetic results from three Cambrian localities show scattering magnetic directions between a declination of 90 and 155 combined with a low inclination. As shown by a synthesis stratigraphic column and stratigraphical cored measurements, there is no trend in the magnetic data. The magnetic directions are combined with an elongated VGP scatter, magnetically isotropic rock conditions and the presence of pyrrhotite to the interpretation that the rocks are remagnetized and rotated 65 degrees counterclockwise. The oroclinal bending of the Variscan is a prone candidate for remagnetization and rotation and is supported by the fit of the paleolatitudes of one locality obtained to the models of Torsvik et al. (2012).

Thermal demagnetization profiles and thermomagnetic analysis show pyrrhotite as main carrier with small additions of magnetite. IRM acquisition measurements of one locality result in a three end-member solution that discriminates two grain sizes of pyrrhotite and one end-member for magnetite presence. The hysteresis parameters mainly show single domain with some multi domain specimen at all three localities, suggesting similar habits and deformation mechanisms.

The proposed explanatory model for the Tamames locality shows multiple stages of local remagnetizations during rotation of the localities for the total duration of 13 Myrs, which explains the elongated VGP scatters and the scatter in magnetic directions. The rotation is caused by the oroclinal bending between 310 and 297 Ma. The remagnetization is due to burial and local hot fluid flow and is present at the same time as the oroclinal bending. The other two localities show similar magnetic directions, mineralogy and hysteresis parameters, which implies similar scenarios.

The model does not meet with the proposed statement of literature that orocline formation of the Cantabrian Orocline and the Central Iberian Orocline is simultaneous, as the only paleomagnetic footprints of the northern Cantabrian Orocline are found during at these locations. This does not disprove the Central Iberian Orocline in the south, as it could have been formed before 310 Ma, which might fit with gaps in the literature data. It could also be a primary bend.

7. References

Aerden, D.G. a M., 2004. Correlating deformation in Variscan NW-Iberia using porphyroblasts; implications for the Ibero-Armorican Arc. *Journal of Structural Geology*, 26(1), pp.177–196.

Appel, E., Crouzet, C. & Schill, E., 2012. Pyrrhotite remagnetizations in the Himalaya: a review. *Geological Society, London, Special Publications*, 371(1), pp.163–180.

Aubourg, C., Pozzi, J.-P. & Kars, M., 2012. Burial, claystones remagnetization and some consequences for magnetostratigraphy. *Geological Society, London, Special Publications*, 371(1), pp.181–188.

Bonjour, J.L. et al., 1988. U-Pb zircon dating of the early paleozoic (Arenigian) transgression in Western Brittany (France): A new constraint for the lower paleozoic time-scale. *Chemical Geology: Isotope Geoscience section*, 72(4), pp.329–336.

Borradaile, G.J., 1988. Magnetic susceptibility, petrofabrics and strain. *Tectonophysics*, 156(1-2), pp.1–20.

Borradaile, G.J. & Henry, B., 1997. Tectonic applications of magnetic susceptibility and its anisotropy. *Earth-Science Reviews*, 42(1-2), pp.49–93.

Borradaile, G.J. & Jackson, M., 2004. Anisotropy of magnetic susceptibility (AMS): magnetic petrofabrics of deformed rocks. *Geological Society, London, Special Publications*, 238(1), pp.299–360.

Carbonell, R. et al., 2004. Geophysical evidence of a mantle derived intrusion in SW Iberia. *Geophysical Research Letters*, 31(11), pp.2–5.

Carey, S.W., 1955. The orocline concept in geotectonics-Part I. *Papers and proceedings of the Royal Society of Tasmania*, 89, pp.255–288.

Carpenter, R.H., 1974. Pyrrhotite Isograd in Southeastern Tennessee and Southwestern North Carolina. *Geological Society of America Bulletin*, 85(3), p.451.

Cocks, L.R.M. & Torsvik, T.H., 2002. Earth geography from 500 to 400 million years ago : a faunal and palaeomagnetic review. *Journal of the Geological Society: London*, 159(6), pp.631–644.

Corrales, I., Manjón, M. & Valladares, I., 1974. La Serie Carbonatada de Navarredonda De La Rinconada (Salamanca, España). *Stvdia Geologica*, 8, pp.85–91.

Corrales, I. & Valladares, I., 1980. Facies Carbonatadas del Cambrico de Salamanca. *Stvdia Geologica Salmanticensia*, 16, pp.95–102.

Crouzet, C. et al., 2001. Detailed analysis of successive pTRMs carried by pyrrhotite in Himalayan metacarbonates: an example from Hidden Valley, Central Nepal. *Geophysical Journal International*, 146(3), pp.607–618.

Dallmeyer, R.D. et al., 1997. Diachronous Variscan tectonothermal activity in the NW Iberian Massif: Evidence from 40Ar/39Ar dating of regional fabrics. *Tectonophysics*, 277(4), pp.307–337.

Dankers, P.H.M. & Zijderveld, J.D. a., 1981. Alternating field demagnetization of rocks, and the problem of gyromagnetic remanence. *Earth and Planetary Science Letters*, 53(1), pp.89–92.

Deenen, M.H.L. et al., 2011. Geomagnetic secular variation and the statistics of palaeomagnetic directions. *Geophysical Journal International*, 186(2), pp.509–520.

Dekkers, M.J., 2012. End-member modelling as an aid to diagnose remagnetization: a brief review. *Geological Society, London, Special Publications*, 371(1), pp.253–269.

Dekkers, M.J., 1988. Magnetic properties of natural pyrrhotite Part I: Behaviour of initial

susceptibility and saturation-magnetization-related rock-magnetic parameters in a grain-size dependent framework. *Physics of the Earth and Planetary Interiors*, 52(3-4), pp.376–393.

Dekkers, M.J., 1989. Magnetic properties of natural pyrrhotite. II. High- and low-temperature behaviour of Jrs and TRM as function of grain size. *Physics of the Earth and Planetary Interiors*, 57, pp.266–283.

Dias, G. et al., 1998. U-Pb zircon and monazite geochronology of post-collisional Hercynian granitoids from the Central Iberian Zone (Northern Portugal). *Lithos*, 45(1-4), pp.349–369.

Díez Balda, M.A., 1986. *El Complejo esquisto-grauváquico, las series paleozóicas y la estructura hercínica al sur de Salamanca*,

Díez Fernández, R. et al., 2013. Rheological control on the tectonic evolution of a continental suture zone: The Variscan example from NW Iberia (Spain). *International Journal of Earth Sciences*, 102(5), pp.1305–1319.

Díez Fernández, R. et al., 2011. Tectonic evolution of a continental subduction-exhumation channel: Variscan structure of the basal allochthonous units in NW Spain. *Tectonics*, 30(3), p.n/a–n/a (22p).

Díez Fernández, R. et al., 2012. The onset of the assembly of Pangaea in NW Iberia: Constraints on the kinematics of continental subduction. *Gondwana Research*, 22(1), pp.20–25.

Diez-Balda, M.A., Martinez-Catalan, J.R. & Ayarza-Arribas, P., 1995. Syn-collisional extensional collapse parallel to the orogenic trend in a domain of steep tectonics: the Salamanca Detachment Zone (Central Iberian Zone, Spain). *Journal of Structural Geology*, 17(2), pp.163–182.

Egli, R., 2004. Characterization of Individual Rock Magnetic Components by Analysis of Remanence Curves, 1. Unmixing Natural Sediments. *Studia geophysica et geodaetica*, 48(1), pp.391–446.

Evans, M.A. & Elmore, R.D., 2006. Fluid control of localized mineral domains in limestone pressure solution structures. *Journal of Structural Geology*, 28(2), pp.284–301.

Fernández Suarez, J. et al., 2000. Variscan collisional magmatism and deformation in NW Iberia: constraints from U-Pb geochronology of granitoids. *Journal of the Geological Society*, 157(3), pp.565–576.

Ferry, J.M., 1981. Petrology of graphitic sulfide-rich schists from south-central Maine: an example of desulfidation during prograde regional metamorphism. *American Mineralogist*, 66(7-8), pp.908–931.

Garza, R.S.M. & Zijderveld, J.D. a., 1996. Paleomagnetism of Paleozoic strata, Brabant and Ardennes Massifs, Belgium: Implications of prefolding and postfolding Late Carboniferous secondary magnetizations for European apparent polar wander. *Journal of Geophysical Research*, 101(B7), p.15799.

Gradstein, F.M., Ogg, J.G. & Hilgen, F.J., 2012. On The Geologic Time Scale. *Newsletters on Stratigraphy*, 45(2), pp.171–188.

Groenewegen, T., 2014. *The intriguing geometry of the Central Iberian Orocline*.

Gutiérrez-Alonso, G. et al., 2012. Buckling an orogen : The Cantabrian Orocline. *GSA Today*, (7), pp.4–9.

Gutiérrez-Alonso, G., Fernández-Suárez, J., et al., 2011. Diachronous post-orogenic magmatism within a developing orocline in Iberia, European Variscides. *Tectonics*, 30(5), p.n/a–n/a.

Gutiérrez-Alonso, G., Murphy, J.B., et al., 2011. Lithospheric delamination in the core of Pangea: Sm-

Nd insights from the Iberian mantle. *Geology*, 39(2), pp.155–158.

Gutiérrez-alonso, G. & Fernández-suárez, J., 2004. Orocline triggered lithospheric delamination. *Geological Society of America Special Paper*, 383(2), pp.121–130.

Hall, a. J., 1986. Pyrite-Pyrrhotine Redox Reactions in Nature. *Mineralogical Magazine*, 50(356), pp.223–229.

Heslop, D. & Dillon, M., 2007. Unmixing magnetic remanence curves without a priori knowledge. *Geophysical Journal International*, 170(2), pp.556–566.

Heslop, D., McIntosh, G. & Dekkers, M.J., 2004. Using time- and temperature-dependent Preisach models to investigate the limitations of modelling isothermal remanent magnetization acquisition curves with cumulative log Gaussian functions. *Geophysical Journal International*, 157(1), pp.55–63.

Hinsbergen, D.J.J. Van et al., 2015. A Paleolatitude Calculator for Paleoclimate Studies. *Plos One*, 10(6), pp.1–21.

Hirt, a. M. et al., 2004. Magnetic and mineral fabric development in the Ordovician Martinsburg Formation in the Central Appalachian Fold and Thrust Belt, Pennsylvania. *Geological Society, London, Special Publications*, 238(1), pp.109–126.

Hrouda, F., 1986. The effect of Quartz on the magnetic anisotropy of quarzite. *Studia geophysica et geodaetica*, 30(1), pp.39–45.

Hrouda, F. & Jelinek, V., 1990. Resolution of ferrimagnetic and paramagnetic anisotropies in rocks, using combined low-field and high-field measurements. *Geophysical Journal International*, 103(1), pp.75–84.

Jackson, M.J., 1990. Diagenetic sources of stable remanence in remagnetized Paleozoic cratonic carbonates: a rock magnetic study. *Journal of Geophysical Research B: Solid Earth*, 95(B3), pp.2753–2761.

Jelinek, V., 1978. Statistical processing of anisotropy of magnetic susceptibility measured on groups of specimens. *Studia geophysica et geodaetica*, 22, pp.50–62.

Julivert, M. et al., 1972. Mapa Tectônico de la Peninsula Ibérica y Baleares a escala 1:1000000. , p.IGME Madrid.

Kent, D., 1985. Thermoviscous remagnetization in some Appalachian limestones. *Geophysical Research Letters*, 12(12), pp.3–6.

Kirschvink, J.L., 1980. The least-squares line and plane and the analysis of paleomagnetic data. *Geophysical Journal of the Royal Astronomical Society*, 62(3), pp.699–718.

Kollmeier, J.M., Van Der Pluijm, B. a. & Van Der Voo, R., 2000. Analysis of Variscan dynamics; early bending of the Cantabria-Asturias Arc, northern Spain. *Earth and Planetary Science Letters*, 181(1-2), pp.203–216.

Koymans, M.R. et al., Paleomagnetism.org - An Online multi-platform and open source environment for Paleomagnetic Analysis. *Computers & Geoscience*.

Kruiver, P.P., Dekkers, M.J. & Heslop, D., 2001. Quantification of magnetic coercivity components by the analysis of acquisition curves of isothermal remanent magnetisation. *Earth and Planetary Science Letters*, 189(3-4), pp.269–276.

Lambert, B., 1973. Post availability of suphur and metals and formation of secondary textures and structures in stratiform sed- imentary sulfide deposits. *J. Geol. Sot. Australia*, 20(October 2015), pp.205–215.

Linnemann, U. et al., 2008. The Cadomian Orogeny and the opening of the Rheic Ocean: The diacrony of geotectonic processes constrained by LA-ICP-MS U-Pb zircon dating (Ossa-Morena and Saxo-Thuringian Zones, Iberian and Bohemian Massifs). *Tectonophysics*, 461(1-4), pp.21–43.

Martínez Catalán, J.R. et al., 2009. A rootless suture and the loss of the roots of a mountain chain: The Variscan belt of NW Iberia. *Comptes Rendus Geoscience*, 341(2-3), pp.114–126.

Martínez Catalán, J.R., 2011. Are the oroclines of the Variscan belt related to late Variscan strike-slip tectonics? *Terra Nova*, 23(4), pp.241–247.

Martínez Catalán, J.R. et al., 2007. Space and time in the tectonic evolution of the northwestern Iberian Massif : Implications for the Variscan belt. *Geological Society of America*, Memoir 200(21), pp.403–423.

Matte, P., 2001. The Variscan collage and orogeny (480 ± 290 Ma) and the tectonic definition of the Armorica microplate : a review. *Terra Nova*, 13(2), pp.122–128.

Mattei, M. et al., 1997. Magnetic fabric of weakly deformed clay-rich sediments in the Italian peninsula: Relationship with compressional and extensional tectonics. *Tectonophysics*, 271(1-2), pp.107–122.

Menéndez Carrasco, S., 2013. *Los arequeociatos de la formación Calizas de Los Navalucillos en los Montes de Toledo*.

Montero, P. et al., 2007. Zircon ages of the metavolcanic rocks and metagranites of the Ollo de Sapo Domain in central Spain: implications for the Neoproterozoic to Early Palaeozoic evolution of Iberia. *Geological Magazine*, 144(06), pp.963–976.

Mullender, T. a. T., van Velzen, a. J. & Dekkers, M.J., 1993. Continuous drift correction and separate identification of ferrimagnetic and paramagnetic contributions in thermomagnetic runs. *Geophysical Journal International*, 114, pp.663–672.

Mullender, T.A.T. et al., 2005. Fully automated demagnetization and measurement of NRM, ARM and IRM on a '2G' SQUID magnetometer,. In *IAGA, abstract number: IAGA2005-A-00898.*

Parés, J.M., Van der Pluijm, B. a. & Dinarès-Turell, J., 1999. Evolution of magnetic fabrics during incipient deformation of mudrocks (Pyrenees, northern Spain). *Tectonophysics*, 307(1-2), pp.1–14.

Parés, J.M. & Van der Voo, R., 1992. Paleozoic paleomagnetism of Almaden, Spain: A cautionary note. *Journal of Geophysical Research*, 97(B6), p.9353.

Pastor-Galan, D. et al., 2015. One or two oroclines in the Variscan orogen of Iberia? Implications for Pangea amalgamation. *Geology*, (6), pp.527–530.

Pastor-Galán, D. et al., 2012. Conical folding in the core of an orocline. A geometric analysis from the Cantabrian Arc (Variscan Belt of NW Iberia). *Journal of Structural Geology*, 39, pp.210–223.

Pastor-Galán, D., Gutiérrez-Alonso, G. & Weil, A.B., 2011. Orocline timing through joint analysis: Insights from the Ibero-Armorican Arc. *Tectonophysics*, 507(1-4), pp.31–46.

Perroud, H., Calza, F. & Khattach, D., 1991. Paleomagnetism of the Silurian volcanism at Almaden, southern Spain. *Journal of Geophysical Research*, 96(B2), p.1949.

Potter, D.K. & Stephenson, a, 2005. New observations and theory of single-domain magnetic moments. *Journal of Physics: Conference Series*, 17, pp.168–173.

Robertson, D.J. & France, D.E., 1994. Discrimination of remanence-carrying minerals in mixtures, using isothermal remanent magnetisation acquisition curves. *Physics of the Earth and Planetary*

Interiors, 82(3-4), pp.223–234.

Rochette, P., 1987. Metamorphic control of the magnetic mineralogy of black shales in the Swiss Alps: toward the use of "magnetic isograde." *Earth and Planetary Science Letters*, 84(4), pp.446–456.

Rodriguez-Alonso, M.D. et al., 2004. La secuencia litoestratigráfica del Neoproterozoico-Cámbrico Inferior del Dominio del Complejo Esquito-Gravuáquico. *Geologia de España*, pp.78–81.

Sagnotti, L. et al., 1998. Magnetic fabric of clay sediments from the external northern Apennines (Italy). *Physics of the Earth and Planetary Interiors*, 105(1-2), pp.73–93.

Schill, E., Appel, E. & Gautam, P., 2002. Towards pyrrhotite/magnetite geothermometry in low-grade metamorphic carbonates of the Tethyan Himalayas (Shiar Khola, Central Nepal). *Journal of Asian Earth Sciences*, 20, pp.195–201.

Schwarz, S. & Van der Voo, R., 1983. Paleomagnetic Evalutation of the orocline hypothesis in the Central and Southern Appalachian. *Geophysical Reserch Letters*, 10(7), pp.505–508.

Shaw, J. et al., 2012. Oroclines of the Variscan orogen of Iberia: Paleocurrent analysis and paleogeographic implications. *Earth and Planetary Science Letters*, 329-330, pp.60–70.

Stampfli, G.M. & Borel, G.D., 2002. A plate tectonic model for the Paleozoic and Mesozoic constrained by dynamic plate boundaries and restored syntetic ocean isochrons. *Earth and Planetary Science Letters*, 196(1-2), pp.17–33.

Stephenson, a., 1993. Three-axis static alternating field demagnetization of rocks and the identification of natural remanent magnetization, gyroremanent magnetization, and anisotropy. *Journal of Geophysical Research*, 98(B1), p.373.

Tauxe, L. et al., 2010. Essentials of Paleomagnetism. *University of California press*, p.512.

Tauxe, L., 2002. Physical interpretation of hysteresis loops: Micromagnetic modeling of fine particle magnetite. *Geochemistry Geophysics Geosystems*, 3(10).

Tauxe, L. & Watson, G.S., 1994. The fold test: an eigen analysis approach. *Earth and Planetary Science Letters*, 122(3-4), pp.331–341.

Torsvik, T.H. et al., 2012. Phanerozoic polar wander, palaeogeography and dynamics. *Earth-Science Reviews*, 114(3-4), pp.325–368.

Tracy, R.J. & Robinson, P., 1988. Silicate-sulfide-oxide-fluid reactions in granulite-grade pelitic rocks, central Massachusetts. *American Mineralogist*, 288-A, pp.45–74.

Ugidos, J.M. et al., 2003. Geochemistry of the Upper Neoproterozoic and Lower Cambrian siliciclastic rocks and U-Pb dating on detrital zircons in the Central Iberian Zone, Spain. *International Journal of Earth Sciences*, 92(5), pp.661–676.

Valladares, M.I. et al., 2000. Upper Neoproterozoic: Lower Cambrian sedimentary successions in the Central Iberian Zone (Spain): sequence stratigraphy , petrology and chemostratigraphy . Implications for other European zones. *Int J Earth Sci*, 8, pp.2–20.

Van der Voo, R., Stamakatos, J. & Parés, J., 1997. Kinematic constraints on thrust-belt curvature from syndeformational magnetizations in the Lagos del Valle Syncline in the Cantabrian Arc, Spain. *Journal of Geophysical Research*, 102(B5), pp.105–119.

Weil, a., Gutierrez-alonso, G. & Conan, J., 2010. New time constraints on lithospheric-scale oroclinal bending of the Ibero-Armorican Arc: a palaeomagnetic study of earliest Permian rocks from Iberia. *Journal of the Geological Society*, 167(1), pp.127–143.

Weil, A.B. et al., 2013. Kinematic constraints on buckling a lithospheric-scale orocline along the northern margin of Gondwana: A geologic synthesis. *Tectonophysics*, 582, pp.25–49.

Weil, A.B., 2006. Kinematics of orocline tightening in the core of an arc: Paleomagnetic analysis of the Ponga Unit, Cantabrian Arc, northern Spain. *Tectonics*, 25(3), pp.1–23.

Weil, A.B. et al., 2000. The formation of an orocline by multiphase deformation: A paleomagnetic investigation of the Cantabria-Asturias Arc (northern Spain). *Journal of Structural Geology*, 22(6), pp.735–756.

Weil, A.B. & Sussman, A.J., 2004. Classifying curved orogens based on timing relationships between structural development and vertical-axis rotations. *Geological Society of America Special Papers*, 383, pp.1–15.

Weil, A.B. & Van der Voo, R., 2002. Insights into the mechanism for orogen-related carbonate remagnetization from growth of authigenic Fe-oxide: A scanning electron microscopy and rock magnetic study of Devonian carbonates from northern Spain. *Journal of Geophysical Research-Solid Earth*, 107(B4), p.14.

Weil, A.B., Van der Voo, R. & van der Pluijm, B. a., 2001. Oroclinical bending and evidence against the Pangea megashear: The Cantabria-Asturias arc (northern Spain). *Geology*, 29(11), pp.991–994.

Weltje, G.J., 1997. End-member modeling of compositional data: Numerical-statistical algorithms for solving the explicit mixing problem. *Mathematical Geology*, 29(4), pp.503–549.

Winchester, J.A., Pharoh, T.C. & Verniers, J., 2002. Palaeozoic amalgamation of Central Europe : an introduction and synthesis of new results from recent geological and geophysical investigations. *Geological Society, London, Special Publications*, 201, pp.1–18.

Yonkee, A. & Weil, A.B., 2010. Quantifying vertical axis rotation in curved orogens: Correlating multiple data sets with a refined weighted least squares strike test. *Tectonics*, 29(3), pp.1–31.

Zijderveld, J.D. a., 1967. AC demagnetization of rocks: analysis of results. In *methods of paleomagnetism*. pp. 254–286.

A. Appendices

A1. Methods

A1.1 Anisotropy of magnetic susceptibility

Anisotropy of Magnetic Susceptibility is a symmetric tensor relating to the applied magnetic field H_i to the magnetization M_i through the second order magnetic susceptibility tensor χ_{ij}. The tensor consists of 6 elements and is symmetric; therefore one can decompose this tensor to three major axes K1, K2, and K3. K1 represents the largest axis of anisotropy of magnetic susceptibility, K2 represents the intermediate axis, and K3 lowest axis (eg. Borradaile & Jackson 2004).

Magnetic fabric in sediments can reflect early deformation by gravitational flattening and can be observed by the K3 being perpendicular to the bedding plane (Sagnotti et al. 1998; Parés et al. 1999). This feature is retained irrespective of further basin evolution. Newer fabrics will be formed if the maximum strain is surpassed and causes distinctive clustering of K2 and K3 (Mattei et al. 1997).

Tectonic influences are not only properties that can be found in AMS. AMS can also reveal mineralogical information, but it is complicated to match the magnitude and nature of the magnetic anisotropy to the controlling physical or mineralogical properties of the site and therefore the magnetic carrier (Borradaile & Henry 1997). Mean bulk susceptibility values ($K_m > 10^{-6}$) are characteristic for ferromagnetic carriers, while lower mean susceptibilities are often suggest the main mineral assemblage to be paramagnetic (Hrouda & Jelinek 1990). There is also a rule of thumb that the lower the mean bulk susceptibility, bigger the contribution of paramagnetic minerals. On the contrary, Hirt et al. 2004 attributes low bulk susceptibility values to weakly oriented ferromagnetic minerals, therefore the argument is whether rock magnetic carriers can be correctly predicted using solely magnetic anisotropy measurements.

A1.2 Hysteresis loops

A hysteresis loop is measured between ferromagnetic magnets which will need to be initialized before measurement. A calibration sample of nickel is placed to calibrate the magnetometer to minimize errors each time the machine is turned on. The measurement is initiated by the desired maximum field to the right, which slowly decreases to 0 followed by an increase in field to the left. The magnetic particles in the sample will flip to the magnetic direction if the sample is subjected to an adequate amount of magnetism equal to $\mu_0 H_f$, which is the flipping field parameter. This flipping field parameter is dependent on the angle of the magnetic mineral when compared to the applied field. As the machine inverts the process, the flip back will again occur at $\mu_0 H_f$ (Tauxe et al. 2010). The probe measures the vibration due to the changing field characteristics in which the amplitude is proportional to the moment in the axis of the applied field direction (Tauxe et al. 2010).

A1.3 XRF instrument errors

Instrument errors arise next to the measurement errors that are shown in the main text results. The instrument errors here consist of the uncertainty that holds in the measurement in comparison to the balance. The values of the TAM cores, their measurement error and percentage of error are shown in table A1. Typically, a sample that has low to 0 ppm measured shows an error that is larger than the base value, which is indicative for a sample that is not present in the rock, which most probably is the case for phosphorus, copper and chrome as shown in the bottom of table A1. A lot of

other minerals were measured, but had the same result as copper, indicating that they are not present in the rock composition. The minor elements, shown in the middle of table A1, show a higher error up to more than 10%. The major element errors, shown on the top of table A1, show a small percentage of error around up to 5% which makes the instrument errors of inferior importance to the standard deviation error in the main text.

	Value	Error	% Error
Mg	60673.28	2689.48	4.43%
Ca	217120.6	1461.028	0.67%
Si	57069.94	569.911	1.00%
K	8214.828	311.3057	3.79%
Fe	13720.08	242.2279	1.77%
Al	13420.87	547.6355	4.08%
Zr	25.92265	2.494717	9.62%
Cl	237.1367	28.02523	11.82%
S	318.6731	76.09564	23.88%
Ti	610.5946	36.96034	6.05%
V	64.73661	26.10808	40.33%
Rb	9.698502	1.076376	11.10%
Mn	1381.692	99.02315	7.17%
Ba	252.4032	58.03854	22.99%
Cu	1.874928	13.28257	708.43%
P	6.871547	103.6311	1508.12%
Cr	23.55827	44.30381	188.06%

Table A1: Overview of the XRF-machine errors with respect to the balance elements. The table is split in three parts: large presence on top, followed by small presence and no presence due to close-to-zero value.

A2. Results appendix

A2.1 Digitalized literature stratigraphic columns

The stratigraphical columns that originate from the literature references are digitalized and shown below in figure A1 and A2. The column of Corrales et al., (1974) has a higher focus on fossil content and sedimentological features, while the column of Diez Balda (1986) shows more relative hardness. The stratigraphical columns have not been taken at the same position, therefore lateral variations might occur.

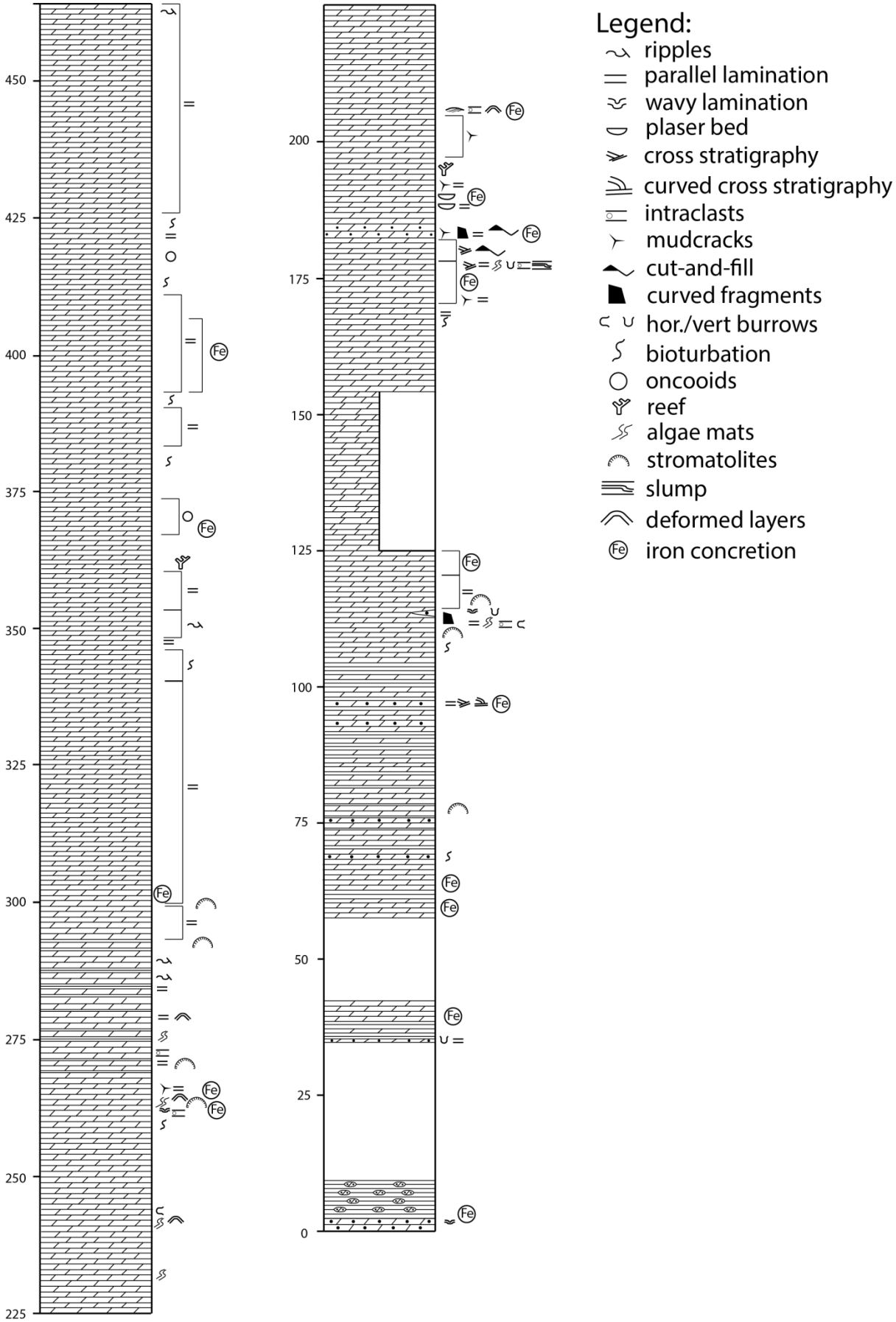

Figure A 1: Digitallized and untouched image of the stratigraphical column of Corrales et al. (1974).

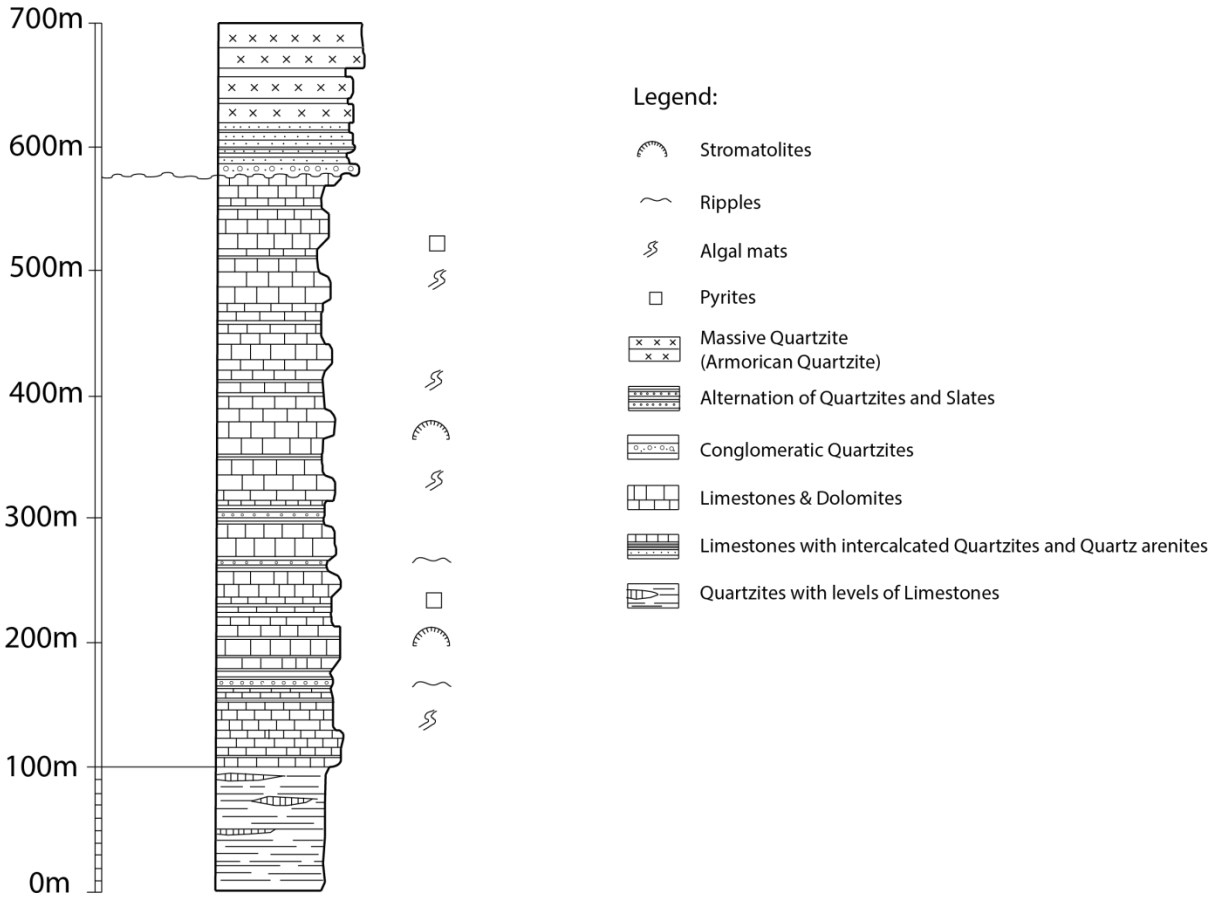

Figure A 2: Digitallized and untouched image of the stratigraphical column of Díez Balda (1986).

A2.2 Temperature steps in the NRM

Figure A3 shows an overview of the different procedures and results during the thermal demagnetization. In figure A1a shows an overview of the first set of samples that is used to obtain a suitable set of thermal demagnetization steps shown in TAM1-43 with tilt correction. The following temperature steps were implemented: 20-100-150-180-210-240-270-285-300-315-330-345-400-450°C. The magnetic intensity is slowly rising and decreasing fast from 285 to 330, with a peak at the latest part. From 400 up, a small increase of magnetism occurs. Using the Zijderveld plot provided, one can see that there is a trend from the 240 to the 330 degree Celsius measurements, where a line is fit in excluding the origin. The magnetic directions are mainly focused around the south southeast, while the 20 degree step and the 345+ degree step show a different direction. This measurement concludes a declination and inclination of 141 and 0 respectively.

Using this set of samples, a new set of temperatures is found and measured to increase the measurement density at the decrease of the magnetic intensity: 200-250-270-285-295-300-305-320-°C. An example of these is TAM1-7, found in figure A3b The intensity starts quite low (3.689x10-3 A/m2) and is decreasing quite rapidly to a close to zero value. The Zijderveld plot shows a continuous trend towards the origin, so all temperature steps can be used in the determination of the magnetic declination/inclination, which is 126/6.

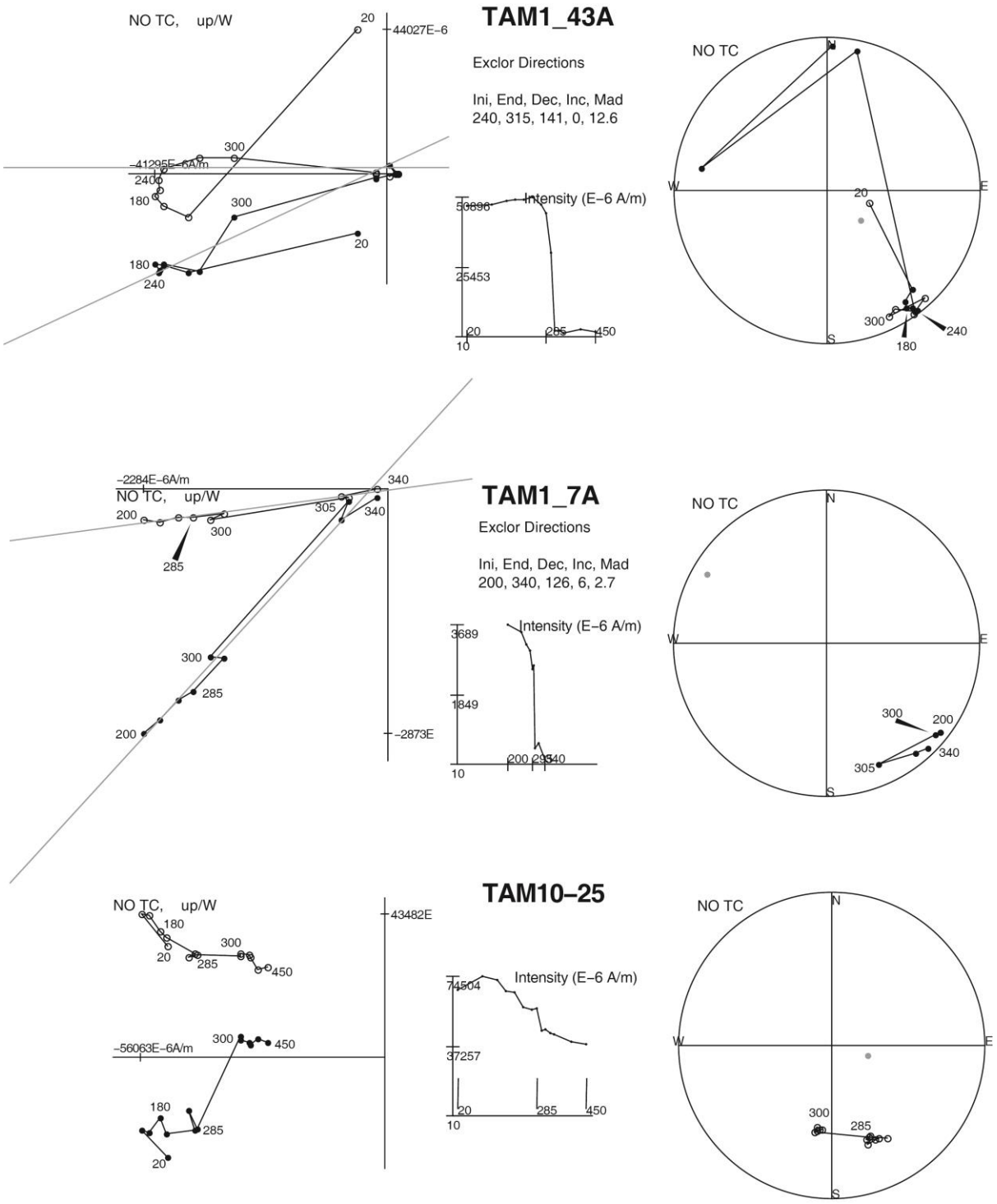

Figure A 3: examples of behavior of thermally demagnetized rocks. The temperature paths are described in the text.

There is another major group in the Tamames limestones that behave quite differently from the rest, an example can be seen in figure A3c where TAM10-25 is shown, which was in the first set and had similar temperature steps as TAM1-43. The intensity plot shows that the rock is not completely demagnetized, but up to about 50%, while the Zijderveld plot shows a trend, but since the rock is not fully empty, there is no direction taken from this core.

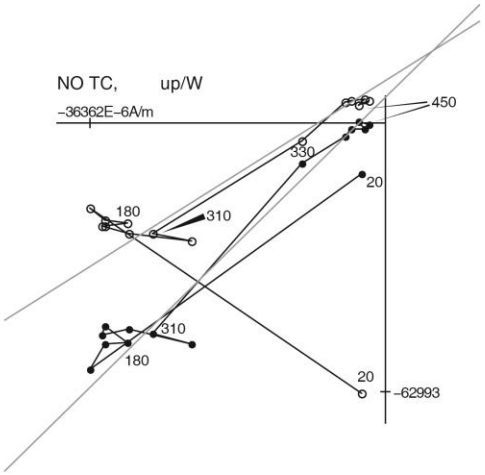

DB3–3–6

Exclor Directions

Ini, End, Dec, Inc, Mad
240, 400, 118, 29, 6.5

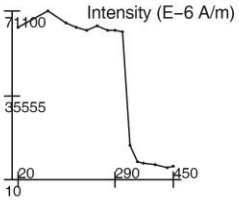

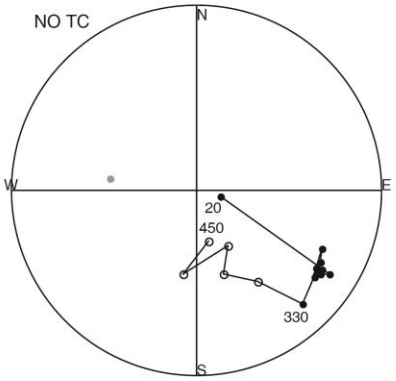

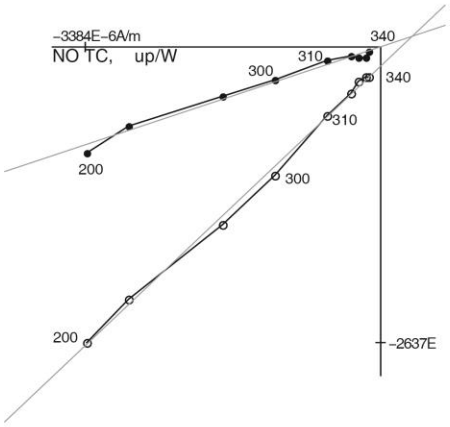

DB6–1–10

Exclor Directions

Ini, End, Dec, Inc, Mad
200, 350, 165, 36, 2.1

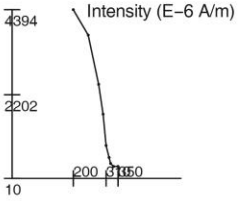

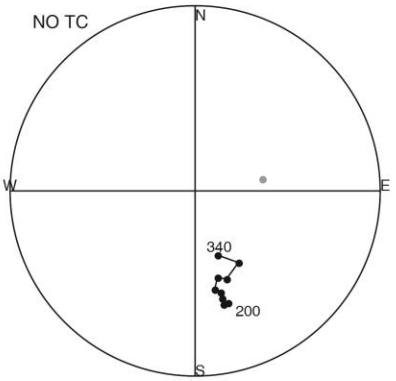

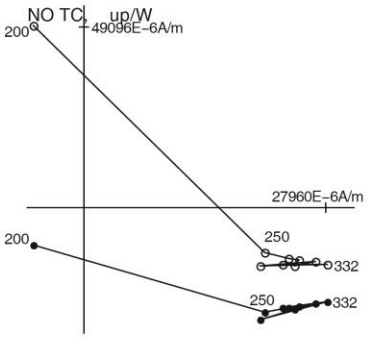

DB3–1–2

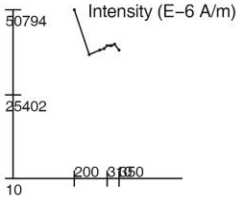

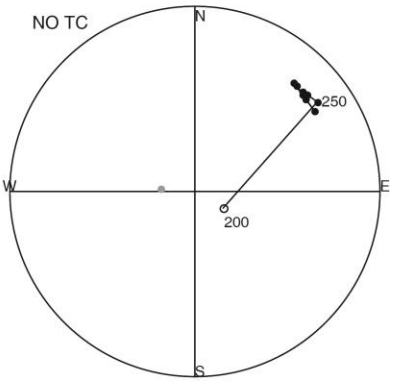

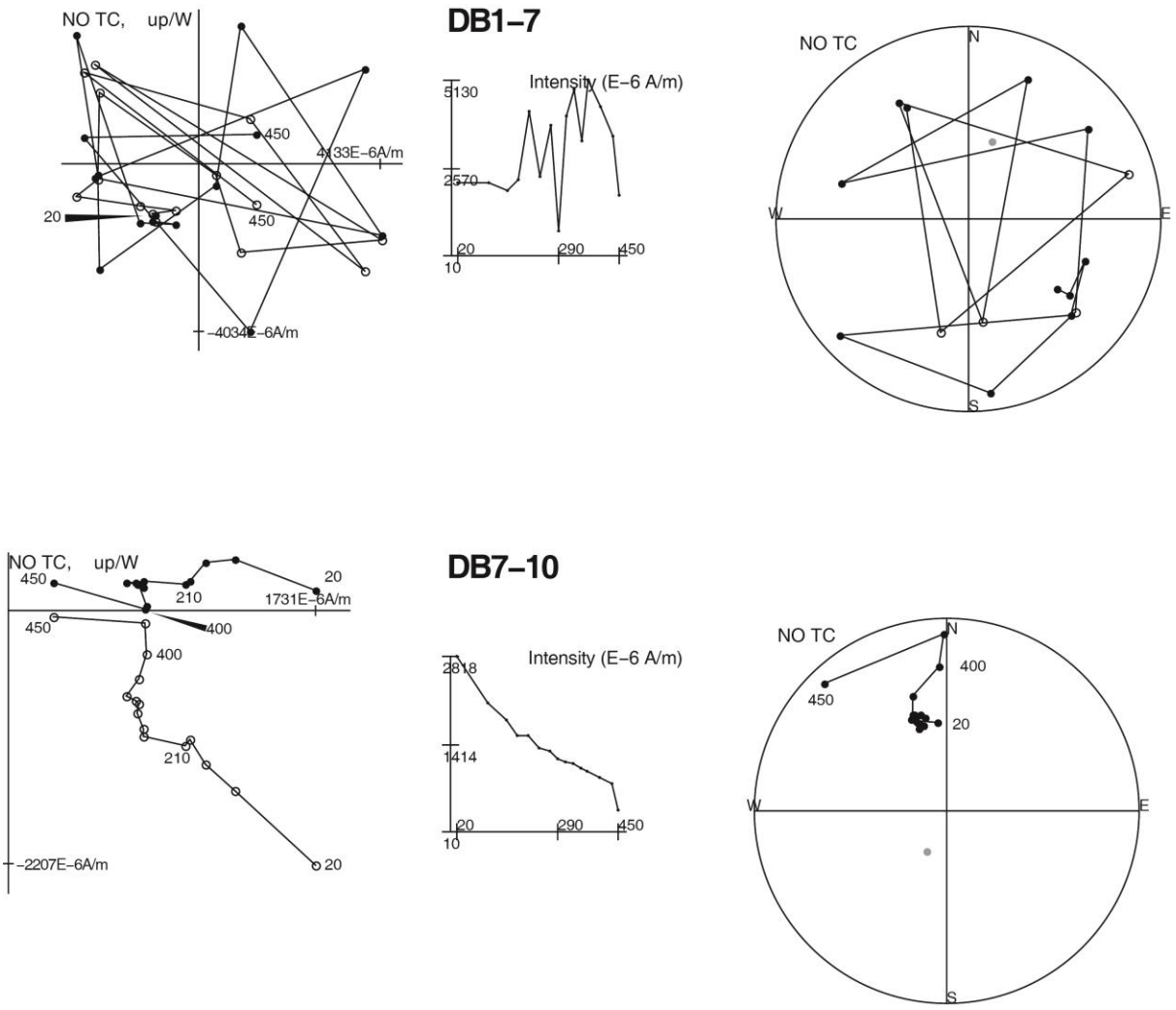

Figure A 4: overview of the different behaviors in the Los Navalucillos Limestone Formation.

Like the Tamames samples, DB-samples of the Los Navalucillos formation behave in different ways, shown in figure A4. In a, an example of the test set is shown in which the temperature steps vary from 20 to 450°C via 20-100-150-180-210-240-270-290-310-330-350-370-400-435-450°C. The intensity of the DB3-3-6 sample shows a rapid decrease at 290 and is mostly horizontal at other temperature ranges. The Zijderveld plot shows a trend towards the origin from 240 up to 400 degrees, which is used to come up with a declination/inclination of 118/29.

Using the test sample, different sets can be distinguished which are discussed here. DB6-1-10 is shown in figure A4b, which has temperature steps starting at 200°C, followed by 250-285-300-310-317-325-332-350°C. These points follow a nearly straight line towards the origin, so all points are considered valid for the determination of the direction, which is 165/36 in this case.

A second set is shown in figure A4c, which shows no complete demagnetization as shown in the intensity plot, which shows a decay of about 30%, but a rising intensity after the decay. The plot shows no trend; therefore no direction could be detected.

Figure A4d shows a sample of DB1-7 which does not tend to have any direction at all. The same temperature steps as in figure A4a are used, but there is no trend or correlation and therefore no direction. Most of these samples are found in DB 1 and 2.

DB 7 and 8 show a different habit due to a different location and age. They all are magnetically very weak with samples starting from about $3x10^{-3}$ A/m, but still show good results. For this particular sample the same temperature steps are used as in a, but for the majority, a separate scheme has been used. This sample shows no accurate direction.

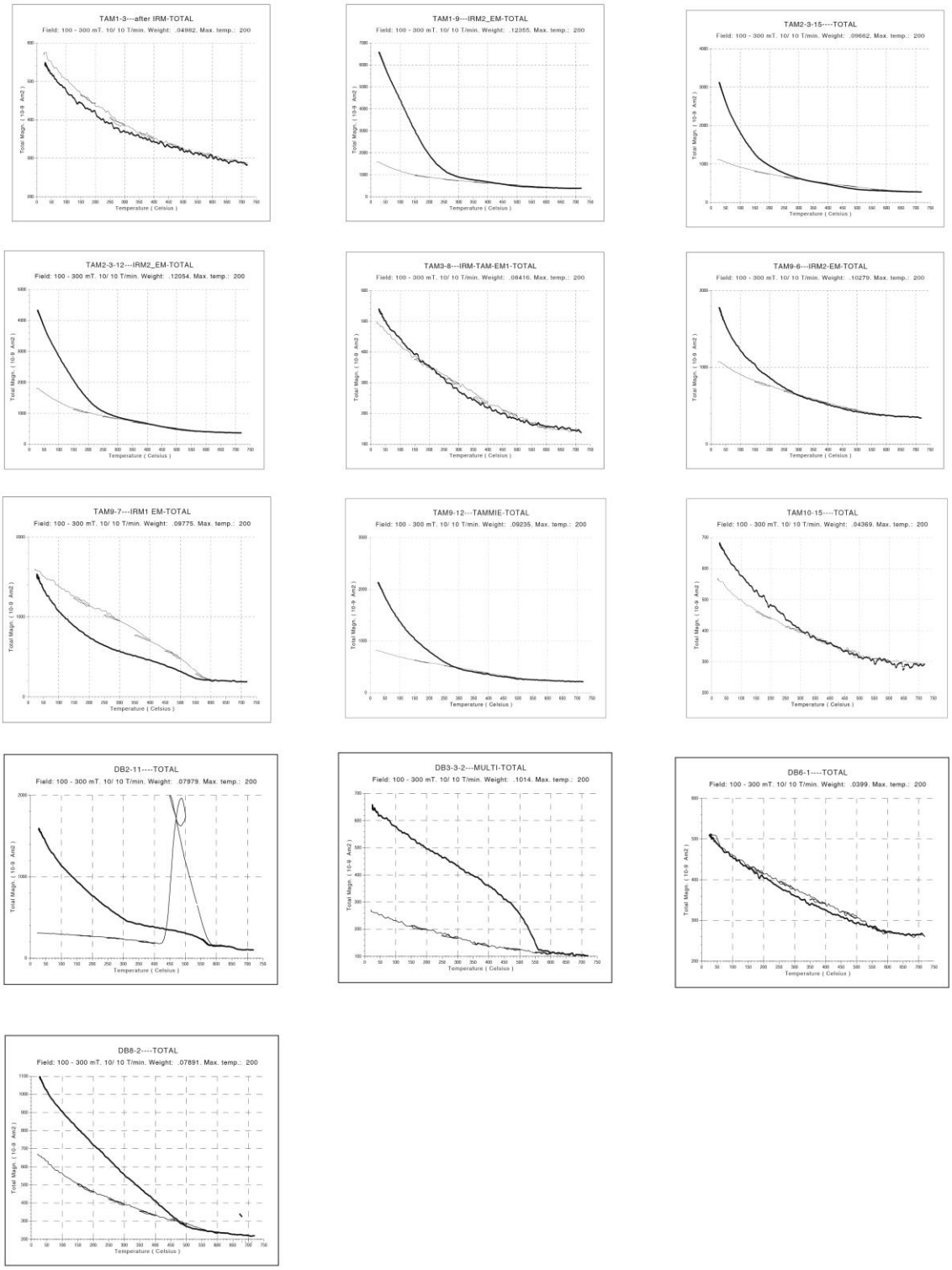

Figure A 5: Complete overview of the measurements of the thermomagnetic analysis. The main results are explained in the main text.

A2.3 Thermomagnetic analysis

The magnetic study of all the selected TAM and DB cores is shown in figure A5, which is constructed using hysteresis loops. In this figure, the x-axis shows the coercivity in millitesla while the y-axis shows the squareness of the sample (Mr/Ms). As stated before, different maxima of applied field have been used varying between 0.5, 0.7, 1.0, and 2.0 Tesla. Most of the samples tend to be very weak in magnetization, hence the plotted line can be sinusoid and unstable, but the trend is sufficient to interpret safely.

A2.4 Hysteresis loops

An overview of all the measured hysteresis loops is found in figure A6, sorted on site names. All the plots have the applied field in Tesla on the X-axis and magnetization in A/m on the y-axis. This is just an overview of all the performed measurements, the main results are covered in the main text.

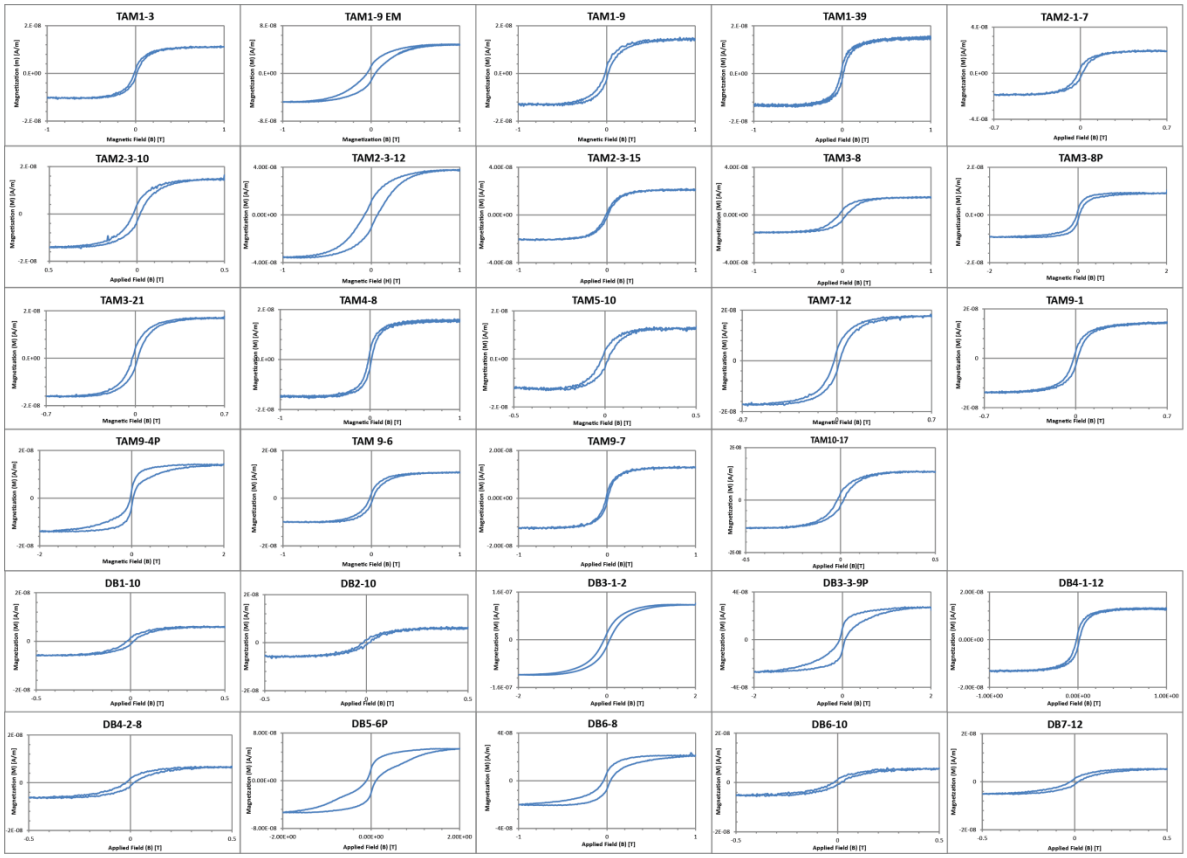

Figure A 6: Overview of all the hysteresis loop measurements that have been performed. The magnetization is situated on the y-axis (in A/m) and applied field on the x-axis in T. The trends are discussed in the main text.

A2.5 IRM set 1

In the results the measurements and conclusions of the correctly measured IRM is shown. A different set is measured with the longitudinal axis first to check for differences.

Figure A7a shows the r^2 plot per end-member of the result of the end-member modelling. By applying the procedure as stated in section 3.3.4, the end-member selection is accepted for 2 and 3 end-members.

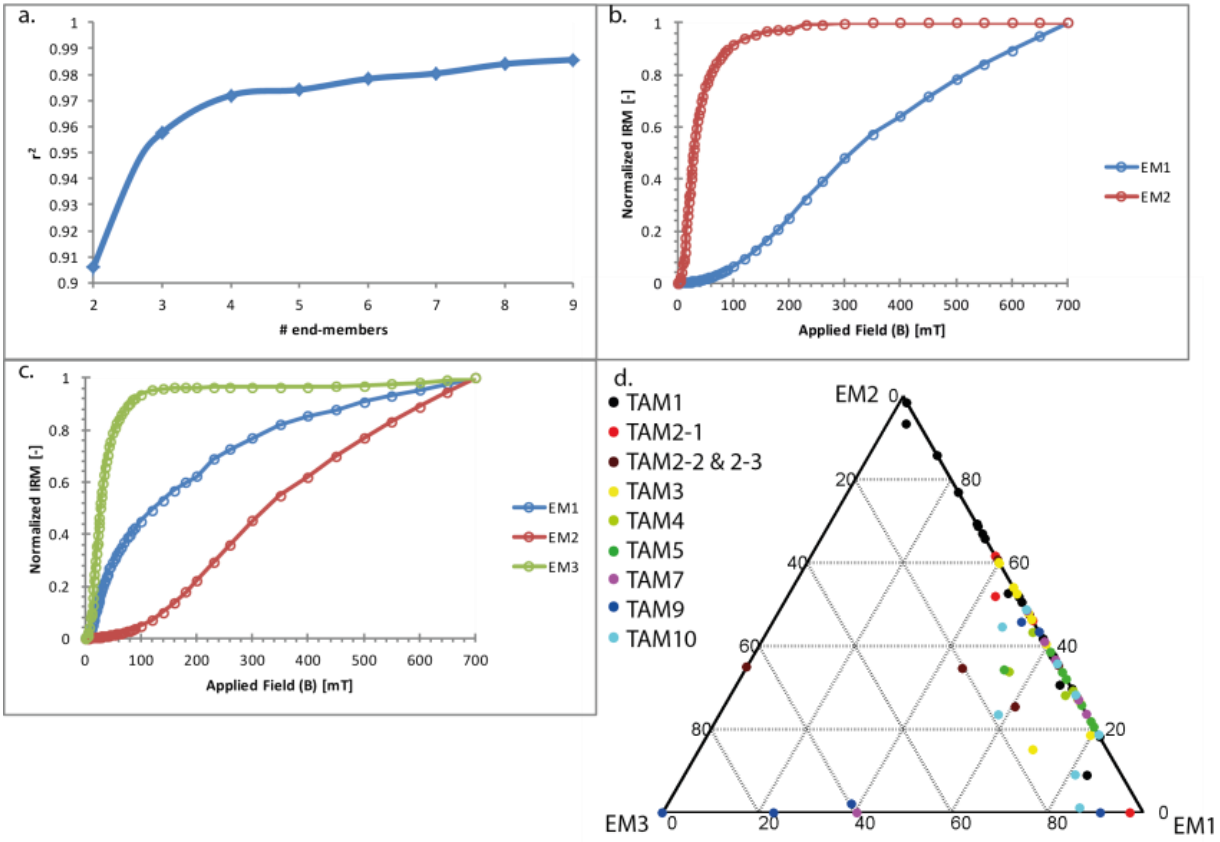

Figure A 7a: r^2 plot of the IRM1 set with the r^2 on the y-axis and amount of end-members on the x-axis. b-c: two and three end-member solutions of IRM unmixing with applied field (in mT) on the x-axis and normalized IRM on the y-axis. d: triplot showing the distribution of the samples across the set for three end members.

IRM set 1 contained 96 samples of which 78 are accepted for the end-member modelling. The results are shown in fig A7b and A7c. This shows two different solutions with a normalized 2 and a 3 end-member model on the y axis plotted over the increasing applied fields on the x-axis, where the dots represent the measurement positions. The two end-member version shows a steep rising curve saturating around 350 mT and a second not fully saturated end member. Adding a third end-member shows an end-member saturated around 140 mT, one end-member saturating around 550 mT and one flat curve which starts to increase in acquisition at 100 mT whereas not saturating at 700 mT. A ternary plot of end-member contributions can be found in figure A7d. The EM3 samples contributions are relatively low, but this second end-member shows distinct habit of the samples and is therefore accepted as end-member.

Figure A8 shows an overview of the mathematical end-members of IRM set 1. The results show EM1-1 which rises continuously, EM1-2 which is not saturated at the end of the test and rising steeply and EM1-3 which shows a big increment around 30 mT combined with a small increment at the end. The end-members are similar to those of IRM set 2, but are ordered differently.

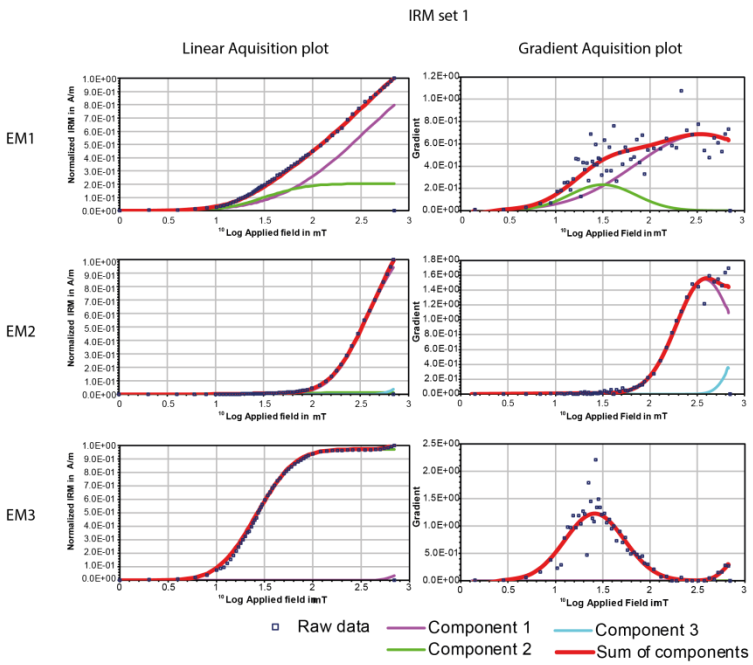

Figure A 8: Unmixed end-members of IRM set 1. The left plots show the linear acquisition plots and the right plots show the gradient of that. The y-axis shows normalized IRM and the x-axis shows the logarithmic scaled applied field. The graphs represent the hypothetical 100% end-member which is not a sample per definition.

The IRM acquisition of EM1-3 shows one large increment of remanence around 30mT with a small increase at the end. The thermomagnetic analysis shows a higher intensity at the heating curve in comparison to the cooling curve with an inflection point at 580°C, which is typical for magnetite. The hysteresis loop shows a SPM state. The NRM demagnetization in the bottom of figure A8 shows an almost fully demagnetized sample. The sample is interpreted and has a declination of 68, which means that is has been rejected by the 45 cutoff.

Figure A9 shows an overview of highly representative samples of IRM set one. End-member one shows a 2 step buildup in the IRM plots with two peaks at 30 mT and 200 mT. The thermomagnetic analysis shows a small addition an equal heating and cooling curve and this sample shows a SPM/PSD type hysteresis loop. The ChRM is fully demagnetized at 350°C.

EM1-2 shows a USD style with a slight wasp-waisted style hysteresis loop, which is a major difference in comparison to the other end-members. The Isothermal remanence shows a peak around 250 mT, but also shows a non-fully saturated sample. The NRM shows that the sample is fully demagnetized at 350°C.

As seen in figure A7d, the TAM9 samples tend to dominate the low-supported end-member, as well as one sample from TAM7 and one from TAM2-2/2-3. Also interesting to see is that TAM1 is largely dominating EM1-2, which is the unsaturated end-member.

A2.6 End-member interpretation IRM set 1

Comparing the different parameters of the EM's that have been proposed by end-member modelling can be done using all the available data.

When taking IRM set 1 into account, the differences are mainly expressed in the thermal demagnetization. EM1-2 shows that the sample is not fully demagnetized at 350°C, which is distinguishable as well in the open hysteresis loop. The main difference of EM1-1 and EM1-3 is found in the hysteresis loop. The loop of EM1-1 is lightly more open.

Striking to see is that the end-member that is associated with magnetite growth in IRM1 shows a magnetite presence in the thermomagnetic analysis, but the NRM is dominated by pyrrhotite as the

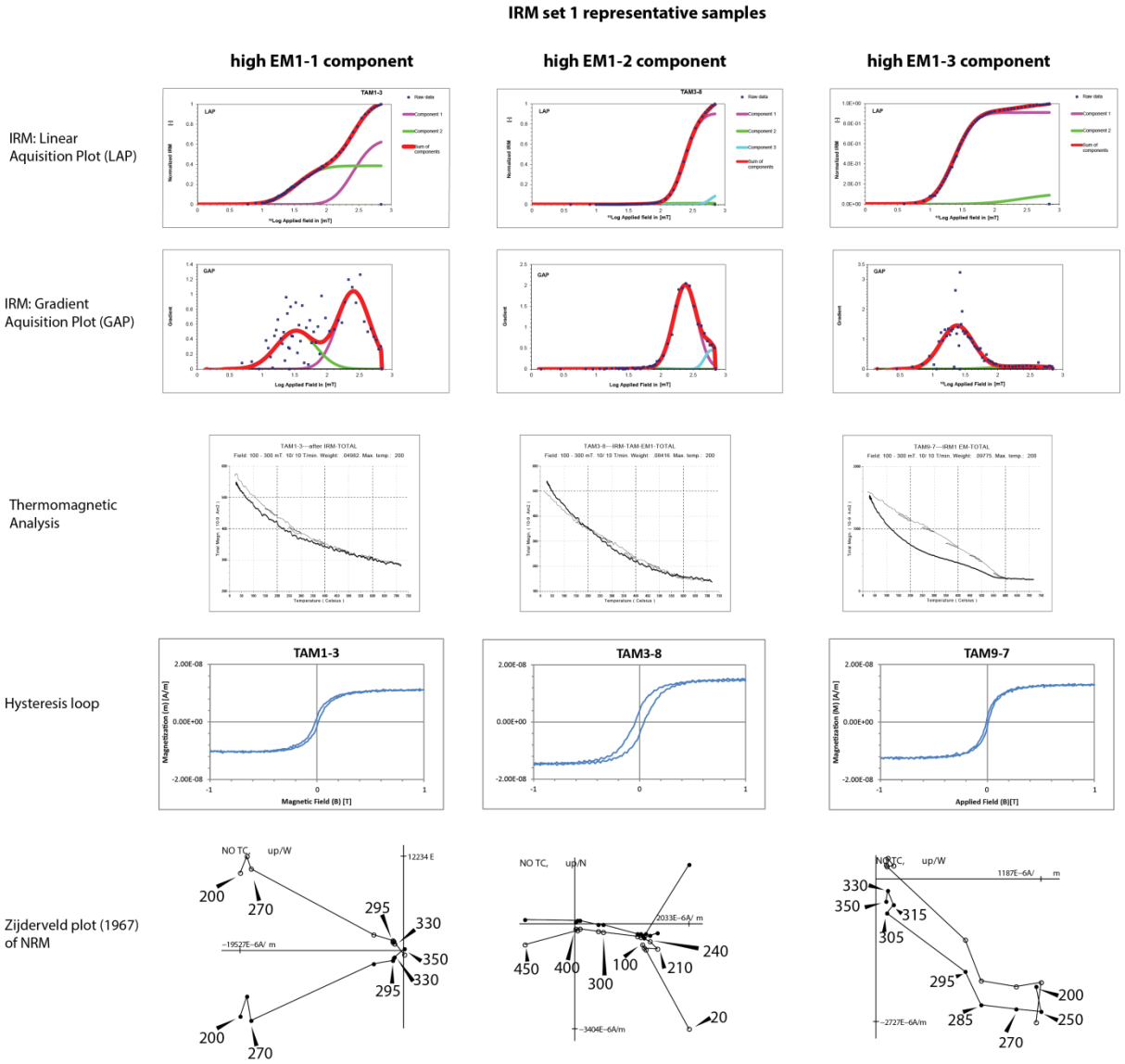

Figure A 9: Overview of major representative samples per end-member of IRM set 2. The top two graphs show the unmixed IRM, followed by a thermomagnetic analysis, a hysteresis loop and the ChRM obtained by thermal demagnetization (temperature steps shown in °C).

sample is close to fully demagnetized at 350°C. This shows that there is already a combination of both minerals present in this end-member. Also important to observe is that the USD end-member already shows large grains of pyrrhotite, as the IRM is not fully saturated at 350 mT.

Comparing these results to the IRM2 set, which is covered in the main text, the same habit arises, though the plots differ a bit. The main results again shows 1 magnetite end-member in combination with two pyrrhotite end-members which have different grain sizes throughout the sample. This strengthens the conclusions made in the main text.

A2.7 Demagnetization prior to IRM: a comparison

The two IRM batches are prepared in different ways. Before applying IRM acquisition, the sample needs to be demagnetized in an alternating field. As the longitudinal axis is measured, the usual method is to demagnetize this axis the latest, which has happened for IRM batch 2, but not for batch IRM1. This provides the opportunity to check for differences in acquisition curve, and to see if both

can be compared. This can be seen in figure A10 where normalized IRM graphs of randomly selected samples are shown. Two samples occurring in both IRM sets are TAM1-39 and TAM4-3. As can be observed on the plot, the main behavior of the sample is the same, but changes do occur, mainly observed in TAM4-3. The main difference is an apparent undersaturation of the sample in IRM1, while there is already is a decline at the highest applied fields of IRM2. TAM1-39 is very similar in both IRM1 and 2.

Each IRM batch has one duplicate sample which is used to test for consistency of the set. In IRM1, sample TAM3-15 was double and the results are quite different as the peak of the acquisition is around 250 mT, while the IRM2 remains apparently undersaturated. TAM1-15 was double in the second IRM set and shows a similar trend line, but only minor changes in the sizes of the acquisition. The fact that these sets show consistency, but no similarity complicates drawing conclusions as there is variability in both a double core in one set, but also differences between the different IRM batches.

This leads to the tentative conclusion that the order of axis demagnetization prior to IRM acquisition does not matter for this type of rock. This is however quite risky to fully accept the conclusion on the basis of this low amount of samples since there are quite some discrepancies, so more of the data should be reviewed as well as different data sets.

One difference between set 1 and set 2 was the size of rock chips. Less material also means a less accurate measurement, which could be of decisive influence when using IRM.

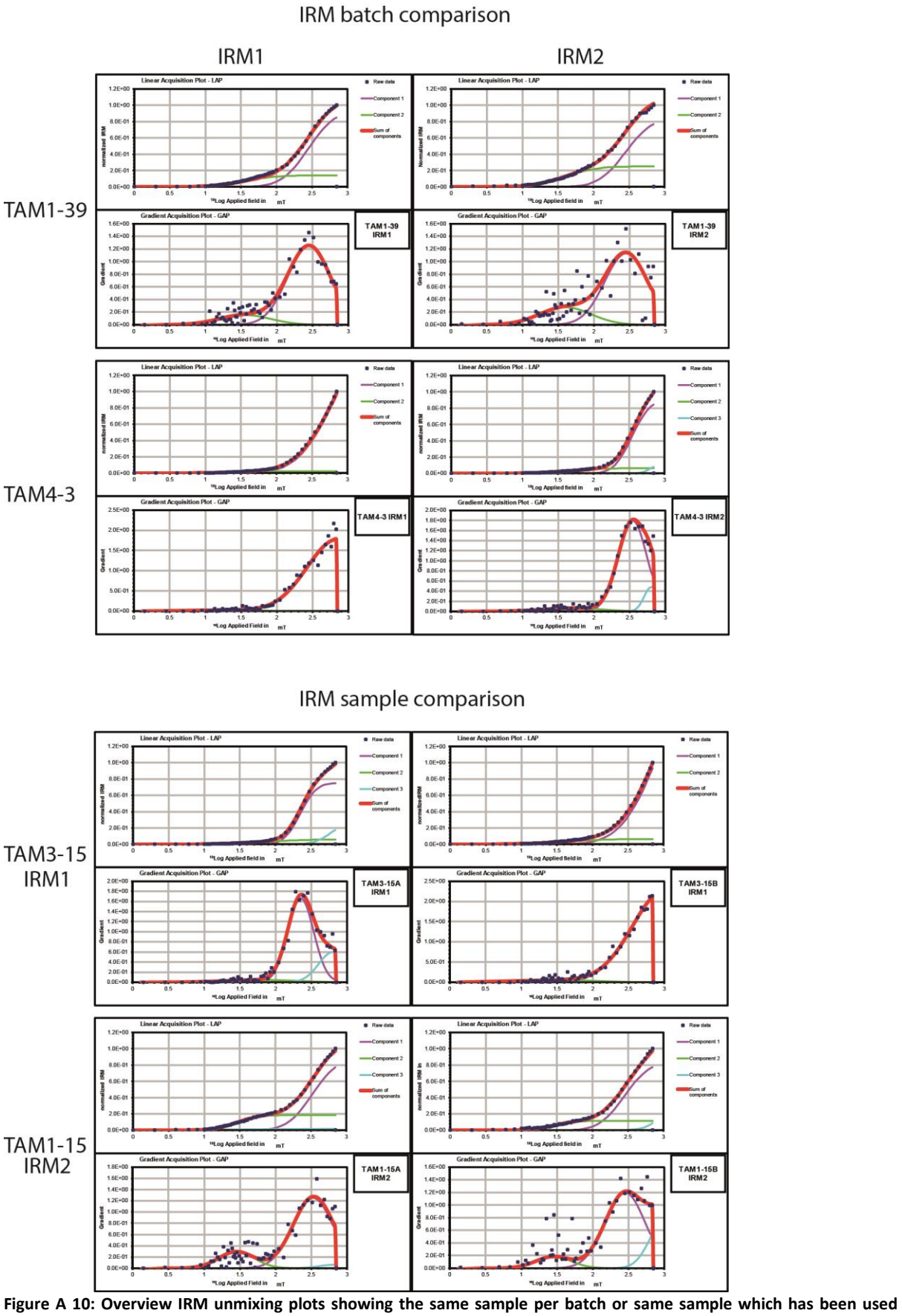

Figure A 10: Overview IRM unmixing plots showing the same sample per batch or same sample which has been used twice in one set. The top plot always shows a linear acquisition plot, while the bottom plot shows the gradient of that acquisition.